TISSUE AND VASCULAR OXYGENATION DYNAMICS DETERMINED BY OPTICAL APPROACHES AND MRI

by

MENGNA XIA

Presented to the Faculty of the Graduate School of

The University of Texas at Arlington in Partial Fulfillment

of the Requirements

for the Degree of

DOCTOR OF PHILOSOPHY

THE UNIVERSITY OF TEXAS AT ARLINGTON

May 2007

ACKNOWLEDGEMENTS

First of all, I am grateful to my advisor, Dr. Hanli Liu. Throughout my doctoral work, she encouraged me to develop independent thinking and research skills. She provided me a perfect balance between guidance and freedom, which allowed me to pursue my own ideas along the right direction. To me, she is not only a wonderful advisor, but also a role model as a successful female scientist, who can balance the family and career perfectly. I am also very fortunate to have Dr. Ralph Mason as my co-advisor. His knowledge and passion in cancer research inspired me, and his meticulous attention to details has helped me to sharpen my skills as a scientist throughout my doctoral work. I would like to give my deepest thanks to them for providing me with invaluable consistent guidance and support during my graduate study.

I would like to thank Dr. Levine for providing me the knowledge, technical support and safety training of hyperbaric chamber. I am also indebted to Dr. Kodibagkar for teaching me the fundamentals of MRI and how to operate the MRI system. I am very grateful to Dr. Alexandrakis for serving as my defense committee member and providing valuable suggestions for my work.

I would like thank all faculties in my department for sharing their knowledge in their classes. I am grateful for the support, assistance and friendship from all the current and previous members of Biomedical Optical Laboratory and Prognostic Radiology Laboratory. I would thank the technical support from Dr. Anca Constantinescu, Ammar

Adam in tumor implanting. I would thank Dr. Weina Cui for teaching me how to implant tumor so I could finish my experiment on time.

The work presented here is supported by DOD breast cancer research grant W81XWH-04-1-0411 (Mengna Xia), DAMD17-00-1-0459 (Hanli Liu), NIH 1R21CA101098-01 (Hanli Liu) and NIH/NCI P20 CA086354 (Ralph P. Mason). The hyperbaric chamber is provided by USAFSAM/FEH Davis Hyperbaric Laboratory at Brooks City-Base, Texas.

Last but not least, I would like to thank my family members for their greatest love and caring. Without their continuous support, I couldn't have today's achievement. I am, and will be deeply indebted to my parents for my whole life. I would like to thank my parents in law, to help me to take care of the baby during the final stage of my doctoral study. I am indebted to my husband Huaping who is the true companion for me in both life and work. I wish I could thank them and this dissertation is dedicated to them.

April 24, 2007

ABSTRACT

TISSUE AND VASCULAR OXYGENATION DYNAMICS DETERMINED BY OPTICAL APPROACHES AND MRI

Publication No. _____

Mengna Xia, PhD.

The University of Texas at Arlington, 2007

Supervising Professor: Hanli Liu

Tumor oxygenation is a crucial factor to determine the efficiency of non-surgery therapy, such as radiotherapy and chemotherapy. Therefore, various approaches have been applied to tumor in order to improve the tumor oxygen level. Breathing oxygen-rich gas with normobaric or hyperbaric pressure has been demonstrated to overcome hypoxia, but with marginal success. Therefore, the outcome would be improved greatly, if the responsive tumors were identified *in priori*. Two non-invasive techniques were applied to monitor tumor oxygenation dynamics simultaneously when rats were exposed to hyperoxic gas intervention. ^{19}F MRI provides tumor tissue oxygen tension (pO_2) images, while Near Infrared Spectroscopy (NIRS) measures global tumor vascular dynamics. Multiple correlations were examined between the rate and

magnitudes of vascular and tissue oxygen responses. In order to extract more physiological information from tumor vascular oxygen measured by NIRS, a mathematical model, modified from the Windkessel model, was used to obtain the tumor blood flow and oxygen consumption rate from hemoglobin concentration.

Besides normobaric oxygen intervention, hyperbaric oxygen intervention was also adopted to improve tumor oxygenation because it increases oxygen tension and oxygen delivery to tissue independent of hemoglobin. Two techniques, FOXY^{TM} fluorescence quenching oxygen sensor and NIRS, were applied simultaneously to monitor tumor tissue and vascular oxygen during and post hyperbaric oxygen administration, so as to investigate tumor oxygenation achieved with hyperbaric oxygen and the preservation of tumor oxygenation after hyperbaric oxygen intervention. I applied combined administration of doxorubicin and hyperbaric oxygen to tumors and compared the tumor oxygenation dynamics, tumor size, body weight between rats with combined therapy and those with doxorubicin alone.

Combined application of MRI and NIRS, and FOXY^{TM} oxygen sensor are novel methodology, which are complementary. Simultaneous application gives us a better understanding on the patho-physiology of tumor and response to therapeutic intervention.

TABLE OF CONTENTS

LIST OF ILLUSTRATIONS

LIST OF TABLES

LIST OF ABBREVIATIONS

ADC	Analogue to digital converter
CBF	Cerebral blood flow
$CMRO_2$	Cerebral metabolic rate of oxygen
CT	Computed tomography
CW	Continuous wave
DOX	Doxorubicin
DPF	Differential pathlength factor
ε	Extinction coefficient
ε_{Hb}	Extinction coefficient of deoxyhemoglobin
ε_{HbO_2}	Extinction coefficient of oxyhemoglobin
E2	17β-estradiol
EPI	Echo planar imaging
EPR	Electron paramagnetic resonance
FO_2	Fraction of O_2
FREDOM	Fluorocarbon relaxometry by echo planar imaging for dynamic oxygen mapping
HBO	Hyperbaric oxygen
HBCB	Hyperbaric carbogen
Hb	Deoxyhemoglobin
HbO_2	Oxyhemoglobin
Hb_{total}	Total hemoglobin
HF	hypoxic fraction
HFB	Hexafluorobenzene
I.P.	Intra-Peritoneal
I.V.	Intra-Venous
I&Q	In-phase and quadrature-phase
MCAO	Middle cerebral artery occlusion
MRI	Magnetic resonance imaging
MRS	Magnetic resonance spectroscopy
NIRS	Near-infrared spectroscopy
NMR	Nuclear magnetic resonance
OVX	Ovariectomized
PFCs	Perfluocarbons
PET	Positron emission tomography
PMT	Photo multiplier tube
pO_2	Oxygen partial pressure

RF	Radio frequency
ROS	Reactive oxygen species
SD	Standard deviation
SE	Standard error
sO_2	oxyhemoglobin saturation
TBF	Tumor blood flow
$TMRO_2$	Tumor metabolic rate of oxygen

CHAPTER 1

INTRODUCTION

1.1 Tumor hypoxia — a target for combined modality treatment

The presence of hypoxia has been demonstrated in breast cancer [1] [2], prostate cancer [3], cervical cancer [4], squamous cell carcinoma of the head and neck [5]. The oxygen levels are typically very heterogenous both among patients and within individual tumors. Tumor hypoxia has been clinically proved to associate with poor outcome of radiotherapy in terms of regional control, disease-free survival and overall survival [6]. The dosage for ionizing radiation required to produce the same amount of cell killing is up to 3 times higher for hypoxic cells compared with well-oxygenated cells [7]. Chemotherapeutic drug resistance in hypoxic cells is also partially caused by reduced toxicity in the absence of molecular oxygen. Furthermore, chemotherapeutic drug delivery to hypoxic areas is challenging since tumor hypoxia itself arises from structurally and functionally abnormal vasculature, thus the effective dosage delivered to hypoxic regions may be much less than to other parts of the tumor [8, 9].

Since inadequate tumor oxygenation is a considerable obstacle in the successful therapy of some human tumors, a number of strategies have been developed to improve tumor oxygenation and increase its uniformity. One commonly accepted method is breathing gas mixtures with high O_2 fractions (either 100% O_2 or carbogen). Using

these gas mixtures at ambient pressure in preclinical animal studies, tumor oxygenation could be substantially improved, although a complete eradication of tumor hypoxia has not been possible in all cases, especially in larger tumors.

Because of the importance of oxygen, many techniques have been developed based on microelectrodes, optical reflectance, electron paramagnetic resonance (EPR), magnetic resonance imaging (MRI) and nuclear medicine approaches, as reviewed previously [10, 11]. Comparing with needle-based oxygen sensitive electrodes, MRI approaches are entirely non-invasive and have advantage of providing dynamic images of tumor oxygen tension [12]. Use of MRI contrast agents, such as perfluorocarbons (PFCs), allow for the determination of pO_2 value within the tissue [12-15]. ^{19}F NMR of PFCs is based on the principle that ^{19}F NMR spin-lattice relaxation rates R1 (1/T1) of PFC emulsions are linearly proportional to oxygen tension. PFCs such as hexafluorobenzene (HFB) are extremely hydrophobic, thus remain as stable droplets in tissue. With the assistance of available imaging protocols, it is possible to produce a pO_2 map with a certain level of temporal resolution. However, the instrument of MRI is large and not readily portable. Therefore, it is desirable to find a complementary method for monitoring intratumor oxygenation rapidly and noninvasively for tumor prognosis and tumor treatment planning. In recent years, Near Infrared Spectroscopy (NIRS) has emerged as an important technique to obtain tissue optical properties noninvasively, because of the relative high penetration depth and absorption characteristics of tissue chromophores, such as oxy-hemoglobin and deoxy-hemoglobin. The change of concentration in deoxy-Hb ,oxy-Hb can be estimated by monitoring the change of

reflectance based on modified Beer-Lambert law [16]. Most NIRS studies conducted to date have been performed on muscle, brain and tumors in human and animal models [17, 18]. Despite a lower resolution compared with MRI, NIRS is attractive because of its direct sensitivity to important physiological parameters, such as oxy-Hb and deoxy-Hb. Moreover, the implementation is relatively inexpensive.

The two non-invasive techniques provide complementary structure and functional physiological information. Hence, combination of these two techniques can be applied to monitor the dynamic change of tumor oxygenation in response to therapeutic interventions, resulting in an improved method to predict cancer treatment efficiency. Meanwhile, they have the potential to enhance our understanding of the complex biological process associated with tumor growth and response to therapy.

1.2 Hyperbaric oxygen — a potential chemotherapy adjuvant

Hyperbaric oxygen (HBO) involves the intermittent administration of hyperbaric hyperoxic gas, such as 100% O_2 and carbogen (95% O_2 + 5% CO_2). In comparison with normobaric oxygen, hyperbaric oxygen increases oxygen tensions and oxygen delivery to tissues nearly independent of hemoglobin. Breathing O_2 at hyperbaric pressure under experimental conditions has provided good evidence that the oxygenation can be improved substantially in solid tumors [19].

Hypoxic tumors are resistant to radiotherapy, photodynamic therapy and some chemotherapy. HBO may help overcome chemotherapy resistance by improving tumor diffusion and cellular sensitivity. HBO therapy in combination with chemotherapy

increases cellular uptake of certain anticancer agents and susceptibility of tumor cells to these agents. It has been shown that HBO improve the therapeutic efficiency of doxorubicin [20, 21], 5-FU [22].

In order to optimize schedule and dosage combination of HBO and chemotherapy, it will provide valuable information to monitor the tumor oxygen dynamics during and after hyperbaric oxygen intervention. An optical oxygen sensor based on dynamic quenching of a fluorescence dye was developed more than two decades ago[23]. The fluorescence dye was immobilized in the probe tip, which is placed directly in the sample. The intensity of fluorescence emitted depends on the oxygen concentration. The FOXY^{TM} fluorescence optical quenching system (Ocean Optics Inc., Tampa, FL) is a multi- channel fiber optic sensor that utilizes this principle to measure discrete changes in local oxygen partial pressure. A multi-channel FOXY^{TM} oxygen sensor has been utilized to study regional tumor oxygen dynamics in a minimally invasive manner [24]. Besides, fiber optic probes of both FOXY oxygen sensor and NIRS could be assembled to the hyperbaric chamber with less difficulty while the major instruments could be placed outside chamber. NIRS combined with FOXY oxygen sensor, thus allow us to monitor tumor vascular and tissue oxygenation simultaneously when the rats were under hyperbaric oxygen intervention.

1.3 Specific aims for the study

The overall goal of this project is to 1) investigate the tumor oxygenation change with respect to hyperoxic gas intervention at ambient pressures and at higher pressures, and the preservation of tumor oxygenation following hyperbaric oxygen intervention;

2) demonstrate that simultaneous MRI and NIRS measurements are a feasible and effective methodology to monitor tumor responses to therapeutic intervention and cancer therapy; 3) investigate if the combined therapy of hyperbaric oxygen and doxorubicin will provide better therapeutic efficiency than doxorubicin alone in our tumor model. The fundamental hypothesis and specific aims of this project are listed as follows:

Hypothesis 1: NIRS provides real time and noninvasive measurement for the dynamic change of tumor vascular oxygenation, which is in good agreement with tissue oxygen tension measured by MRI simultaneously.

Aim 1: to apply NIRS for obtaining global vascular oxygenation and ^{19}F MRI for local tissue oxygenation simultaneously.

Aim 2: to study the correlation between global vascular and tissue oxygenation monitored by NIRS and MRI simultaneously when the rats are under normobaric hyperoxic gas intervention.

Hypothesis 2: Based on an appropriate theoretical model, changes in tumor blood flow and tumor metabolic rate of oxygen can be estimated from the change of hemoglobin concentrations in response to gas intervention, which is monitored by NIRS.

Aim 3: to develop a mathematical model to estimate blood flow and metabolic rate of oxygen in breast tumors in animal models from the change of hemoglobin concentration with respect to gas intervention.

Hypothesis 3: Hyperoxic gas interventions in higher pressure can improve tumor oxygenation better than those in ambient pressure, and tumor oxygenation remains at elevated levels for minutes even after HBO exposure.

Aim 4: to investigate tumor vascular oxygenation and tissue oxygen tension during and post hyperbaric oxygen exposure, using NIRS and multi-channel FOXY^{TM} fluorescence oxygen sensor simultaneously.

Hypothesis 4: Hyperbaric oxygen, when combined with doxorubicin, can provide a better therapeutic efficiency than doxorubicin alone.

Aim 5: to monitor global tumor vascular oxygenation in response to gas intervention by NIRS before and after therapy; compare the growth rate of tumor size, body weight loss between the rats in the group of combined therapy, chemotherapy alone and control.

Hypothesis 5 (appendix): multi-channel NIRS is a valuable approach to monitor the dynamic change of cerebral vascular oxygenation during and after stroke.

Aim 6: to monitor the cerebral vascular oxygenation during and after middle cerebral artery occlusion (MCAO) by NIRS, and characterize the therapeutic effects of estrogen on dysfunctional vasculature induced by MCAO.

CHAPTER 2

TUMOR OXYGEN DYNAMICS MEASURED SIMULTANEOUSLY BY NEAR INFRARED SPECTROSCOPY AND ^{19}F MAGNETIC RESONANCE IMAGING IN RATS

2.1 Introduction

Tumor oxygenation has been widely recognized as a pivotal factor in the efficacy of radiotherapy [25], photodynamic therapy [26] and some chemotherapies [27] and patient stratification with respect to tumor oxygenation status could be clinically important [28-30]. It has been hoped that modulation of tumor oxygenation could be applied to enhance therapeutic efficacy. An attractive intervention is breathing hyperoxic gas, and indeed, several clinical trials have examined the efficacy of normobaric or hyperbaric oxygen, to improve therapeutic outcome, but often with marginal success [31]. It has been suggested that outcome might have been improved, if responsive tumors could have been identified *a priori*. Accordingly, accurate evaluation of tumor oxygenation in response to interventions at various stages of growth should provide a better understanding of tumor response to therapy, potentially allowing therapy to be tailored to individual characteristics.

Given the importance of tumor oxygenation, many techniques have been developed based on microelectrodes, optical reflectance, electron paramagnetic resonance (EPR), magnetic resonance imaging (MRI) and nuclear medicine approaches, as reviewed previously [10, 11]. While each approach has unique strengths, some are

highly invasive. Near-infrared spectroscopy (NIRS) has been developed in recent years as a promising non-invasive technique to quantify the concentration of tissue chromophores, such as oxygenated and deoxygenated hemoglobin, water and lipid [16, 32]. Due to the deep penetration depth and biochemical specificity of NIRS, it has been widely applied for quantitative measurements of cerebral oxygenation [33, 34] and blood oxygenation in muscles *in vivo* [35]. Recently, NIRS has been also used to monitor tumor vascular oxygenation with respect to interventions [16, 24, 36]. With notable exceptions [37-40], NIRS currently lacks spatial resolution, and thus, the utility of global measurements requires validation, given the well-documented heterogeneity of tumor oxygenation. In this regard, Conover *et al* [41] compared the spatially averaged measurement of tumor oxygen saturation (sO_2) using NIRS with the local sO_2 in individual blood vessels measured by cryospectrophotometry. The sensitivity and specificity analysis suggests that NIRS may identify clinically relevant hypoxia, even when its spatial extent is below the resolution limit of the NIRS technique. I have previously investigated correlates between pO_2 assessed by electrodes [15, 42] or fibre-optic probes and NIRS [24]. On occasion, there was a good correlation between global vascular oxygenation and local pO_2 at individual locations, but often, disparate behaviour was observed. Sequential MRI and NIRS suggested a better relationship based on average pO_2 from multiple locations [42]. I have now implemented simultaneous NIRS and ^{19}F MRI to examine the relationships further. Since NIRS is entirely non-invasive it would provide an attractive surrogate for monitoring tumor

oxygenation, and hence, I seek correlations with absolute pO_2 measurements observed simultaneously by MRI.

2.2 Materials and methods

Investigations were approved by the Institutional Animal Care and Use Committee.

2.2.1 Animal preparation and experimental setup

Mammary adenocarcinomas 13762NF (cells originally obtained from the Division of Cancer Therapeutics, NCI) were implanted in skin pedicles [43] on the foreback of ten adult female Fisher 344 rats (~150 g). When the tumors reached ~1 cm in diameter, the rats were anaesthetised with ketamine hydrochloride i.p. (100 mg/kg body weight, Aveco, Fort Dodge, IA) and were maintained under general gaseous anaesthesia (air and 1% isoflurane; Baxter International Inc, Deerfield, IL). Tumor hair was trimmed to give good optical contact for NIR light transmission. Hexafluorobenzene (HFB, 50 μl, 99.9%, Lancaster Co., Pelham, NH) was administered along two or three tracks in central and peripheral regions of the tumors in a single plane (transverse to the rat's tumor, and in the region of NIR photon pathway) using a Hamilton syringe with a 32 G needle. The needle was inserted manually to penetrate across the tumor and was withdrawn ~1 mm to reduce pressure and 3~4 μl of HFB were deposited. The needle was then repeatedly withdrawn 1~2 mm and further HFB deposited at each point, as described in detail previously [11].

The tumor was placed inside a size-matched Helmholtz coil, specially designed for the simultaneous MRI-NIRS study. The tumor was inserted between the two loops

of the Helmholtz coil and two NIRS probes were introduced through the ends of the coil along the coil axis (Figure 2.1). The probes were positioned to be in the same plane as the HFB injection. The rats were placed in the magnet on their side, and body temperature was maintained using a warm water blanket. A total of ten rats were used in the study: seven rats were subjected to respiratory challenge in the sequence of air-oxygen-air-carbogen-air, one rat breathed air-carbogen-air-oxygen-air, one rat breathed air-carbogen-air, and one breathed air-oxygen-air.

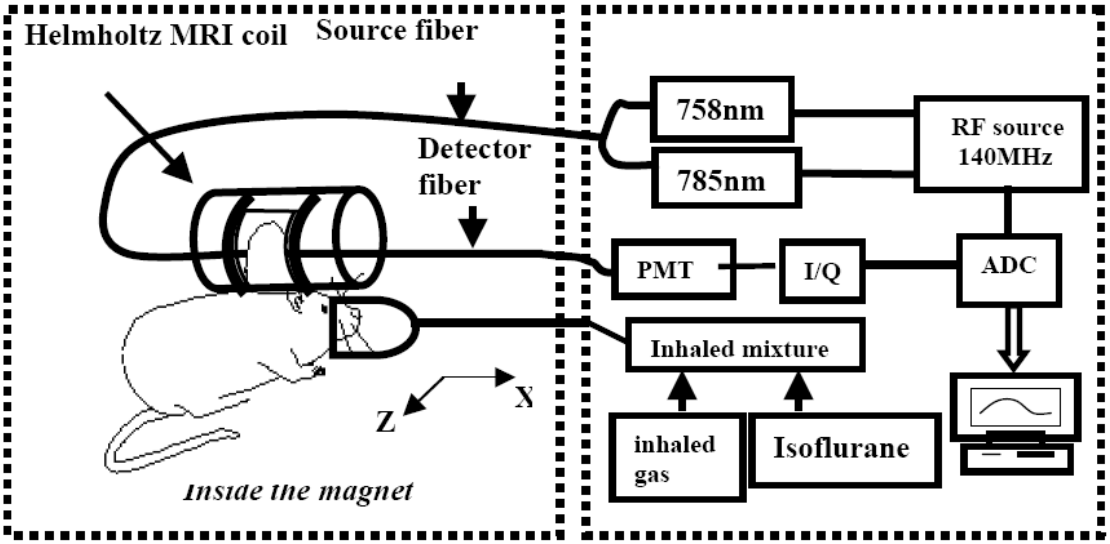

Figure 2.1 Schematic of experimental set-up. Z is along the bore of the magnet, and X along the axis of the RF coil. PMT represents a photomultiplier tube, I/Q represents an In-phase and Quadrature (I/Q) demodulator chip and ADC represents an analogue to digital converter.

2.2.2 NIRS for measuring $\Delta[HbO_2]$

A homodyne frequency-domain system (NIM, Philadelphia, PA) was used to monitor the global change of deoxy- and oxy-Hb concentration ($\Delta[HbO_2]$) in the tumor, as described previously [44], though with minor modifications to ensure MR

compatibility (Figure 2.1). Briefly, the laser light, which was emitted from two laser diodes (at 758 nm and 785 nm), was amplitude-modulated at 140 MHz and time gated on and off sequentially. The two time-shared laser beams illuminated the tumor surface alternately through a light-delivery fiber bundle (source fiber) with a 7-meter length and a 3-mm bundle diameter. The long fibre bundle ensured the separation of the NIRS hardware from the magnet. After being absorbed and scattered in the tumor tissue, the transmitted light was collected on the opposite side of the tumor by another fiber bundle (detector fiber) of same length and diameter as those of source fiber. The collected optical signal was detected and amplified by a photomultiplier tube (PMT). The probe sheaths at the fiber tips were made of nylon for MR compatibility. An In-phase and Quadrature (I/Q) demodulator chip was used to demodulate the amplitude-modulated signal from the PMT.

In principle, since the I/Q system could give both phase and amplitude values, it should be possible to calculate absolute HbO_2, Hb, and sO_2 (Yang *et al*, 1997). However, given the tumor's small size and large spatial heterogeneity, I am currently unable to achieve reliable absolute quantification using the conventional algorithm (Fishkin and Gratton 1993) based on the diffusion approximation. Instead, based on modified Beer-Lambert's law, I simply use the amplitude of the light transmitted through the tumor to calculate concentration changes in HbO_2, Hb and Hb_{total} of the tumor caused by respiratory intervention. Namely, changes of oxy- and deoxyhemoglobin concentration, $\Delta[HbO_2]$ and $\Delta[Hb]$, respectively, can be derived from the measured amplitudes at the two wavelengths (758 nm and 785 nm) [42]

$$\Delta[HbO_2] = \frac{-10.63\log(\frac{A_b}{A_t})^{758} + 14.97\log(\frac{A_b}{A_t})^{785}}{DPF \cdot d} \quad (2.1)$$

$$\Delta[Hb] = \frac{8.95\log(\frac{A_b}{A_t})^{758} - 6.73\log(\frac{A_b}{A_t})^{785}}{DPF \cdot d} \quad (2.2)$$

where A_b is the baseline amplitude, A_t is the transient amplitude during measurement, and d is the direct source-detector separation. *DPF* (differential path-length factor) is a tissue-dependent parameter and is defined as the ratio between the optical path length and the physical separation between the source and detector. The units for $\Delta[HbO_2]$, $\Delta[Hb]$, and $\Delta[Hb]_{total}$ are mM. Since *DPF* is a variable, depending on tissue type and wavelengths, it is currently difficult to quantify *DPF* for tumors. Since this study focuses on dynamic changes of $[HbO_2]$, $\Delta[HbO_2]$ values may be scaled by a factor of DPF (in units of mM/DPF), to obtain characteristic features of tumor oxygen dynamics [16].

2.2.3 Mathematical model for blood oxygenation dynamics of tumors

Based on the previous experimental study, a simple mathematical model [16] has been developed to examine tumor vascular dynamics during oxygen intervention, by analogy to the method used to quantify regional cerebral blood flow (rCBF) with diffusible radiotracers, originally developed by Kety [45]. Accordingly, changes of oxyhemoglobin concentration in tumor vasculature induced by hyperoxic gas intervention, $\Delta[HbO_2]$, can be expressed as

$$\Delta[HbO_2(t)]^{vasculature} = \gamma H_0[1-\exp(-\frac{ft}{\gamma})] = A[1-\exp(-\frac{t}{\tau})] \quad (2.3)$$

where $\Delta[HbO_2]$ corresponds to the changes in oxyhemoglobin concentration from tumor vasculature measured by NIRS, H_0 is the arterial oxygenation input for ΔHbO_2^{artery} after time 0, f is the blood perfusion rate, and γ is the vascular coefficient of the tumor, defined as the ratio of $[HbO_2]$ changes in the vascular bed to that in the veins. Specifically, $\gamma = \Delta[HbO_2]^{vasculature}/\Delta[HbO_2]^{vein}$, τ is the time constant ($= \gamma/f$), and $A = \gamma H_0$.

Given that solid tumors often develop hypoxic regions, which are poorly perfused [46, 47], I hypothesized that the observed, bi-phasic feature of $\Delta[HbO_2]$ came from two different perfusion regions (well- and poorly-perfused regions). Therefore, it is reasonable to define two different blood perfusion rates (f_1, f_2) with two different vascular coefficients (γ_1, γ_2) in the mathematical model. Consequently, equation 2.3 has been modified to a summation of two exponential expressions, representing two perfusion regions, as

$$\Delta[HbO_2(t)]^{vasculature} = \gamma_1 H_0[1-\exp(-\frac{f_1 t}{\gamma_1})] + \gamma_2 H_0[1-\exp(-\frac{f_2 t}{\gamma_2})]$$

$$= A_1[1-\exp(-\frac{t}{\tau_1})] + A_2[1-\exp(-\frac{t}{\tau_2})] \quad (2.4)$$

where f_1 and γ_1 are the blood perfusion rate and the vasculature coefficient, respectively, in the well-perfused region, and f_2 and γ_2 represent the same respective meanings in the poorly perfused region. Also, it follows that $A_1 = \gamma_1 H_0$, $A_2 = \gamma_2 H_0$, $\tau_1 = \gamma_1/f_1$ and $\tau_2 = \gamma_2/f_2$. Since A_1, A_2, τ_1, and τ_2 can be determined by curve-fitting equation

(2.4) to the dynamic NIRS measurements, I can obtain the ratios for two vascular coefficients and two blood perfusion rates, as follows [16]:

$$\frac{\gamma_1}{\gamma_2} = \frac{A_1}{A_2}, \qquad \frac{f_1}{f_2} = \frac{A_1/\tau_1}{A_2/\tau_2}. \tag{2.5}$$

These two ratios provide insight into tumor vascular structures and blood perfusion rates. Specifically, γ_1/γ_2 may be associated with the vascular volume fraction between the two regions, and f_1/f_2 reflects the perfusion ratio between the two regions. For example, if f_1/f_2 is substantially greater than 1, the two compartments have significantly different perfusion rates.

This mathematical model is consistent with experimental animal studies [16, 24, 42]. Moreover, it is supported by computer simulations [48] and a phantom study [49] each of which shows that the bi-phasic or bi-exponential feature can be presented if both a slow and a fast perfusion of flow co-exist within the interrogated volume.

2.2.4 FREDOM for measuring pO_2

MRI was performed using a Varian Inova 4.7 T horizontal bore system equipped with actively shielded gradients. Shimming was performed on the tumor tissue water signal to reduce the line-width to less than 100 Hz. ^{1}H MRI (200.1 MHz). T1-weighted reference images were acquired with TR/TE of 150/10 ms and 40x40 mm^2 field of view. Following ^{1}H MRI, corresponding ^{19}F MR images (188.3 MHz) with a matrix size of 32x32 (1.25 mm per pixel) were obtained to show the distribution of HFB in the tumor. A single 10-mm thick slice was chosen to include all the injected HFB, as the plane of injection was not always perfectly aligned with the imaging plane. The actual volume interrogated is defined by the distribution of the reporter molecule in the

3rd dimension rather than the imaging gradients [11]. The *FREDOM* (*F*luorocarbon *R*elaxometry by *E*cho-planar imaging for *D*ynamic *O*xygen *M*apping) approach was used to measure pO_2, as described in detail previously [14]. The spin lattice relaxation rate (R1= 1/T1) of HFB is highly sensitive to changes in pO_2, but not sensitive to temperature variations: a deviation of 1 ^oC in temperature will introduce a deviation of only 0.13 torr in the pO_2 estimate, when pO_2 is about 5 torr [11]. T1 maps were computed on a voxel-by-voxel basis using non-linear least-squares data fitting by the Gauss-Newton method. I applied a threshold to the raw T1 data in order to remove random noise, *i.e.*, voxels with T1 error >3.6 sec or T1 error/T1 >50% were disregarded. Maps of pO_2 values with 1.25 mm pixel size were obtained from the T1 maps using the equation, $pO_2 = (1/T1-0.0835)/0.001876$ [14].

Each pO_2 map was acquired in 6 1/2 min. Three baseline pO_2 data sets were acquired over 24 mins for all tumors, while the rats breathed air, after which the rats were repeatedly exposed to oxygen or carbogen (95% O_2 and 5% CO_2) interventions. Five pO_2 maps were obtained during each subsequent gas switch period. Typically, for a five gas-intervention sequence (*e.g.*, air-oxygen-air-carbogen-air), a total of 23 pO_2 maps were obtained over a period of 3 h. Due to thresholding, some voxels did not appear in all pO_2 maps and these were discarded. For temporal analysis, voxels were selected as only those which provided consistently reliable data (*i.e.*, satisfied all the thresholding criteria specified above) for all 23 measurements over the time course with a range of 5 to 44 acceptable voxels for the ten tumors. The slope of dynamic pO_2

changes (rate) was defined as $d(pO_2)/dt$ and $d(pO_2')/dt$ in response to increasing or decreasing inhaled FO_2 (Fraction of O_2), respectively.

2.2.5 Statistical Analysis

Linear regression analysis was used to calculate the correlation between the NIRS-derived tumor hemodynamic parameters (*i.e.*, $\Delta[HbO_2]$, A_1/τ_1, A_2/τ_2, f_1/f_2) and the *FREDOM*-determined tumor parameters (*i.e.*, pO_2, $d(pO_2)/dt$, $d(pO_2')/dt$). Data are presented as mean ± standard deviation (SD) and paired Student-t tests compared the effects of oxygen and carbogen on $\Delta[HbO_2]$ and pO_2.

2.3 Results

2.3.1 Dynamic response of $\Delta[HbO_2]$ measured by NIRS

Figure 2.2 shows a group-averaged, temporal profile of $\Delta[HbO_2]$ from seven 13762NF rat breast tumors with air-oxygen-air-carbogen-air intervention, displaying apparent biphasic responses to both interventions. Both single (eq. 2.3) and double-exponential (eq. 2.4) curve fitting were tested for the carbogen intervention in one representative tumor (1.6 cm^3), as in Figure 2.3. The maximal $\Delta[HbO_2]$ achieved with oxygen challenge was compared with that of carbogen, and revealed no significant difference between oxygen and carbogen intervention ($p>0.3$); indeed, there was a strong correlation between the maximal $\Delta[HbO_2]$ values with these two interventions ($R^2>0.75$, figure 2.4), consistent with our previous observations [24]. No correlation was found between the perfusion rate ratio (f_1/f_2) and tumor size ($R^2=0.16$). Vascular oxygen dynamics in response to interventions are provided for individual tumors in table 2.2.

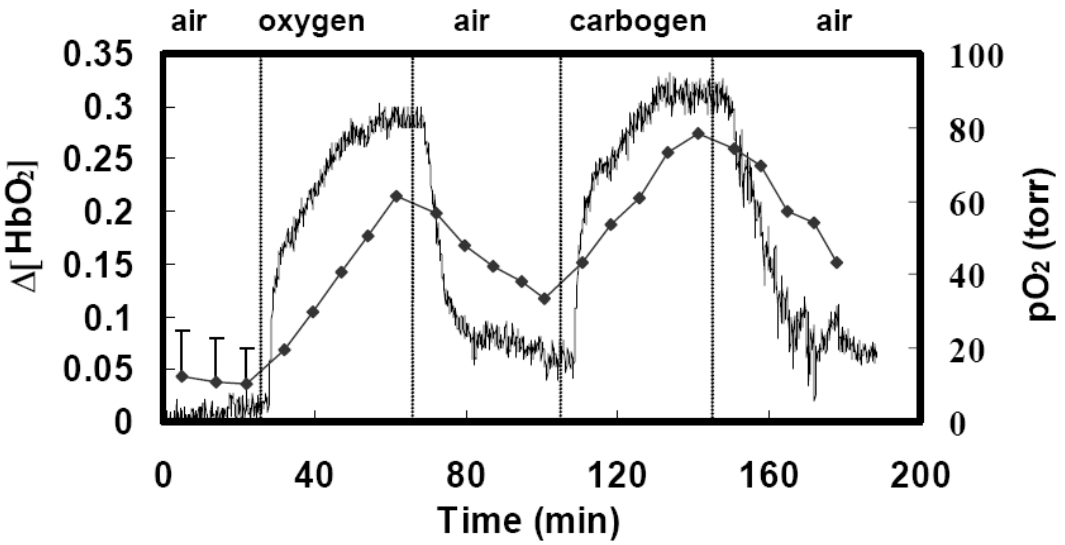

Figure 2.2 Temporal profiles of $\Delta[HbO_2]$ (curve only) and mean pO_2 (curve with ◆) in response to respiratory challenge. Both $\Delta[HbO_2]$ and pO_2 are group-averaged data from seven 13762NF rat breast tumors with an intervention sequence of air-oxygen-air-carbogen-air, measured simultaneously by NIRS and *FREDOM*. The standard deviations of the volume-averaged pO_2 from 7 tumors are indicated for baseline, but became very large in response to interventions and are omitted. $\Delta[HbO_2]$ has units of mM/DPF.

2.3.2 pO_2 measurements by FREDOM

Overlay of ^{19}F and ^{1}H MR images demonstrated that HFB was distributed in both central and peripheral regions of tumors (Figure 2.5). Individual pO_2 values taken from each voxel ranged from hypoxic (< 1 torr) to 35 torr under baseline conditions (Figure 2.6). Mean baseline pO_2 values, which are averaged over all voxels in a given tumor in the first three pO_2 maps, ranged from hypoxic (< 5 torr) to 27 torr with a hypoxic fraction (HF_5; fractional voxels that are less than 5 torr) ranging from 0 to

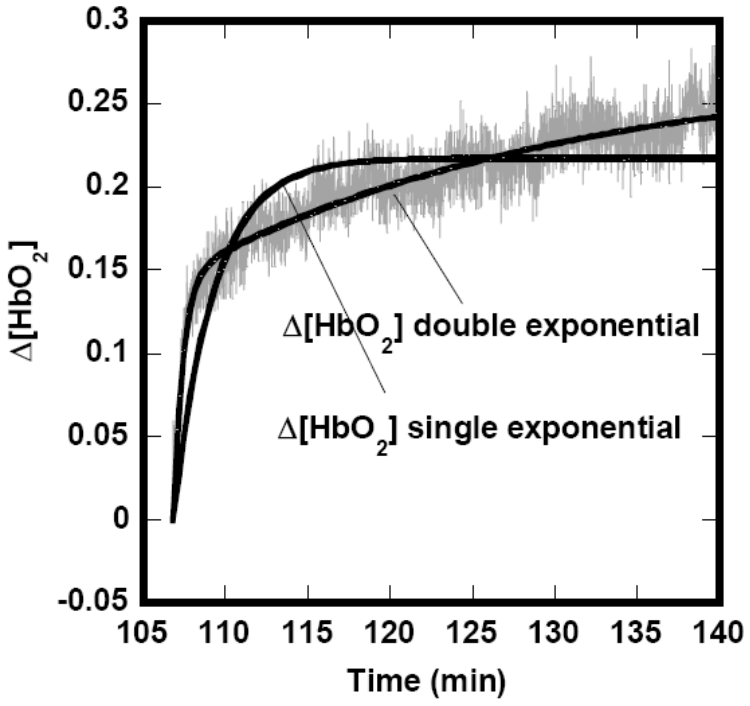

Figure 2.3 Dynamic responses of $\Delta[HbO_2]$ (mM/DPF) to gas intervention (carbogen). Single exponential curve fitting yielded $\Delta[HbO_2] = 0.22\{1 - \exp[-(t-106.8)/2.5]\}$ (R^2=0.64), and double exponential fitting resulted in $\Delta[HbO_2] = 0.15\{1 - \exp[-(t-106.8)/0.58]\} + 0.13\{1 - \exp[-(t-106.8)/23.2]\}$ (R^2=0.88).

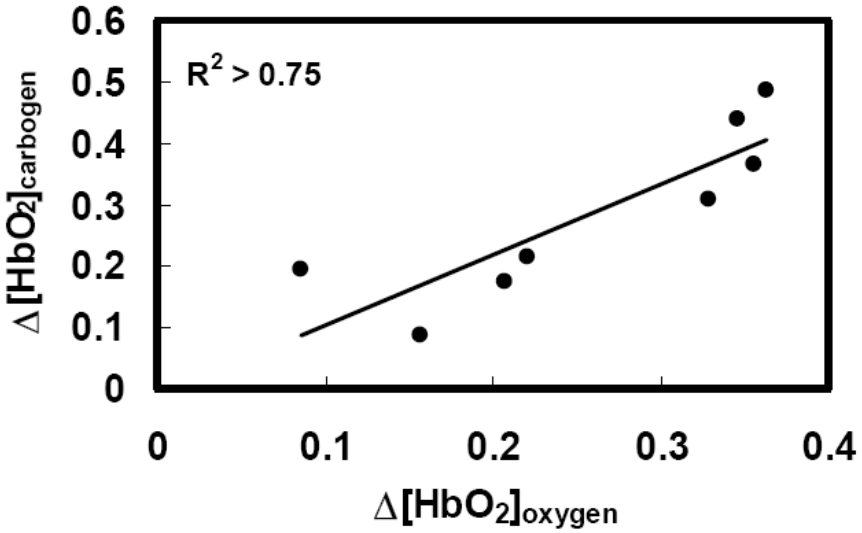

Figure 2.4 Relationship of maximum $\Delta[HbO_2]$ (mM/DPF) in breast tumors in response to switching from air to oxygen and to carbogen (R^2>0.75).

100% (mean 36%) and summarised in table 2.1. A strong correlation was found between mean baseline pO_2 and HF_5 (R^2>0.85, Figure 2.7). Administration of oxygen or carbogen produced significant increases in tumor pO_2, as shown in the pO_2 maps, graphs and table. The tumor pO_2 values were averaged over the entire slice and responses to respiratory challenge for the group of seven tumors, measured simultaneously by *FREDOM* and NIRS, is shown in figure 2.2. Baseline measurements (breathing air) were generally stable, and altering the inhaled gas to oxygen or carbogen induced rapid and significant changes in both pO_2 and $\Delta[HbO_2]$ ($p<0.001$). Upon return to air (baseline), $\Delta[HbO_2]$ dropped quickly and significantly within 16 mins, and then more slowly, for the next 24 mins, whereas the pO_2 decrease was more gradual. Altering the inhaled gas to carbogen also produced a rapid increase in both pO_2 and $\Delta[HbO_2]$. Upon return to air breathing from carbogen, both $\Delta[HbO_2]$ and pO_2 showed a similar trend to that following oxygen. As expected, all ten tumors showed a significant increase in pO_2 (average over entire slice), and decrease in hypoxic fraction (HF) in response to oxygen or carbogen inhalation. The magnitude of response to either hyperoxic gas was correlated (R^2>0.79), as was the maximum volume-averaged pO_2 achieved with either gas (R^2>0.83). The rate of increase with oxygen challenge, $d(pO_2)/dt$, was significantly faster than the return to baseline, $d(pO_2')/dt$, for oxygen intervention ($p<0.02$), but no difference was observed for carbogen ($p>0.1$, figure 2.8). The mean pO_2 values of individual tumors averaged over the final three pO_2 maps during exposure to carbogen breathing were significantly higher than oxygen ($p<0.01$),

and the tumor hypoxic fraction was generally eliminated during carbogen breathing (n = 7 of 9 tumors, table 2.1).

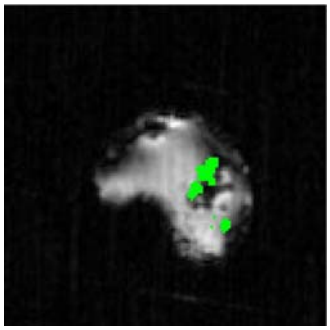

Figure 2.5 Overlay of ^{19}F and ^{1}H MR images. It demonstrated that HFB was distributed in both central and peripheral regions of tumors.

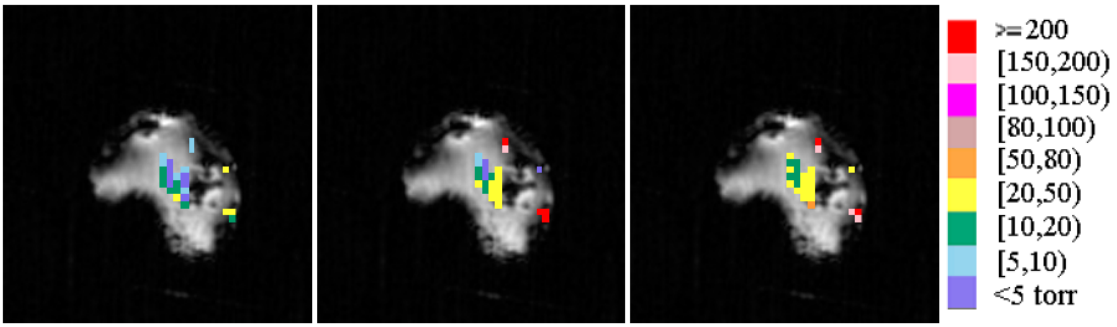

Figure 2.6 pO_2 maps (1.25 mm resolution) obtained using *FREDOM* overlaid on the ^{1}H anatomic image of a tumor (FOV= 4 cm x 4 cm). Left) Rat breathing air, Centre) breathing 100% O_2 (fifth map after switching from air), Right) breathing carbogen (95% O_2 + 5% CO_2) (fifth map after switching from air). The pO_2 maps show distinct heterogeneity.

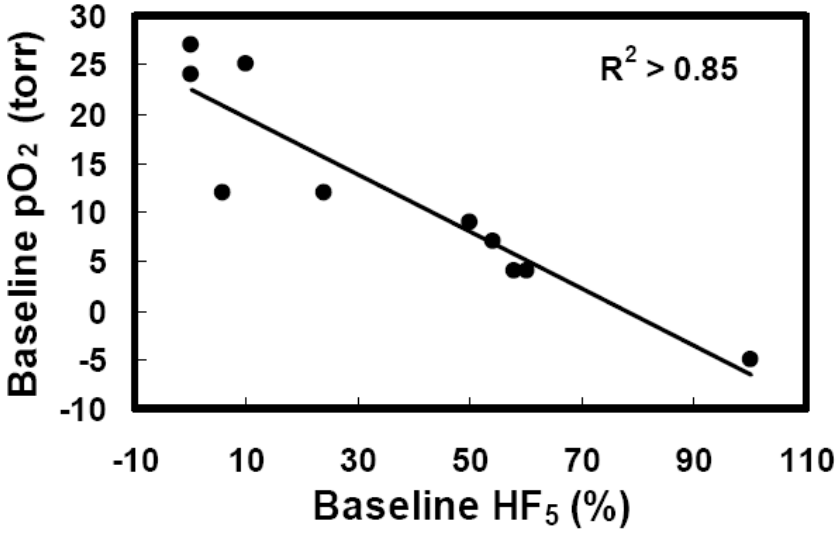

Figure 2.7 Correlation between baseline pO_2 and hypoxic fraction (HF_5) measured using *FREDOM* (R^2>0.85).

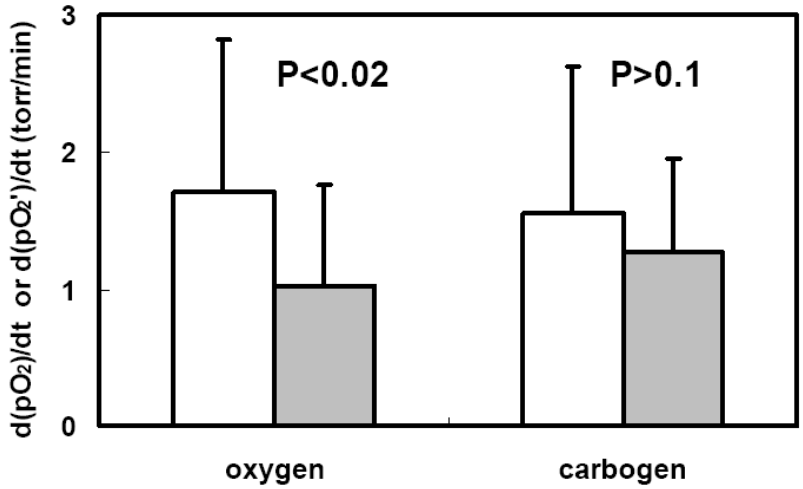

Figure 2.8 Mean $d(pO_2)/dt$ (open) and $d(pO_2')/dt$ (shaded) $\pm$ SD for eight tumors with both interventions, when gas was switched from air to the hyperoxic gas and back to air, respectively. pO_2 is the mean value of all acceptable voxels appearing in the five maps during the oxygen or carbogen intervention. $d(pO_2)/dt$ is the slope of regression line of five pO_2 readings versus time when switching from air to oxygen or carbogen, and $d(pO_2')/dt$ is the slope of regression line for five pO_2 readings during the switch back to air. The rates showed a significant difference with oxygen ($p<0.02$), but not with carbogen ($p>0.1$).

Table 2.1 Oxygen tension (pO_2) in ten rat mammary 13762NF adenocarcinomas. pO_2 in baseline is the average value of all voxels in the first three maps, while pO_2 for oxygen or carbogen is the average value of all voxels in the final three pO_2 maps during exposure to the hyperoxic gas. Hypoxic fraction (HF) is the percentage of voxels with pO_2 values less than 5 torr (HF_5) or 10 torr (HF_{10}) and HF_5 and HF_{10} are the average value of final three maps in baseline, oxygen or carbogen respectively. The mean pO_2 increased significantly with both oxygen and carbogen and the value was significantly higher with carbogen. HF_5 was significantly reduced with oxygen or carbogen.

Tumor			Baseline (air)			Oxygen challenge			Carbogen challenge		
No	Volume (cm^3)	Voxels [a]	pO_2 (Torr) Mean ± SD	HF_5 (%)	HF_{10} (%)	pO_2 (Torr) Mean ± SD	HF_5 (%)	HF_{10} (%)	pO_2 (Torr) Mean ± SD	HF_5 (%)	HF_{10} (%)
1	1.6	26	12 ± 3	24 ± 14	49 ± 15	56 ± 10	22 ± 2	29 ± 8	66 ± 3	0	0
2	0.3	10	12 ± 2	6 ± 12	53 ± 15	62 ± 15	0	0	79 ± 6	0	0
3	0.5	5	4 ± 4	60 ± 20	80 ± 0	14 ± 1	33 ± 12	53 ± 12	3 ± 1	73 ± 12	73 ± 12
4	1.3	14	< 1 torr [b]	100 ± 0	100 ± 0	14 ± 7	19 ± 11	48 ± 30	61 ± 21	0	0
5	0.9	24	24 ± 4	0 ± 0	8 ± 4	47 ± 10	0	0	71 ± 11	0	0
6	1.2	8	4 ± 1	58 ± 7	63 ± 0	43 ± 12	50 ± 22	63 ± 0	73 ± 10	0	0
7	0.8	24	27 ± 2	0 ± 0	3 ± 2	122 ± 21	0	0	142 ± 26	0	0
8	0.6	8	9 ± 6	50 ± 22	63 ± 22	103 ± 26	0	0	118 ± 37	0	0
9	0.7	44	25 ± 1	10 ± 5	26 ± 3	----	--	--	35 ± 3	0	3 ± 3
10	0.7	8	7 ± 6	54 ± 19	75 ± 22	52 ± 18	0	0	----	--	--
Mean ± SD	0.9 ± 0.4	17 ± 12	12 ± 10	36 ± 33	52 ± 31	57 ± 36 [c]	14 ± 1 [d]	21 ± 27	72 ± 41 [b]	8 ± 24 [b]	8 ± 24

[a] Number of voxels that provide acceptable data for all 23 pO_2 maps.
[b] $p<0.01$.
[c] $p<0.005$.
[d] $p<0.05$.

Table 2.2 Summary of vascular oxygen dynamics for the experimental tumors. Two amplitudes (A_1, A_2) and two time constants (τ_1, τ_2) were determined by curve-fitting the dynamic NIRS measurements using a double-exponential expression. Nine out of 10 tumors were observed to have double-exponential features with either oxygen or carbogen intervention. A_1 is significantly smaller than A_2 with oxygen ($p<0.01$), but no significant differences in carbogen ($p>0.19$).

Tumor		Double exponential fitting				
No.	intervention	A_1 (AU)	A_2 (AU)	τ_1 (min)	τ_2 (min)	R
[a]1	oxygen	0.11 ± 0.002	0.12 ± 0.002	0.49 ± 0.02	6.6 ± 0.2	0.94
	carbogen	0.15 ± 0.001	0.13 ± 0.002	0.58 ± 0.01	23.2 ± 1.1	0.94
[a]2	oxygen	0.03 ± 0.002	0.11 ± 0.005	0.46 ± 0.18	25.6 ± 2.9	0.91
	carbogen	----	----	----	----	----
[a]3	oxygen	0.15 ± 0.001	0.38 ± 0.003	0.31 ± 0.02	20.1 ± 0.39	0.98
	carbogen	0.23 ± 0.005	0.2 ± 0.004	1.2 ± 0.04	10.8 ± 0.45	0.95
[a]4	oxygen	----	----	----	----	----
	carbogen	0.16 ± 0.002	2.3 ± 0.27	0.29 ± 0.02	155.8 ± 21	0.97
[a]5	oxygen	0.12 ± 0.002	0.23 ± 0.002	0.55 ± 0.03	11.6 ± 0.27	0.94
	carbogen	----	----	----	----	----
[a]6	oxygen	0.06 ± 0.001	0.26 ± 0.005	0.13 ± 0.01	31.2 ± 1.1	0.96
	carbogen	0.03 ± 0.001	0.08 ± 0.001	0.04 ± 0.02	13.9 ± 0.6	0.78
[a]7	oxygen	----	----	----	----	----
	carbogen	----	----	----	----	----
[b]8	oxygen	0.11 ± 0.002	0.2 ± 0.001	0.24 ± 0.02	7.1 ± 0.1	0.96
	carbogen	0.2 ± 0.002	0.12 ± 0.001	0.49 ± 0.01	9.1 ± 0.2	0.95
[c]9	carbogen	0.01 ± 0.0004	0.02 ± 0.0004	0.14 ± 0.02	3.9 ± 0.12	0.64
[d]10	oxygen	0.05 ± 0.002	0.03 ± 0.002	0.46 ± 0.05	5.6 ± 0.56	0.68
Mean ± SD	----	0.11 ± 0.068	0.32 ± 0.59	0.42 ± 0.3	24.9 ± 40.2	----

[a]: air→O_2 →air →carbogen→air.
[b]: air → carbogen → air → O_2 → air.
[c]: air → carbogen → air.
[d]: air → oxygen → air.

2.3.3 The relationship between pO_2 and $\Delta[HbO_2]$ with respect to hyperoxic gas

Taken as a group of 10 tumors, there was no apparent relationship between the magnitude of the change in tumor vascular oxygenation ($\Delta[HbO_2]$) and change in pO_2 ($R^2<0.1$). However, if tumors were divided into two sub-populations, then two separate correlations were found each with similar slope (Figure 2.9). There was also a correlation ($R^2>0.7$) between the perfusion rate ratio, f_1/f_2, derived from fitting the $\Delta[HbO_2]$ curve and the mean pO_2 values achieved with hyperoxic gas intervention (figure 2.10). Assessment of f_1/f_2 is predicated on biphasic behaviour with respect to interventions, which was observed in most cases (13 of 16 measurements). There was also a positive correlation between A_1/τ_1 (the fast component of biphasic $\Delta[HbO_2]$) and the $d(pO_2)/dt$ of well oxygenated voxels (*i.e.*, those with pO_2 values > 10 torr under oxygen or carbogen intervention) ($R^2>0.5$, figure 2.11). However, no correlation was found between $d(pO_2)/dt$ and A_2/τ_2 (the slow component).

2.4 Discussion and conclusion

Integration of diverse imaging techniques can be technically challenging, since each modality has specific technical constraints and requirements. Here, the NIR system was modified to use longer optical fibers and any metal components were eliminated from the fibre tips. Due to the spatial restrictions within the bore of the magnet a Helmholtz coil was built specifically providing access to both the tumor and fibers. The fibers required sufficient flexibility to allow them to be bent through requisite angles

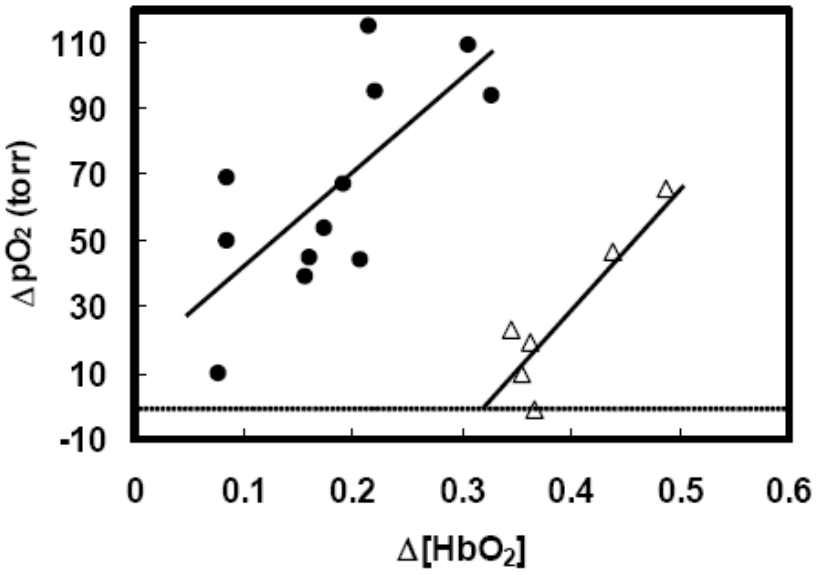

Figure 2.9 Correlation between maximum $\Delta[HbO_2]$ and change in pO_2 with respect to hyperoxic gas intervention for two groups of tumors (●) (group 1: #1, 2, 6, 7, 8, 9, 10; $R^2 > 0.51$) and (Δ) (group 2: #3, 4, 5; $R^2 > 0.82$). The unit for $\Delta[HbO_2]$ is mM/DPF. 6 of 7 of group 1 tumors had a high initial global pO_2 (*i.e.*, mean baseline pO_2 >5 torr), whereas 2 out of 3 of group 2 tumors on the right had low initial global pO_2.

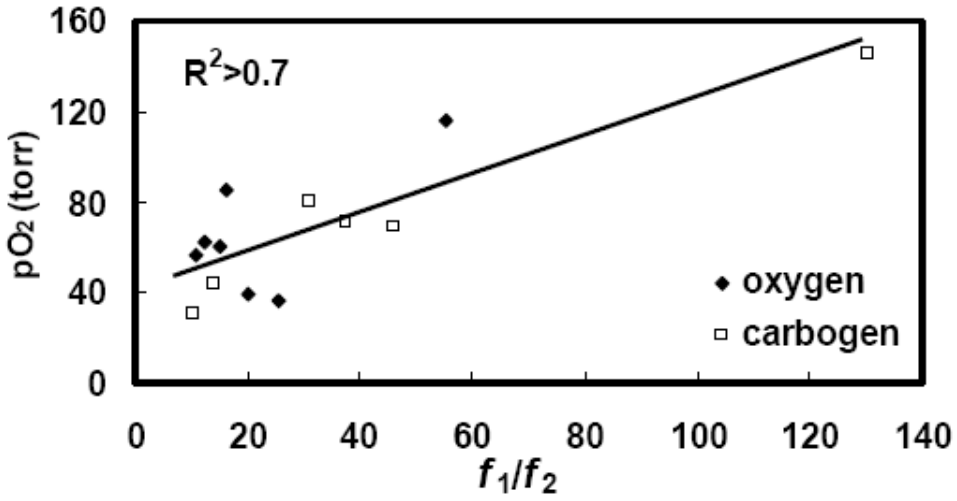

Figure 2.10 Correlation between mean pO_2 achieved with hyperoxic gas breathing and perfusion rate ratio (f_1/f_2) for tumors with biphasic response to intervention ($R^2>0.7$). pO_2 is the mean value for the final three pO_2 maps under hyperoxic intervention, selected from all voxels appearing in the final three pO_2 maps during oxygen (◆) or carbogen (□) intervention.

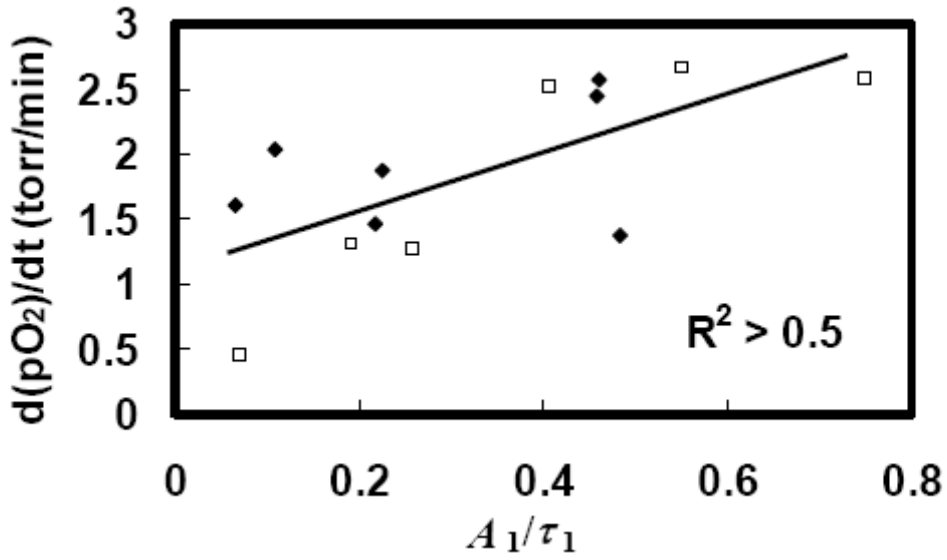

Figure 2.11 $d(pO_2)/dt$ vs A_1/τ_1 (determined from $\Delta[HbO_2]$ for tumors with biphasic response to interventions) showing a positive correlation ($R^2>0.5$). pO_2 values are the mean value of all well oxygenated voxels (*i.e.*, the maximum pO_2 > 10 torr under oxygen or carbogen intervention) appearing in the five pO_2 maps during oxygen (◆) or carbogen (□) intervention

within the confines of the magnet bore. To date there have been few reports of simultaneous data acquisition by NIR and MRI, *e.g.*, studies of phantoms [37], human brain [50, 51] and human breast [52-55].

In the present study, global average $\Delta[HbO_2]$ was measured by NIRS, and pO_2 maps were obtained simultaneously by ^{19}F MRI. I used transmission mode NIRS in order to interrogate deep tumor tissue. While NIRS is a global measurement, the region sampled by it is predominantly a banana-shaped region joining the locations of the source and detector [56, 57], and it was recently showed that typically 15 to 30% of the vascular volumes of rat tumors are interrogated by NIR using this configuration [58]. I positioned the NIRS probes (source and detector) to be in the same plane as the HFB

injection to ensure maximum overlap between the regions sampled by the two techniques. Utilising our previously developed mathematical model [16], multiple hemo-dynamic parameters were derived for $\Delta[HbO_2]$ (A_1/τ_1, A_2/τ_2 and f_1/f_2) to be compared with pO_2. The results demonstrate that oxygenation parameters measured from both techniques show significant and consistent elevation in tumor oxygenation during the hyperoxic gas interventions. As reported previously, the magnitude of the vascular response was similar with both hyperoxic gases [24]. As expected, $\Delta[HbO_2]$ increased much faster than pO_2 in all ten tumors, indicating that change in tumor vascular oxygenation precedes tumor tissue oxygenation. This observation is consistent with our previous studies in this tumor type measured simultaneously by NIRS and fiber-optic probes [24], as well in the Dunning prostate R3327-AT1 tumors measured sequentially by NIRS and ^{19}F MRI [42].

It have been previously demonstrated the application of *FREDOM* to monitor tumor oxygen dynamics in diverse rat prostate tumors [59, 60], human tumor xenografts [10] and a few breast tumors [46]. Here, mean baseline was $pO_2=12 \pm 10$ torr for the 10 tumors, which is lower than reported previously [46], but entirely consistent with the newer anaesthetic protocol (air or 21% oxygen, as opposed to 33% O_2 previously). There was a strong correlation between baseline pO_2 and hypoxic fraction (Figure 2.7), as we have previously found using Dunning prostate R3327-HI tumors [59]. The pO_2 achieved with carbogen in this study was significantly higher than with oxygen and carbogen appeared to be more effective at eliminating the hypoxic fraction (Table 2.1). However, carbogen was generally applied second in our experimental

protocols, and it is highly likely that the initial oxygen primed the tumor. Indeed, while oxyhaemoglobin generally returned to baseline during the air breathing episode between hyperoxic gases, it is clear that pO_2 remained elevated (Figure 2.2). Both ΔpO_2 and the maximum pO_2 achieved with either gas were closely correlated. Similar behaviour was reported previously based on measurements using fiber optic probes [24]. For the group of tumors in this study, mean baseline pO_2 did not provide a good indication of response to hyperoxic gas (ΔpO_2 or pO_{2max}). However, considering the fate of individual voxels in separate tumors with respect to intervention, strong linear correlation was observed in some tumors (tumor #3, 4, 6 and 9) between initial mean baseline pO_2 and the maximum pO_2 at the same location (voxel) in response to carbogen or oxygen breathing consistent with the results of Song *et al* [46]. Other tumors showed no correlation.

The rate of pO_2 response to either gas was similar (figure 2.8), but decrease upon return to air was significantly faster in the case of oxygen, but not carbogen. While the relationships between ΔpO_2 and $\Delta[HbO_2]$ are not obvious, there exists a significant correlation between f_1/f_2 and mean pO_2 values achieved with hyperoxic gas intervention. Most f_1/f_2 values are between 5 and 60 (figure 2.10), implying that the blood perfusion rate in the well perfused region is much higher than that from the poorly perfused region. Not surprisingly the higher the ratio of well-perfused to poorly-perfused regions, the higher the mean pO_2 values achieved by the hyperoxic gas interventions.

Previous studies have demonstrated that tumor tissue oxygenation could be strongly affected by changes in tumor blood flow measured locally by Laser Doppler

Flowmetry [61]. It was also reported that spontaneous fluctuations in flow and peri-vascular pO_2 are correlated at the on micro-regional level [62, 63]. In my study, I am able to derive the perfusion rate ratios between the well perfused and poorly perfused regions from the hemoglobin concentration responses to the intervention measured by NIRS. I found that there was a significant correlation between $d(pO_2)/dt$ and A_1/τ_1 (f_1, proportional to A_1/τ_1), but not $d(pO_2)/dt$ and A_2/τ_2 (f_2, proportional to A_2/τ_2), provided that the pO_2 readings were selected from well oxygenated or responsive voxels (figure 2.11). This linear correlation suggests that the rate of change in pO_2 is closely related to the perfusion rate in the well perfused region, f_1. In other words, the dynamic changes in pO_2 of those regions responsive to hyperoxic gas intervention may be attributed to fast tumor vascular perfusion, rather than to the slow perfusion in tumor vasculature. I believe these results provide a valuable association between tumor vascular oxygenation and tumor pO_2 determined simultaneously by the optical and NMR measurements.

A goal had been to develop a low-cost, simple, fast surrogate measurement of pO_2 based on NIRS of the oxygenation status of endogenous haemoglobin. Both figures 2.10 and 2.11 suggest that there exist linear relationships of pO_2 with the NIRS measurable parameters f_1/f_2 and with A_1/τ_1. However, the correlation between ΔpO_2 and $\Delta[HbO_2]$ (Figure 2.9) seems to be more complex with a separation of the tumors into two groups. It may be noteworthy that the majority (6 of 7) of the tumors associated with the correlation on the left hand side of the graph had a high initial global pO_2 (*i.e.*, mean baseline pO_2 >5 torr), whereas 2 out of 3 of the tumors on the right had low initial global pO_2. A possible interpretation relates to the shape of the hemoglobin-oxygen

dissociation curve (the Hill curve). A given pO_2 response can correspond to different changes in haemoglobin saturation depending on where the change occurs on the Hill curve. At lower initial pO_2 there may be a substantial ΔpO_2 with little $\Delta[HbO_2]$. By contrast, at higher initial pO_2 the same increase in pO_2 could produce a greater effect on the saturation. While $\Delta[HbO_2]$ is proportional to the change of sO_2 (with the assumption of little change in total haemoglobin concentration during intervention), two subpopulations of tumors in the relationship between ΔpO_2 and $\Delta[HbO_2]$ could be the result of different initial pO_2. Similarly, two subpopulations of tumors were observed in the relationship between initial sO_2 and the carbogen-induced change in saturation in the study of Hull *et al* [36]. Such an effect also confounds the direct correlation of BOLD MRI response to changes in pO_2 [64]. Significantly, preliminary data reported by Gu *et al* [55] for simultaneous BOLD MRI and NIR in tumors showed a strong linear correlation in response to hyperoxic gas challenge, as also reported by Chen *et al* [51] in the rat brain.

A major concern is tumor heterogeneity, as recognised throughout the literature and shown here by ^{19}F MRI (Figure 2.6). Indeed, we have obtained some preliminary data using a single NIR source and three detectors placed on various regions across a tumor [65], showing that each region of the tumor responded differently to hyperoxic gas, in terms of the extent and rate, indicating the heterogeneity of tumor vasculature. Spatial discrimination will be even more critical, if such studies are transferred to human breast cancer, where the tumor is surrounded by normal tissue [66]. Nevertheless, I believe this hemodynamic model and correlation between tumor

vascular oxygenation and pO_2 provides valuable insight into the tumor compartment of such a mixed system and explores dynamic signatures of breast tumors, which could, in turn, enhance/assist human breast cancer diagnosis and prognosis.

In summary, by studying tumor vascular oxygenation concomitantly with changes in tumor oxygen tension, I found several significant correlations between rates and magnitudes of vascular and tissue responses. This study also demonstrates the feasibility of conducting simultaneous NIRS and MRI oximetry. I believe the correlation of tumor vascular oxygenation and tumor tissue pO_2 can provide valuable insights into tumor pathophysiology and response to interventions.

CHAPTER 3

A MODEL OF HEMODYNAMIC RESPONSES OF RAT TUMORS TO HYPEROXIC GAS CHALLENGE

3.1 Introduction

Tumor oxygenation is a critical parameter to determine the efficacy of cancer therapies. Poorly perfused regions of tumors are hypoxic and thus resistant to radiotherapy. Accordingly, various approaches have been introduced to improve tumor oxygenation. The use of hyperbaric oxygen was an early example [67], and it continues to be studied in laboratory animal systems and in human clinical trials [68, 69]. Inhalation of high oxygen content gases, such as carbogen, has also been studied extensively [70-72].

Given the importance of tumor responses to hyperoxic gas intervention, many techniques have been developed to monitor changes in physiological parameters induced by the interventions, such as tumor oxygenation, tumor blood flow and tumor metabolic rate of oxygen. Regarding tumor oxygenation, various methodologies have been used to measure either oxygen partial pressure in tumor tissues or oxygen levels in tumor vasculature, using needle oxygen electrodes, optical reflectance, MRI, and nuclear medicine approaches, as reviewed previously [10, 73]. Near infrared spectroscopy (NIRS) has been developed in recent years as a promising non-invasive technique to improve tumor detection and characterization, and to assist with tumor

treatment planning and monitoring of tumor responses to therapy [74-76]. The intrinsic sensitivity of optical methods to oxygenated and deoxygenated hemoglobin, as well as water and lipid, makes them an attractive means to assess tumor oxygenation status, especially to monitor tumor vascular oxygenation with respect to interventions [76-78]. Among the techniques for monitoring tumor blood flow (TBF), Laser Doppler flowmetry (LDF) has been utilized for this purpose since 80s [79]. However, it is sensitive to artifacts and can only monitor TBF mostly in superficial vasculature [80-82]. Positron Emission Tomography (PET) provides quantitative measurements of the metabolic rate of oxygen ($TMRO_2$), but it is restricted by the number of repeated measurements with a limited temporal resolution [83, 84]. A previous optical spectroscopy study has utilized a theoretical model to associate the NIRS readings with cerebral blood flow and metabolic rate of oxygen during neural activation in humans so as to estimate these cerebral parameters [85]. Here, taking the similar modeling approach, I am investigating if NIRS can be used to estimate changes in tumor blood flow and tumor metabolic rate of oxygen non-invasively during hyperoxic gas intervention in rat tumors. Such a model will shed light on tumor vascular adaptation to therapeutic intervention, giving us a better understanding of physiological responses of tumors to intervention.

3.2 Materials and Methods

3.2.1 Animal and tumor model

Mammary adenocarcinomas 13762NF were surgically implanted in skin pedicles on the foreback of adult female Fisher 344 rats (~150 g), as described

previously [86]. Once the tumors reached ~1 cm in diameter, the rats were administered 150 μl ketamine hydrochloride (100 mg/ml; i.p.) and maintained under gaseous anesthesia with 1.3% isoflurane in air (1 dm^3/min), to immobilize the animal and to avoid stress associated with confinement. Body temperature was maintained at 37 ^oC by a warm water blanket. Air (20 min.), followed by carbogen (5% CO_2+95% O_2; 20 min.) or oxygen (20 min). Gas was administrated via a nose cone at a flow rate of 1 liter/min. The investigated rats were divided into two groups: group 1 (n= 6) administrated with air-oxygen-air, and group 2 (n= 5) with air-carbogen-air.

3.2.2 NIRS for measurement of changes in hemoglobin concentration

I used a homodyne frequency-domain system (NIM, Philadelphia, Pennsylvania) to measure the change in hemoglobin concentration. Briefly, the light from two laser diodes (758 nm and 785 nm) was coupled to a bifurcated fiber bundle for illumination of the tumor. The transmitted light was collected on the opposite side of tumor by another fiber bundle and propagated to a photomultiplier tube (PMT) for amplification. An In-phase and Quadrature (IQ) demodulator chip was used to demodulate the amplitude-modulated signal from PMT.

Based on the modified Beer-Lambert law, changes of oxy- and deoxy-hemoglobin concentration, Δ[HbO2] and Δ[Hb], respectively, can be derived from the measured amplitudes at the two wavelengths (758 nm and 785 nm), by using extinction coefficients of oxygenated or deoxygenated hemoglobin published by Kim [87]

$$\Delta[HbO_2] = \frac{-10.63\log(\frac{A_b}{A_t})^{758} + 14.97\log(\frac{A_b}{A_t})^{785}}{DPF \cdot d} \quad (3.1)$$

$$\Delta[Hb] = \frac{8.95\log(\frac{A_b}{A_t})^{758} - 6.73\log(\frac{A_b}{A_t})^{785}}{DPF \cdot d} \quad (3.2)$$

where A_b is the baseline amplitude, A_t is the transient amplitude during the intervention, and d is the direct source-detector separation. *DPF* (differential path-length factor) is a tissue-dependent parameter and defined as the ratio between the optical path length and the physical separation between the source and detector. Since *DPF* is a variable, depending on tissue types and wavelengths, it is currently difficult to quantify *DPF* for tumors. However, I may include *DPF* in the unit of [HbO_2] and [Hb] and still obtain characteristic features of tumor oxygen dynamics, since the study focuses on dynamic changes of hemoglobin concentration. After Δ[HbO_2] and Δ[Hb] are calculated, Δ[HbT] is the summation of Δ[HbO_2] and Δ[Hb].

3.2.3 Definition of $TMRO_2$

Tumor metabolic rate of oxygen (i.e. tumor oxygen consumption, $TMRO_2$) is simply given by the difference of the oxygen flowing into and out of a region. If I assume artery saturation SaO_2 =1, then the relative change of tumor metabolic rate of oxygen can be given by ratio method [88], as shown in equation 3.3:

$$(1 + \frac{\Delta TMRO_2}{TMRO_{2_0}}) = (1 + \frac{\Delta TBF}{TBF_0}) \cdot (1 + \gamma \frac{\Delta Hb}{Hb_0}) / (1 + \gamma_T \frac{\Delta HbT}{HbT_0}) \quad (3.3)$$

where γ and γ_T factors relates fractional hemoglobin changes in venous compartment to those across the vascular compartment.

$$\gamma = \left(\frac{\Delta[Hb]_v}{[Hb]_{v,0}} \right) / \left(\frac{\Delta[Hb]}{[Hb]_0} \right) \tag{3.4}$$

$$\gamma_T = \left(\frac{\Delta[HbT]_v}{[HbT]_{v,0}} \right) / \left(\frac{\Delta[HbT]}{[HbT]_0} \right) \tag{3.5}$$

In order to obtain $TMRO_2$ from equation 3.3, there are three unknowns on the right side of the equation. NIRS can provide the values of Δ[HbT] and Δ[Hb], but not ΔTBF. Therefore, I has to rely on some model which could be employed to estimate ΔTBF from Δ[HbT].

3.2.4 The Windkessel model used for estimating blood flow from Δ[HbT]

The Windkessel model relates blood flow to blood volume. With a few assumptions, I can thus estimate the blood flow response to intervention from the measured Δ[HbT] since Δ[HbT] is directly proportional to changes in blood volume. The Windkessel model is based on the conservation of mass to associate changes in blood volume with changes in blood flow through the regional arterial, capillary and venous compartments, with capillaries and veins lumped together and named a Windkessel compartment. The model proposes that the flow into the Windkessel compartment is largely determined by the vasomotor control of arterioles, and that the capillaries and veins passively respond to arterial pressure changes. Briefly described here, the model has the following definitions and relationships [89]:

1) between flow (*F*), pressure (*P*), and vascular resistance (*R*): *P(t)=F(t)R(t)*;

2) between Windkessel volume (*Vw*) and pressure (*Pw*): $Vw(t)=APw(t)^{1/\beta}$;

3) between Windkessel compartment resistance (*Rw*) and Windkessel volume: $Rw(t)/Rw(0)=(V(0)/Vw(t))^{\alpha}$;

4) arterial volume changes are related to the arterial resistance changes.

In the relationships given above, β represents the vascular compliance, α=2 indicates laminar flow with the vessel, *A* is a constant and equal to $Vw(0)/(F(0)Rw(0))^{1/\beta}$. With these definitions and initial conditions, the Windkessel model then arrives at the coupled differential equations, equations (3.6) and (3.7), for flow and volume changes due to arterial resistance changes [89], i.e.

$$\frac{\partial V_w(t)}{\partial t} = F_{in}(t) - F_{out}(t) = F_{in}(t) - \frac{V_w(t)^{\alpha+\beta}}{A^{\beta} R_w(0) V(0)^{\alpha}} \tag{3.6}$$

$$F_{in}(t) = \frac{P - P_w(t)}{R_A(t)} = \frac{P - V_w(t)^{\beta} / A^{\beta}}{R_A(t)} \tag{3.7}$$

In the study, I assume a bi-phasic model for the temporal response of arterial resistance during hyperoxic gas intervention according to the bi-phasic behavior of hemodynamic responses to oxygen or carbogen intervention [16], i.e.

$$R_A = R_{A,f}(0)\exp(-\frac{t-t_0}{\tau_f}) + R_{A,s}(0)\exp(-\frac{t-t_0}{\tau_s}) \tag{3.8}$$

where $R_{A,f}$ and $R_{A,s}$ are the amplitudes of fast and slow arterial resistance components, τ_f and τ_s are the time constants of fast and slow component, respectively, and t_0 is the time when the rats were exposed to the hyperoxic gas intervention. The numerical solutions of these differential equations, equations (3.6) and (3.7), then

provide the relationship between blood flow and blood volume. I normalized the units $F_{in}(0)=F_{out}(0)=1$, $V_w(0)=F_{in}(0)\tau$, and $R_A(0)+R_w(0)=1$.

In order to estimate the blood flow from blood volume changes, the value of $[HbT]_o$ and constant hematocrit have to be assumed during the intervention in order to establish the equation $\Delta[HbT]/[HbT]_o=\Delta BV/BV_o$. Based on the Windkessel model, I need to estimate four parameters for the arterial resistance, i.e., $R_{A,f}(0)$, $R_{A,s}(0)$, τ_f and τ_s, besides the Windkessel vascular reserve β and the Windkessel transit time τ. The model parameters were determined or optimized in a nonlinear fit to the experimentally measured Δ[HbT]. Given the optimal parameters, Windkessel model permits to estimate $\Delta TBF/TBF_o$.

3.3 Results

Figure 3.1 shows an example of time course of tumor Δ[HbT] and $\Delta[HbO_2]$, with thick lines, obtained by averaging six sets of measurements from group 1 tumors, when the rats were subject to oxygen intervention. Δ[HbT] and $\Delta[HbO_2]$ have stable baselines when the rats were breathing air. As the gas was switched to oxygen, both parameters increased consistently with the typical bi-phasic pattern. ΔTBF was estimated from Δ[HbT], based on the Windkessel model with equations (3.6) to (3.8). After ΔTBF was calculated, $\Delta TMRO_2$ was obtained using equation (3.3) with three known values, i.e. measured Δ[HbT] and $\Delta[HbO_2]$, comupted ΔTBF. Both ΔTBF and $\Delta TMRO_2$ have exhibited significant increases with a bi-phasic pattern too.

However, the tumors have various responses of Δ[HbT], ΔTBF, and $\Delta TMRO_2$ to carbogen inhalation (Fig 3.2 to 3.4), while tumor $\Delta[HbO_2]$ always show consistent

increases when given carbogen intervention (Fig 3.2 to 3.4). Figure 3.2 shows the time course of averaged $\Delta[HbO_2]$, $\Delta[HbT]$, computed ΔTBF and $\Delta TMRO_2$ from three tumors in group 2 (tumor #1~3) when the rats were subject to the gas intervention. In this case, there is a consistent increase of $\Delta[HbO_2]$ and $\Delta[HbT]$. It shows the increase of

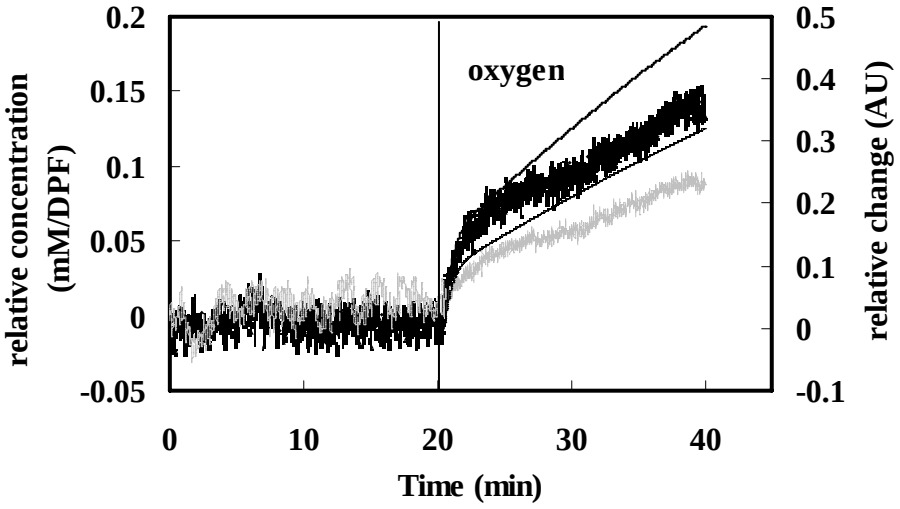

Figure 3.1 Time course of averaged values of $\Delta[HbT]$ (light thick curve), $\Delta[HbO_2]$ (dark thick curve), with computed ΔTBF (thin dotted curve) and $\Delta TMRO_2$ (thin dark curve), taken from six tumors with gas interventions of air-oxygen. The units of $\Delta[HbT]$ and $\Delta[HbO_2]$ are mM/DPF, and ΔTBF and $\Delta TMRO_2$ have arbitrary units.

ΔTBF, which was estimated from $\Delta[HbT]$ by utilizing the Windkessel model. A similar increase was observed for the corresponding $\Delta TMRO_2$. However, $\Delta[HbT]$ taken from tumor #4 from group 2 did not show much change, and neither did ΔTBF and $\Delta TMRO_2$ from this tumor in response to carbogen inhalation (Figure 3.3). Furthermore, Tumor #5 in group 2 shows a decreased $\Delta[HbT]$ induced by carbogen intervention, with reduced ΔTBF and $\Delta TMRO_2$ accordingly (Figure 3.4).

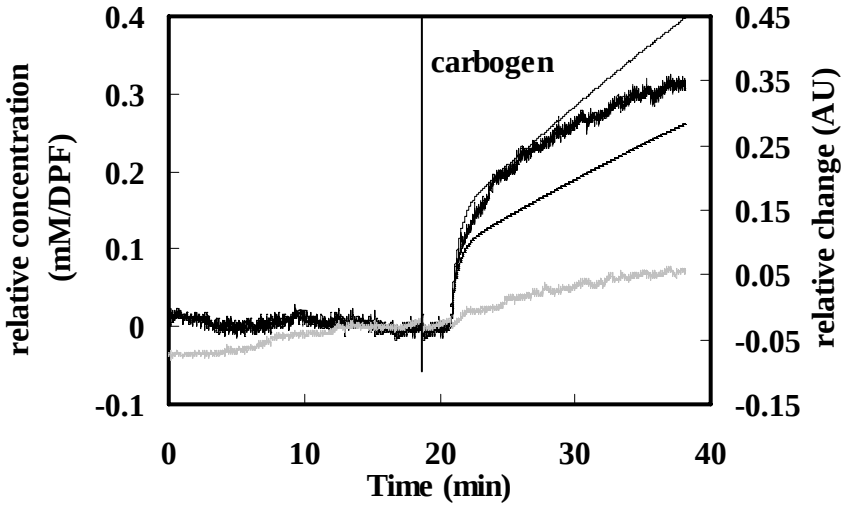

Figure 3.2 Time course of average values of Δ[HbT] (light thick curve), Δ[HbO_2] (dark thick curve), with computed ΔTBF (thin dotted curve) and Δ$TMRO_2$ (thin dark curve), from three tumors with gas interventions of air-carbogen. The units of Δ[HbT] and Δ[HbO_2] are mM/DPF, and ΔTBF and Δ$TMRO_2$ have arbitrary units.

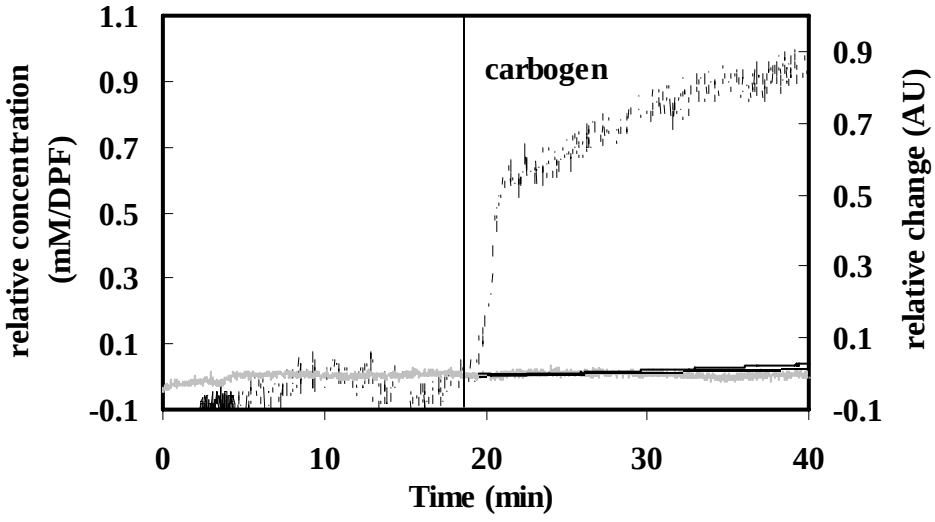

Figure 3.3 Time course of Δ[HbT], Δ[HbO_2], computed ΔTBF and Δ$TMRO_2$ from tumor 4 of group 2 with air-carbogen intervention.

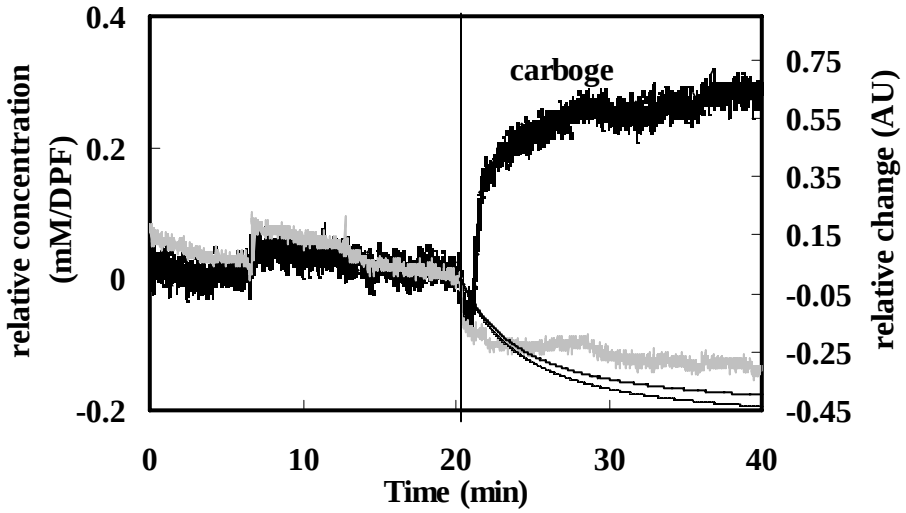

Figure 3.4 Time course of Δ[HbT], Δ[HbO_2], computed ΔTBF and Δ$TMRO_2$ from tumor 5 of group 2 with air-carbogen intervention.

3.4 Discussion and conclusion

In the present study, global tumor oxygenation was measured by NIRS during the administration of oxygen and carbogen. This technique enables us to measure relative changes in [HbO_2] and [HbT], but not in flow changes. Hence, it is necessary to rely on a mathematical model that relates changes in blood flow to changes in blood volume (i.e., total hemoglobin concentration) in order to estimate flow changes from the NIRS data. Boas et al had utilized the Windkessel model to fit a flow-volume relationship and estimated the relative changes of cerebral blood flow during brain activation [85], with a relatively good fit to the experimental data. Following the same strategy, I estimated the hyperoxic gas induced tumor blood flow changes by fitting the Windkessel model to the measured Δ[HbT], with the modification of physiological meaning of tumor vasculature. The bi-phasic feature of the computed blood flow is

consistent with the hypothesis that there exist two distinct regions within a tumor: 1) a well perfused region with a regular blood flow and 2) a poorly perfused region with slow blood flow. Song et al developed a model to calculate tumor oxygen consumption rate based on NIRS readings, but it requires to sacrifice rats to calculate the oxygen consumption rate [90].

The computed blood flow of rat tumors (n=6) shows a consistent increase, which may be induced by oxygen inhalation. However, it seems that carbogen breathing leads to various responses in ΔTBF: three tumors show improved ΔTBF, one with no change, and one with a decrease in ΔBF. Some evidence has indicated that, at least in some tumors, carbogen breathing may increase tumor blood flow and hence may lead to fluctuations in blood perfusion [91, 92]. In contrast, other studies have shown either a decrease or no change in blood flow during breathing of hyperoxic-hypercarbic gases [93, 94]. Our current results reveal all three possibilities, i.e., increase, no change or decrease of blood flow, during carbogen inhalation. Such variations may be due to tumor- or site-specific differences in the vasculature. Moreover, the computed $\Delta TMRO_2$ reveals the similar trend as the ΔTBF during hyperoxic gas intervention. All of these results, nevertheless, need to be further verified by simultaneous measurements of PET and NIRS in tumors, for the future study.

A major concern is tumor abnormal vasculature and perfusion, which are more complex than normal tissue. The flow-volume relationship in tumor may not be accurately represented simply by the Windkessel model, which has been used to describe the cerebral blood flow and volume relationship in brain activation [85, 89].

However, the bi-phasic feature of blood volume (i.e., total hemoglobin concentration) change during hyperoxic gas intervention provides a bridge to connect the computational model to our tumor data. I believe that the hemodynamic parameters, such as $\Delta[HbO_2]$, $\Delta[Hb]$ and $\Delta[HbT]$ directly measured from NIRS, ΔTBF and $\Delta TMRO_2$ indirectly estimated from NIRS, can provide valuable insight into the tumor compartment of such a complex system and allow us to explore dynamic signatures of tumors. All of these can, in turn, enhance/assist human cancer diagnosis and prognosis. Overall, NIRS is a noninvasive tool to monitor tumor oxygenation and may also serve as a mediator to estimate tumor perfusion and oxygen consumption rate with response to intervention in tumor tissue.

CHAPTER 4

TUMOR VASCULAR AND TISSUE OXYGEN DYNAMICS SIMULTANEOUSLY MONITORED BY NIRS AND FLUORESCENCE OXYGEN SENSOR IN RATS UNDER HYPERBARIC OXYGEN EXPOSURE

4.1 Introduction

As mentioned in chapter 1 and 2, tumor hypoxia has proven to have a prognostic impact in cancers and is associated with poor response to radiotherapy [25, 95]. Besides the normobaric inhalation, hyperbaric oxygenation was also employed to overcome tissue or tumor hypoxia. Several randomized studies investigating hyperbaric oxygenation as a radiosensitizer were performed 30-40 years ago [96, 97]. However, hyperbaric oxygenation was largely abandoned because of the hazard and complexity of irradiation under hyperbaric exposure. Recently, a few groups have developed and demonstrated a new strategy to combine hyperbaric oxygenation and radiotherapy, based on the finding that tumor oxygenation persisted even after hyperbaric oxygen intervention [98-101]. Therefore, accurate evaluation of tumor oxygenation in response to hyperbaric intervention could be crucial for determining the optimal time to perform radiotherapy.

Steady-state diffuse reflectance spectroscopy (SSDRS) is an effective technique for determining the optical absorption and scattering coefficients of biological tissues and other turbid media [102-104]. It has been developed in recent years as a promising non-invasive technique to determine the concentration of tissue chromophores, such as

oxygenated and deoxygenated hemoglobin [105, 106]. However, SSDRS currently lacks spatial resolution, and thus, the utility of global measurements require validation, given the well-documented heterogeneity of tumor oxygenation. Oxygen microsensors are powerful tools to monitor oxygen quantitatively and interrogate tumor microenvironment with high resolution reliably [107]. FOXY^{TM} fluorescence oxygen sensor can monitor regional oxygen tensions in multiple locations in tumors [59, 108, 109]. Simultaneous monitoring by both techniques provides complementary information of tumor oxygenation, i.e. both vascular and tissue oxygenation, in response to hyperbaric oxygen intervention.

I now applied two monitoring techniques simultaneously, i.e., steady-state diffuse reflectance spectroscopy to monitor tumor vascular oxygenation and a multi-channel FOXY^{TM} oxygen sensor to measure regional tumor oxygen tension when the rats were under a sequential hyperoxic gas intervention including hyperbaric oxygen. Furthermore, I measured the preservation of tumor oxygenation after hyperbaric oxygen exposure and compared it with the tumor oxygenation achieved with normobaric oxygen intervention. In this chapter, I investigated breast tumor oxygen dynamics in response to hyperbaric oxygenation and examined how long tumor oxygenation could persist after hyperbaric oxygenation.

4.2 Materials and Methods

4.2.1 Animal preparation and experimental setup

Female Fischer 344 rats were used with subcutaneously growing mammary adenocarcinoma 13762NF (originally obtained from DCT, NIH) on the dorsum of the

thigh. When the tumors reached ~1 cm in diameter, the rats were anesthetized with ketamine hydrochloride (1.5ml; 100mg/ml; Aveco, Fort Dodge, IA) and xylazine by intraperitoneal injection. Tumor hair was trimmed for the ease of optical contact for transmitting NIR light and FOXY^{TM} probe insertion. The rats were placed in the hyperbaric chamber on their sides, and probes of SSDRS and FOXY^{TM} were fixed securely on the tumor. FOXY^{TM} probes were threaded though 18 gauge needles which puncture tumor skin, and then inserted into different regions inside tumor. Tumor oxygenation parameters, $\Delta[HbO_2]$ and pO_2, were measured simultaneously by SSDRS and FOXY^{TM} during respiratory challenge with hyperbaric oxygen (HBO) or carbogen (HBCB).

During the experiments, the rats were placed inside the acrylic hyperbaric chamber. The chamber was flushed with air for 15 min, followed by normobaric 100% oxygen or carbogen for 15 min, and then the gas pressure was increased to 2 atm for 30 min. The chamber pressure was then reduced to ambient, followed by a flushing with air or oxygen. Gas exchange (air to oxygen/carbogen) was accomplished at an initial flow rate of approximately 15 l/min. Compression and decompression (from 1 to 2 atm oxygen/carbogen, and 2 to 1 atm oxygen/carbogen) required approximately 2 min. A total of seventeen rats were used in the study: six rats (group 1) were subjected to respiratory challenge in a sequence of air-oxygen-hyperbaric oxygen-air, five rats (group 2) breathed air-carbogen-hyperbaric carbogen-air, six rats (group 3) breathed air-oxygen-hyperbaric oxygen-oxygen-air.

4.2.2 Steady-state diffuse reflectance spectroscopy (SSDRS) for measuring changes in tumor vascular oxygenation (ΔHbO_2)

Broadband light diffuse reflectance spectrometer was used to acquire reflectance spectra from tumor tissue. Briefly, continuous wave (CW) light from a 20 W tungsten-halogen light source (HL-2000HP, ocean optics, FL) is coupled into a 2.6-mm core diameter fiber optic bundle, the distal end of which is placed in physical contact with the surface of the tumor. After being scattered in the tumor tissue, the transmitted light is collected by a 1-mm core diameter detection fiber, the end of which is coupled to a hand-held spectrometer (USB2000, Ocean optics, FL). The broadband light diffuse spectrometer provides reflectance spectra from 400 to 900 nm.

According to the modified Beer-Lambert law, as given in Equations (4.1) and (4.2), changes of oxy- and deoxy-hemoglobin concentration, $\Delta[HbO_2]$ and $\Delta[Hb]$, can be derived from the measured amplitudes at two wavelengths (750nm and 830nm), by using extinction coefficients of oxy- and deoxy-hemoglobin published by Cope [18].

$$\Delta[HbO_2] = \frac{-1.532\log(\frac{A_b}{A_t})^{750} + 1.753\log(\frac{A_b}{A_t})^{830}}{DPF \cdot d} \tag{4.1}$$

$$\Delta[Hb] = \frac{1.758\log(\frac{A_b}{A_t})^{750} - 0.92\log(\frac{A_b}{A_t})^{830}}{DPF \cdot d} \tag{4.2}$$

where A_b is the baseline amplitude, A_t is the transient amplitude during the intervention, and d is the direct source-detector separation. DPF (differential path-length factor) is a

tissue-dependent parameter and defined as the ratio between the optical path length and the physical separation between the source and detector.

4.2.3 FOXY™ oxygen sensor for measuring oxygen tension of tumors (pO_2)

FOXY™ fluorescence optical quenching system is a multi-channel oxygen sensor (Ocean Optics Inc, Tampa, FL). Each channel is composed of a LED light source, a spectrometer and a Y shape bifurcated optical fiber with the common end connected to FOXY™ AL-300 probes (tip diameter 410 μm). Prior to data recording, tips of AL-300 probes were inserted via 18 gauge needles, and gently move through the tumor to sample extracellular region of the tumors, as more details described by Vincent [110]. Light from a pulsed blue LED (475 nm) light source was coupled into one branch of a bifurcated optical fiber probe and propagated to the probe tip. The distal end of the probe is coated with a thin layer of a hydrophobic sol gel material, in which oxygen-sensing ruthenium complex is effectively trapped. Illumination of the ruthenium complex causes fluorescence at ~600 nm. If the excited ruthenium complex encounters oxygen molecule, the excess energy is transferred to the oxygen molecule, thus quenching the fluorescence signal. The degree of quenching correlates with the oxygen concentration, pO_2.

4.3 Results

The reading of FOXY™ oxygen sensor is consistent with the partial pressure of oxygen, not ambient pressure. As showed in figure 4.1, the corresponding pO_2 readings measured from oxygen sensor change in proportional to the actual pO_2 value when the gas (5% O_2 + 95% N_2) in the chamber was pressurized to 1, 1.2, 1.4, 1.6, 1.8 and 2 atm.

Typical time profiles of $\Delta[HbO_2]$, pO_2 in response to respiratory challenge are shown for a representative 13762NF breast tumor (2.5 cm^3) in figure 4.2. This tumor showed a rapid response to 1 atm oxygen intervention with a significant increase in $\Delta[HbO_2]$. pO_2 readings from three regions indicated tumor heterogeneous responses with respect to normobaric oxygen inhalation. One region had distinct improvement in pO_2, while the other two regions had less improvement in pO_2. After oxygen was pressurized to 2 atm, $\Delta[HbO_2]$ had a further increase, while pO_2 readings in all three regions showed significant improvement under hyperbaric oxygen exposure. Returning to normobaric oxygen from hyperbaric oxygen caused a gradual decline for both $\Delta[HbO_2]$ and pO_2. Three pO_2 readings reached to stable levels in different rates, but all faster than $\Delta[HbO_2]$. When switching gas from oxygen back to air, both $\Delta[HbO_2]$ and pO_2 value have further decrease with similar rates.

Tumor oxygen tension has significant improvement in response to normobaric hyperoxic gas intervention ($p<0.05$) for all 17 tumors. Hyperbaric oxygen/carbogen produced further significant increase ($p<0.05$) in pO_2 in comparison with normobaric oxygen/carbogen (table 4.1). For tumors in group 1, 15 min after the hyperbaric gas was switched back to air, pO_2 was still significantly greater ($p<0.05$) than that in baseline air. For tumors in group 2, 20 min after the hyperbaric gas was switched back to air, pO_2 was significantly greater than that in baseline air ($p<0.05$). pO_2 of 10 min post second normobaric oxygen/carbogen administration has a decrease, but the value is not significantly greater than pO_2 achieved with first normobaric oxygen/carbogen before hyperbaric oxygen/carbogen ($p>0.08$). Continuing breathing normobaric oxygen after

hyperbaric oxygen could not sustain the high tumor oxygen tension achieved with hyperbaric oxygen. Indeed, pO_2 of tumors in group 3 after 10 min normobaric oxygen inhalation (second normobaric oxygen after hyperbaric oxygen intervention) has a value

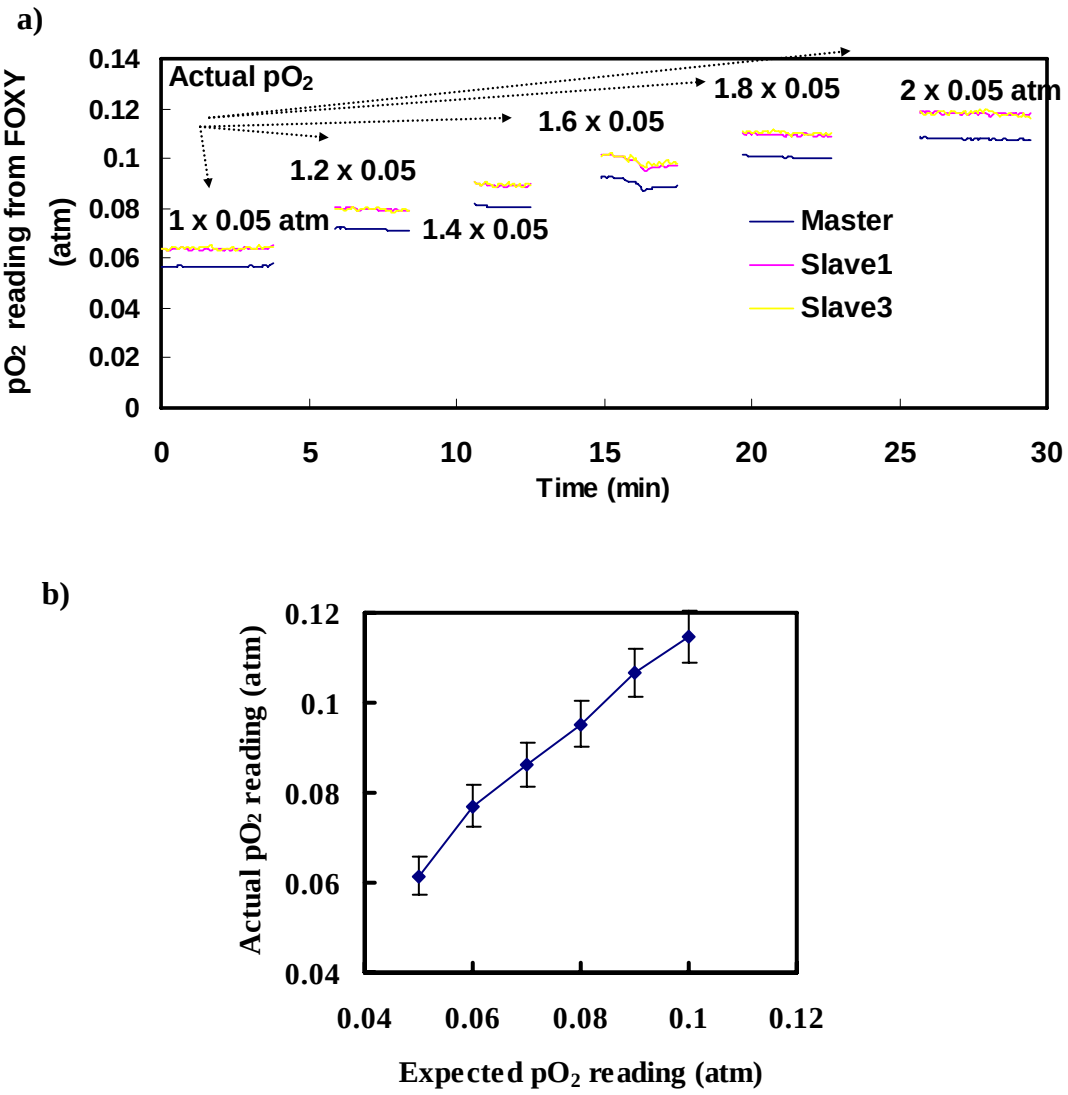

Figure 4.1 (a) pO_2 readings measured from three channels, master channel (blue), slave1 channel (pink) and slave 3 (yellow) of FOXY^{TM} oxygen sensor and (b) the relationship between expected pO_2 readings and actual pO_2 readings measured from oxygen sensor, when the gas (5% O_2 + 95% N_2) in the chamber was pressurized to 1, 1.2, 1.4, 1.6, 1.8 and 2 atm. The actual pO_2 readings are averaged from pO_2 readings of three channels.

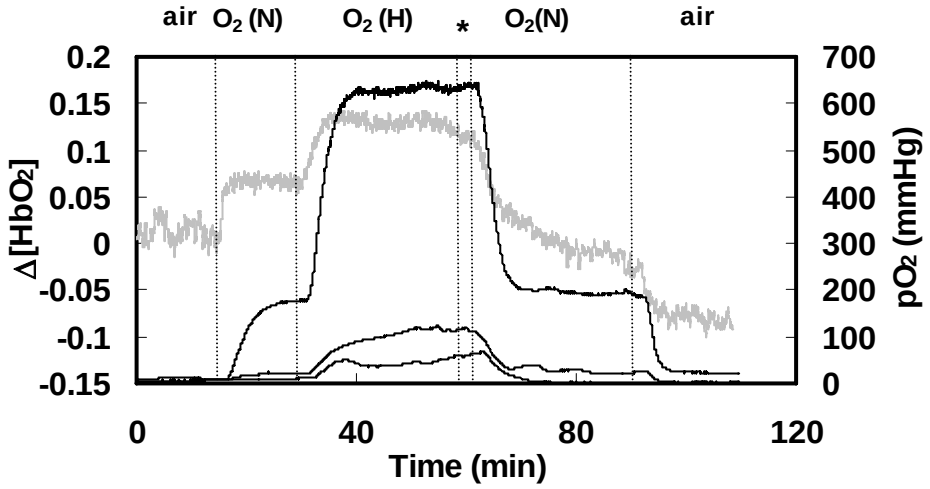

Figure 4.2 Time course of $\Delta[HbO_2]$ and pO_2 in response to respiratory challenge for a representative tumor, simultaneously measured by SSDRS (thicker and lighter curve) and FOXY^{TM} (thinner and darker curves). O_2 (N) represents normobaric oxygen inhalation, O_2 (H) represents hyperbaric oxygen inhalation. The symbol "*" represents the time needed for decompression.

similar to the maximal value of pO_2 achieved with 15 min normobaric oxygen inhalation (the one before hyperbaric intervention) (p=0.5).

Figure 4.3 is pooled data showing the relationship between pO_2 in baseline air and relative change achieved with normobaric/hyperbaric oxygen intervention. ΔpO_2 in HBO is significantly greater than those in NBO. There was a strong correlation (R^2=0.78) between maximal change of tumor oxygen tension achieved with hyperbaric oxygen/carbogen intervention and that achieved with normobaric oxygen/carbogen intervention in 17 tumors (Figure 4.4a). By examining point by point in Figure 4.4a, there is 26% pO_2 reading with significant increase ($\Delta pO_2 > 5$ mmHg) under hyperbaric hyperoxic exposure but few change ($\Delta pO_2 < 5$ mmHg) under normobaric intervention. In other words, 26% regions sampled by FOXY^{TM} probes have significant improvement

Table 4.1 Variation of oxygen tension (pO_2) in individual rat mammary 13762NF adenocarcinomas in response to gas intervention. pO_2 value in baseline air is significantly less than that achieved in normobaric oxygen/carbogen, hyperbaric oxygen/carbogen, 10 or 15 min after hyperbaric oxygen/carbogen for rats in three groups.

Group	No	Baseline(air)	NBO	HBO	10 min after HBO	15 min after HBO	20 min after HBO
1	6	11.69 ± 2.6	17.5 + 4.0*	58.9 + 21.3*	21.48 + 4.6*	16.89 + 3.1*	14.26 + 2.4
2	5	7.42 ± 1.5	17.54 + 3.8**	105.6 + 25.7*	21.21 + 6.3*	14.39 + 3.3*	12.36 + 2.3*
3	6	13.17+ 2.2	45.15 + 13.2**	162.4 + 44.2*	44.81 + 13.3*	41.7 + 12.8*	41.07 + 12.4*

* $p<0.05$
** $p<0.005$

in pO_2 during hyperbaric oxygen/carbogen intervention, whereas no significant increase achieved during normobaric oxygen/carbogen intervention. The maximal $\Delta[HbO_2]$ achieved with normobaric hyperoxic gas was also correlated with that under hyperbaric hyperoxic gas exposure (R^2=0.65, figure 4.4b).

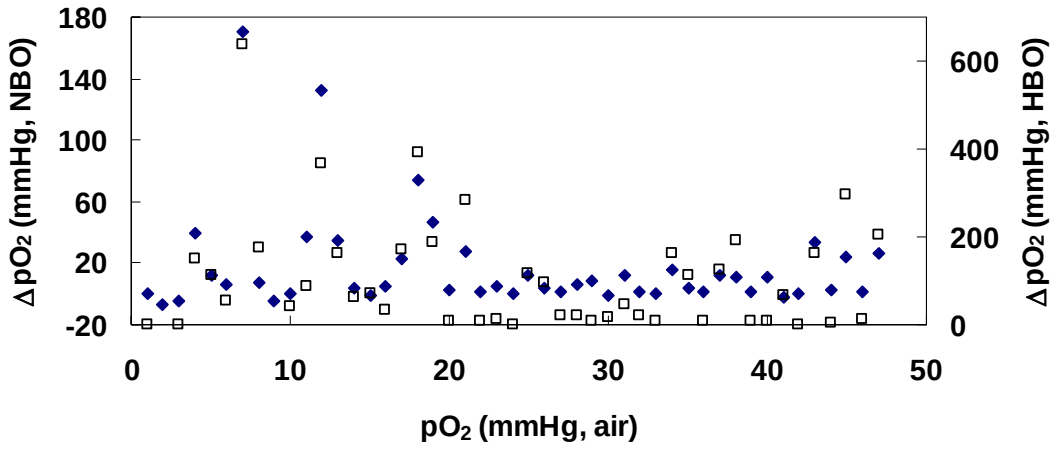

Figure 4.3 pO_2 values in baseline air versus relative change in pO_2 achieved during normobaric oxygen (◆) and hyperbaric oxygen (□) intervention in 17 tumors.

There is correlation (R^2=0.52) between change of pO_2 and maximal $\Delta[HbO_2]$ with respect to normobaric oxygen/carbogen for 17 tumors (Figure 4.5), while there is no correlation (R^2=0.15) between change of pO_2 and maximal $\Delta[HbO_2]$ with respect to hyperbaric hyperoxic gas intervention (Figure 4.6).

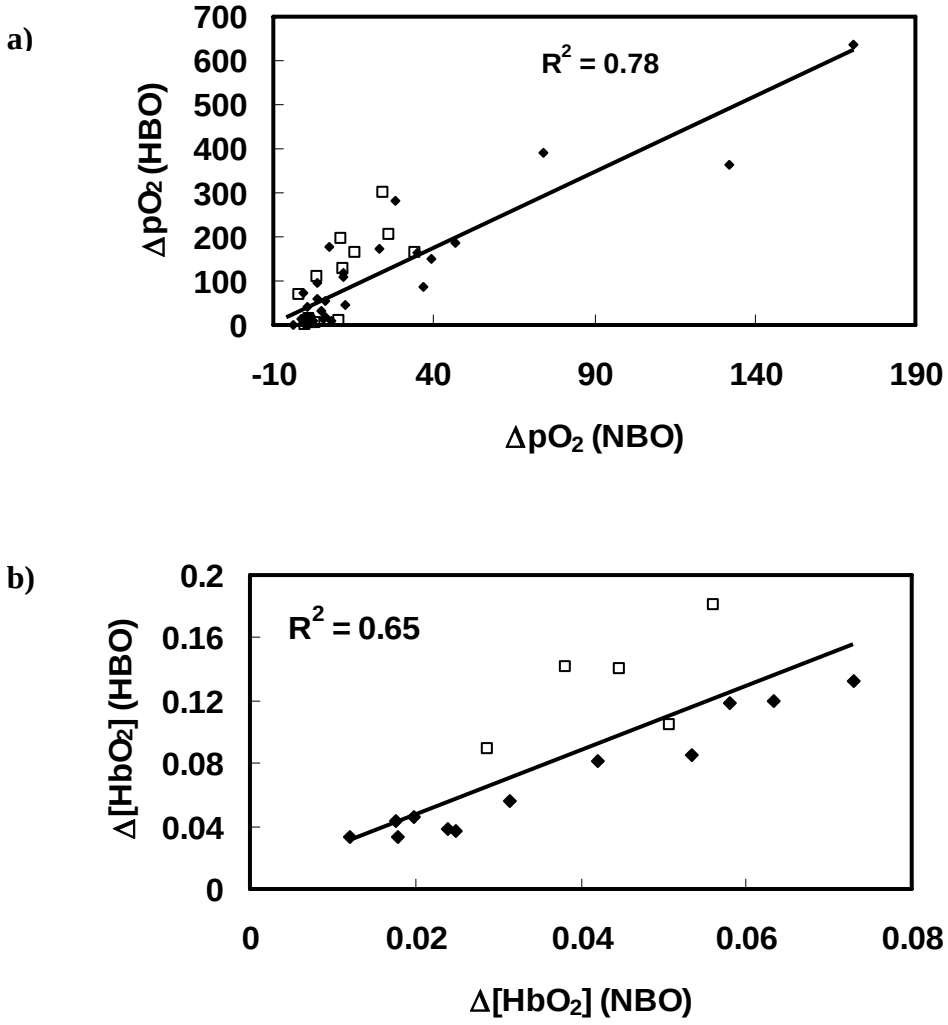

Figure 4.4 Correlation between maximal change of (a) pO_2 and (b) $\Delta[HbO_2]$ during normobaric and hyperbaric oxygen/carbogen inhalation for tumors with oxygen (◆) or carbogen (□) intervention. The unit for $\Delta[HbO_2]$ is mM/DPF.

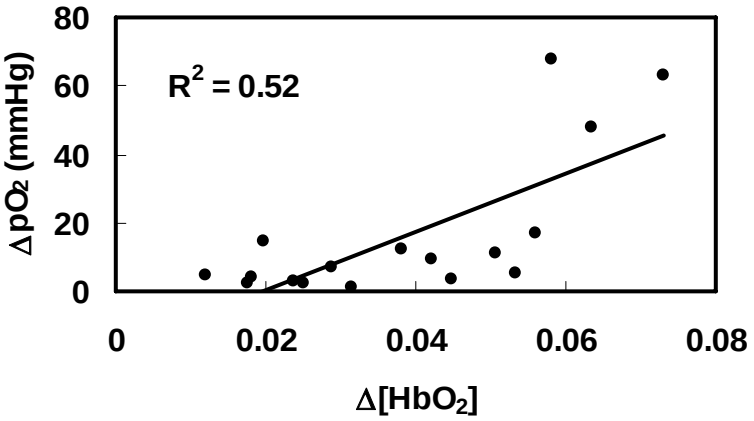

Figure 4.5 Correlation between change of pO_2 and maximal $\Delta[HbO_2]$ with respect to normobaric oxygen/carbogen intervention for 17 tumors. The unit for $\Delta[HbO_2]$ is mM/DPF.

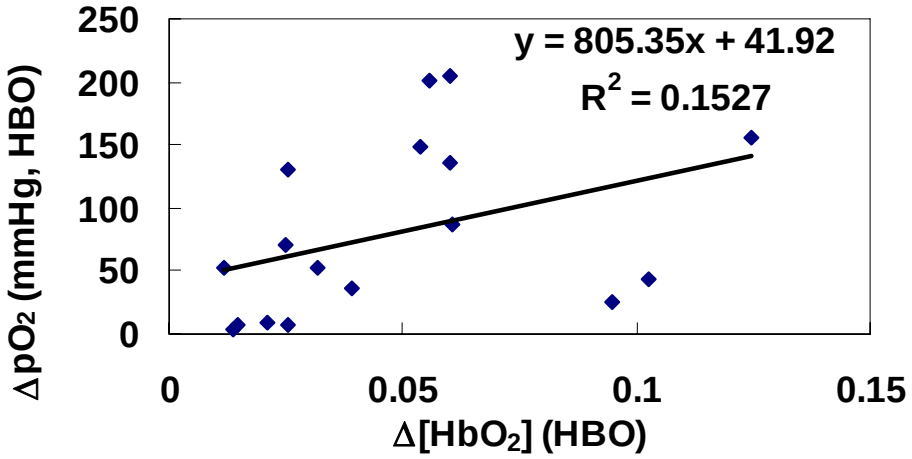

Figure 4.6 Relationship between maximal change in averaged pO_2 and maximal $\Delta[HbO_2]$ with respect to normobaric oxygen/carbogen interventions for 17 tumors. The unit for $\Delta[HbO_2]$ is mM/DPF.

4.4 Discussion and Conclusion

In the present study, global average $\Delta[HbO_2]$ was measured by SSDRS, and regional pO_2 were obtained simultaneously by a multi-channel FOXY™ fluorescence optical quenching system, in response to hyperbaric oxygen/carbogen intervention. I used

transmission mode NIRS in order to interrogate deep tumor tissue. Two oxygen-sensitive indicators showed similar dynamic changes in response to gas interventions. The simultaneous measurements demonstrate that the two techniques, i.e., SSDRS and FOXY, are consistent and complementary with one another for tumor oximetry. Both systems are relatively inexpensive and provide real-time measurements. The results indicate that oxygenation parameters measured from both techniques have significant and consistent elevation in tumor oxygenation during both normobaric and hyperbaric oxygen/carbogen interventions in this tumor type. As expected, $\Delta[HbO_2]$ increased much faster than pO_2 in all tumors, indicating that change in tumor vascular oxygenation precedes tumor tissue oxygenation. The current data also showed that $\Delta[HbO_2]$ and ΔpO_2 in response to normobaric oxygen/carobogen intervention are correlated with each other (Figure 4.5), which is consistent with results in MRI-NIRS study (Figure 2.9). Therefore, it implied that NIRS reading may be used to predict the tumor tissue in response to therapeutic gas intervention. Both observations are consistent with our previous studies in the same tumor type measured simultaneously by NIRS and ^{19}F MRI [111], as well as by NIRS and fiber-optic probes [24]. However, $\Delta[HbO_2]$ and ΔpO_2 in response to hyperbaric hyperoxic gas intervention are not significantly correlated. Hence, it demonstrates that the further improvement of pO_2 during hyperbaric gas intervention is contributed to the increased amount of dissolved oxygen molecule in plasma, rather than oxygen molecule transported by hemoglobin.

Previous studies have demonstrated that hyperbaric hyperoxic gas intervention improved tumor oxygen tension in mammary adenocarcinomas (R3230Ac), while

normobaric oxygen and carbogen did not change tumor oxygenation significantly [112]. In my current tumor model, both normobaric and hyperbaric oxygen/carbogen improve tumor oxygenation (Table 4.1). Moreover, hyperbaric oxygen/carbogen results in much more significant improvement in tumor oxygenation than normobaric oxygen/carbogen. It is clinically important for the oxygen tension of those tumor regions, which could be significantly improved by hyperbaric oxygen/carbogen, but not by normobaric oxygen/carbogen.

Preservation of pO_2 after hyperbaric oxygen in tumors has been recently studied by several groups [100, 113]. Their results indicated that tumor oxygen decreased gradually and remained at a high level tens of minutes after HBO exposure, while NBO group showed no significant change after NBO exposure. It was also observed that an improvement in tumor tissue oxygenation achieved by hyperbaric oxygenation may persist over 10-20 minutes even after ending hyperbaric oxygenation intervention. However, a major concern is whether the persistence of tumor oxygenation some time after ending HBO can still achieve greater values than those with normobaric oxygen intervention. Indeed, I found that the tumor oxygenation of 10 min post HBO was not significantly higher than oxygenation achieved with normobaric oxygen prior to HBO. The result may suggest that having irradiation after HBO exposure may not be superior to performing radiotherapy during normobaric oxygen intervention.

In summary, by studying tumor vascular oxygenation concomitantly with changes in tumor oxygen tension, I found several correlations for both modalities under sequences of normobaric and hyperbaric hyperoxic gas intervention. This study also

demonstrates the feasibility of conducting simultaneous SSDRS and FOXY^{TM} oxygen sensor under hyperbaric oxygen exposure. I believe both tumor vascular and tissue oxygenation can provide valuable insights into tumor pathophysiology and response to intervention.

CHAPTER 5

TUMOR VASCULAR OXYGENATION MONITERED BY NIRS IN RATS WITH HYPERBARIC OXYGEN INTERVENTION IN COMBINATION WITH DOXORUBICIN TREATMENT

5.1 Introduction

Doxorubicin (DOX) is one of the most widely used broad-spectrum anticancer agents [114]. However, its clinical utility is limited, because this agent produces a chronic and dose-related cardiomyopathy as its principal side effect. Therefore, it is desirable to achieve better chemotherapeutic effect with lower dosage of the agent. It is well accepted that hypoxic tumor is resistant to radiotherapy and some chemotherapy agent [27, 115-117]. To overcome hypoxia, a variety of approaches have focused on improve oxygen delivery via oxygen-enriched gases or blood substitutes [25, 96, 118-120]. Hyperbaric oxygen was believed to improve tissue oxygenation greater than normabric oxygen because it increased oxygen tension and oxygen delivery to tissue independent of hemoglobin[121]. HBO, as a chemotherapy adjuvant in tumor treatment rather than stand alone treatment, is believed to increases cellular uptake of some chemotherapy agents and the susceptibility of cells to these agents. It has been demonstrated that HBO can increase the susceptibility of malignant cells to destruction with taxol [21], doxorubicin [20, 21] and 5-FU [22, 122].

The influence of tumor oxygenation on treatment outcome has stimulated various techniques to monitor or estimate tumor oxygenation. These include

microelectrodes, optical reflectance, electron paramagnetic resonance (EPR), magnetic resonance imaging (MRI) and nuclear medicine approaches, as reviewed previously [10, 73]. As each approach has their own strength, some are highly invasive. Since its introduction in 1970s[123], Near Infrared Spectroscopy has been increasingly applied to study tissue oxygenation status non-invasively. Near infrared light can easily penetrate biological tissue, and allow for detection of specific light-absorbing chromophores in human in vivo, such as oxygenated and deoxygenated hemoglobin, water and lipid [16, 32]. it has been used extensively for quantitative measurements of cerebral oxygenation [33, 34] and blood oxygenation in muscles *in vivo* [35], and more recently, tumor vascular oxygenation with respect to interventions [16, 24, 36, 124]. NIRS currently lack of spatial resolution, and thus, the utility of global measurement require validation, given the well-documented heterogeneity of tumor. In this regard, Xia *et al* [124] compared the spatially averaged measurement of relative tumor oxygen saturation ($_SO_2$) using NIRS with the local pO_2 measured by MRI. The sensitivity and specificity analysis suggests that NIRS may identify clinically relevant hypoxia, even when its spatial extent is below the resolution limit of the NIRS technique. Kim *et al* demonstrated that NIRS may be used as an effective tool to monitor tumor hemodynamic change induced by some vascular disrupting agent [125, 126].

These studies were designed to investigate 1) whether HBO could enhance the therapeutic efficiency of malignancy when used as a chemotherapeutic adjuvant of doxorubicin in mammary carcinomas of rat model, and 2) the feasibility of NIRS to

monitor tumor hemodynamic changes resulting from the therapeutic effect of DOX on vasculature.

5.2 Materials and Methods

5.2.1 Animal and Tumor models

Healthy female Fischer 344 rats aged 5 to 6 months were obtained from Harlan Sprague-Dawley (Indianapolis, IN). They were housed for at least a week to acclimatize and for monitoring of health before inclusion in the study. Mammary carcinomas 13762NF were implanted in the dorsum of female Fischer 344 rats weighing ~200g. Tumor volume was estimated by the formula of 6/pi *(LxWxH), Tumor diameter was measured in orthogonal axes (L,W, H). Tumor size and body weight were monitored every other day after therapeutic interventions. All animal protocols were approved by Institutional Animal Care and Use Committee at the University of Texas Southwestern Medical Center and University of Texas at Arlington.

5.2.2 Drug preparation and dose

Doxorubicin Hydrochloride was purchased from Sigma Aldrich, Inc. It was made into a solution by dissolving with saline. A single dose of DOX (2mg/kg body weight) was administrated by tail vein. The dose of doxorubicin given was the usual chemotherapeutic dose, which would not cause cardio-toxicity [20].

5.2.3 Experimental procedure

Following tumor establishment (~1 cm diameter), rats were randomly assigned to one of three groups according to different therapeutic strategies: a) DOX (n=5), b) HBO + DOX (n=5). C) control group (n=2) with saline injection. Rats were

anesthetized with the mixture of ketamine hydrochloride (0.15 ml; 100mg/ml; Aveco, Fort Dodge, IA) and xylazine via i.p. After tumor hair was shaved to allow better optical contact for NIR light transmission, the rat was placed on its side in the hyperbaric chamber. Probes of SSDRS were fixed securely on the tumor of rat, and then SSDRS monitored tumor vascular oxygenation while the rat was subjected to therapeutic interventions.

DOX group was given 0.4 mg/ml doxorubicin solution intravenously after the respiratory intervention of air -O_2 - air, and then were exposed to air – O_2 - air after DOX injection. HBO + DOX group was exposed to gas intervention in a sequence of air-O_2 - HBO (30 min) prior to intravenously administration of 0.4 mg/ml doxorubicin solution, and then exposed to air - O_2 – air. Control group was subjected to the respiratory intervention of air -O_2 - air, saline solution intravenous injection and then were exposed to air – O_2 – air. To control the timing of DOX injection, an IV butterfly catheter was inserted into rat tail vein and fixed securely with tape before the rat was put into the chamber. The syringe filled with DOX solution was connected to the catheter with heparin only before DOX injection, in order to avoid the possible precipitation caused by the incompatibility of DOX and heparin [127].

5.2.4 Spectrometer for monitoring the disturbance of DOX on the absorption of tissue phantom

Because the reddish color of doxorubicin, it is reasonable to consider the bolus injection of doxorubicin may change tissue absorption. A UV/VIS spectrometer Lambda 20 (PerkinElmer Inc., Waltham, MA) was used to detect the absorption change resulting from the addition of DOX into tissue phantom, in order to verify the acute

effect of DOX bolus injection on tissue absorption. A tissue phantom is composed of 100 μl sheep blood mixed with phosphate buffer solution with total volume of 3.5 ml and total hemoglobin concentration of 7.1 g/L, which is in the range of total hemoglobin concentration in tissue [128]. The Hb concentration of tissue phantom was measured by Co-oximeter (Instrumentation Lab, Ramsey, MN). Since animal's total blood volume is 10% of its body weight, total blood volume = 0.2 Kg x 10% = 20 ml, with the known body weight of ~ 0.2 Kg of rats. 0.17 ml DOX solution with the concentration of 0.4 mg/ml was added into the tissue phantom. Accordingly, the volume ratio of DOX to tissue phantom is proportional to the ratio of 1 ml 0.4 mg/ml DOX to 20 ml total blood volume in rats. According to the Lambert Beer Law, the absorption in 750nm and 830nm are

$$A^{750}(0) = \varepsilon_{Hb}{}^{750}[Hb] + \varepsilon_{HbO_2}{}^{750}[HbO_2] \tag{5.1}$$

$$A^{750}(1) = \varepsilon_{Hb}{}^{750}[Hb] + \varepsilon_{HbO_2}{}^{750}[HbO_2] + \varepsilon_{DOX}{}^{750}[DOX] \tag{5.2}$$

$$A^{830}(0) = \varepsilon_{Hb}{}^{830}[Hb] + \varepsilon_{HbO_2}{}^{830}[HbO_2] \tag{5.3}$$

$$A^{830}(1) = \varepsilon_{Hb}{}^{830}[Hb] + \varepsilon_{HbO_2}{}^{830}[HbO_2] + \varepsilon_{DOX}{}^{830}[DOX] \tag{5.4}$$

where A^{750} (0) and A^{750} (1) represent the absorption at 750 nm in tissue phantom without DOX and with DOX, respectively. A^{830} (0) and A^{830} (1) represent the absorption at 830 nm in tissue phantom without DOX and with DOX, respectively.

5.2.5 Steady-state diffuse reflectance spectroscopy (SSDRS) for measuring changes in tumor vascular oxygenation (ΔHbO_2)

A broadband diffuse reflectance spectrometer was used to acquire reflectance spectra from tumor tissue. Briefly, continuous wave (CW) light from a 20 W tungsten-halogen light source (HL-2000HP, ocean optics, FL) is coupled into a 2.6-mm core diameter fiber optic bundle, the distal end of which is placed in physical contact with the surface of the tumor. After being scattered in the tumor tissue, the transmitted light is collected by a 1-mm core diameter detection fiber, the end of which is coupled to a hand-held spectrometer (USB2000, Ocean optics, FL). The broadband light diffuse spectrometer provides reflectance spectra from 400 to 900 nm.

According to the modified Beer-Lambert law, changes of oxy- and deoxy-hemoglobin concentration, $\Delta[HbO_2]$ and $\Delta[Hb]$, can be derived from the measured amplitudes at two wavelengths (750nm and 830nm), by using extinction coefficients of oxy- and deoxy-Hb published by Cope [18], as given in Equations. (5.5) and (5.6)

$$\Delta[HbO_2] = \frac{-1.532 \log(\frac{A_b}{A_t})^{750} + 1.753 \log(\frac{A_b}{A_t})^{830}}{DPF \cdot d} \tag{5.5}$$

$$\Delta[Hb] = \frac{1.758 \log(\frac{A_b}{A_t})^{750} - 0.92 \log(\frac{A_b}{A_t})^{830}}{DPF \cdot d} \tag{5.6}$$

where A_b is the baseline amplitude, A_t is the transient amplitude during the intervention, and d is the direct source-detector separation. DPF (differential path-

length factor) is a tissue-dependent parameter and defined as the ratio between the optical path length and the physical separation between the source and detector.

5.3 Results

5.3.1 Disturbance of DOX on the absorption of tissue phantom

There is absorption difference between tissue phantom with and without DOX, as shown in Figure 5.1. However, the differences are relatively small. Indeed, the relative changes of absorption in wavelength of 750nm and 830nm are $\frac{A^{750}(1)-A^{750}(0)}{A^{750}(0)}$=4.85% and $\frac{A^{830}(1)-A^{830}(0)}{A^{830}(0)}$=4.80%, respectively. In order to investigate the disturbance of DOX on calculating oxygen saturation, absorption spectrum profiles between 700 and 900 nm were normalized by absorption values at the wavelength of 700 nm. The normalized spectra cover the wavelengths we utilized for

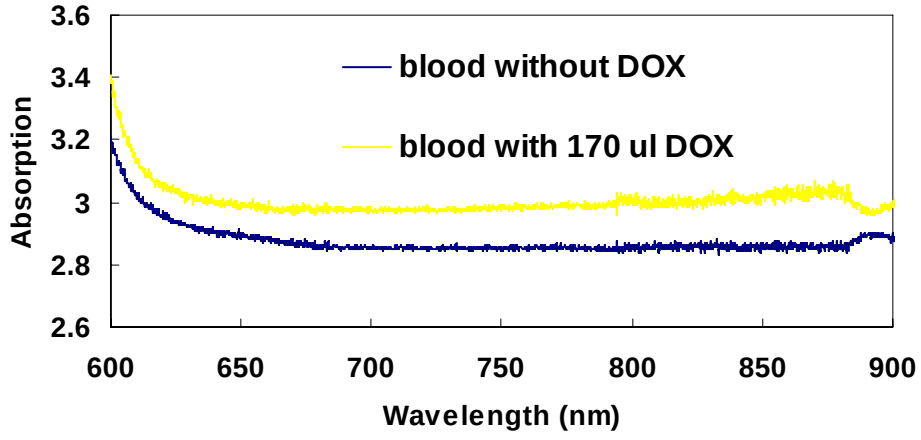

Figure 5.1 Absorption spectra of tissue phantoms with (yellow curve) or without 170 μl DOX (blue curve). The unit for absorption is arbitrary unit.

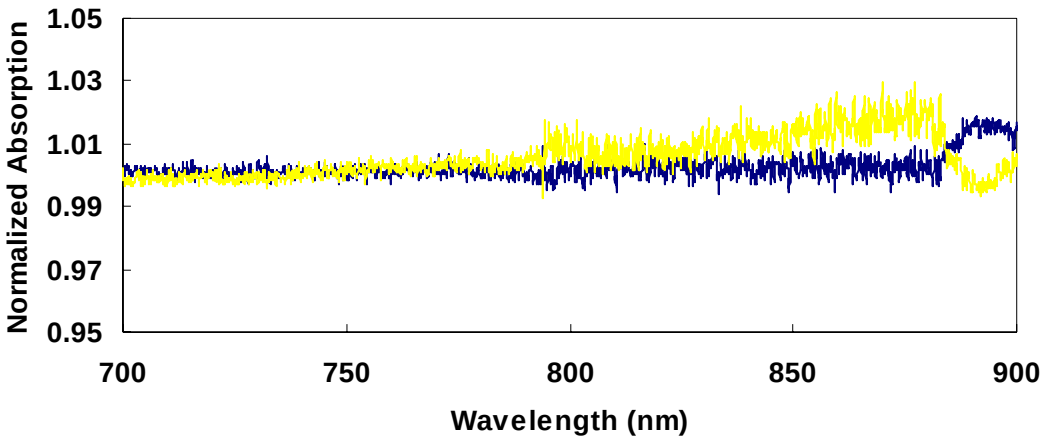

Figure 5.2 Normalized absorption spectra of tissue phantoms with (yellow curve) or without 170 μl DOX (blue curve) in the wavelength range of 700 ~ 900 nm.

calculating hemoglobin concentration. As shown in figure 5.2, profiles of normalized absorption spectrum in NIR range appeared to be overlaid.

5.3.2 Changes in Tumor volume and body weight during chemotherapy

Tumor volume and body weight were monitored before and after DOX treatment to examine the tumor response. Changes in tumor volume and body weight were normalized by the values at day 0 (before DOX administration).

Tumors in the control group grow significantly faster than tumors with treatment in the other groups ($p<0.05$), as shown in Figure 5.3a. Tumors with combined treatment of HBO and DOX grow significantly slower than those with DOX treatment except for the first two days after treatment ($p<0.05$). Basically, there is no significant difference for tumor volume in HBO + DOX and DOX groups on the 2nd day after treatment. However, significant differences are observed starting from 5th day after treatment between the DOX treated and control group ($p< 0.05$). Regarding body

weight loss, figure 5.3b indicated that rats in DOX group and DOX + HBO group had significant and continuous body weight loss after day 0. Rats in control group gained weight at day 2, and started to lose weight after day 4, and then kept constant body weight thereafter.

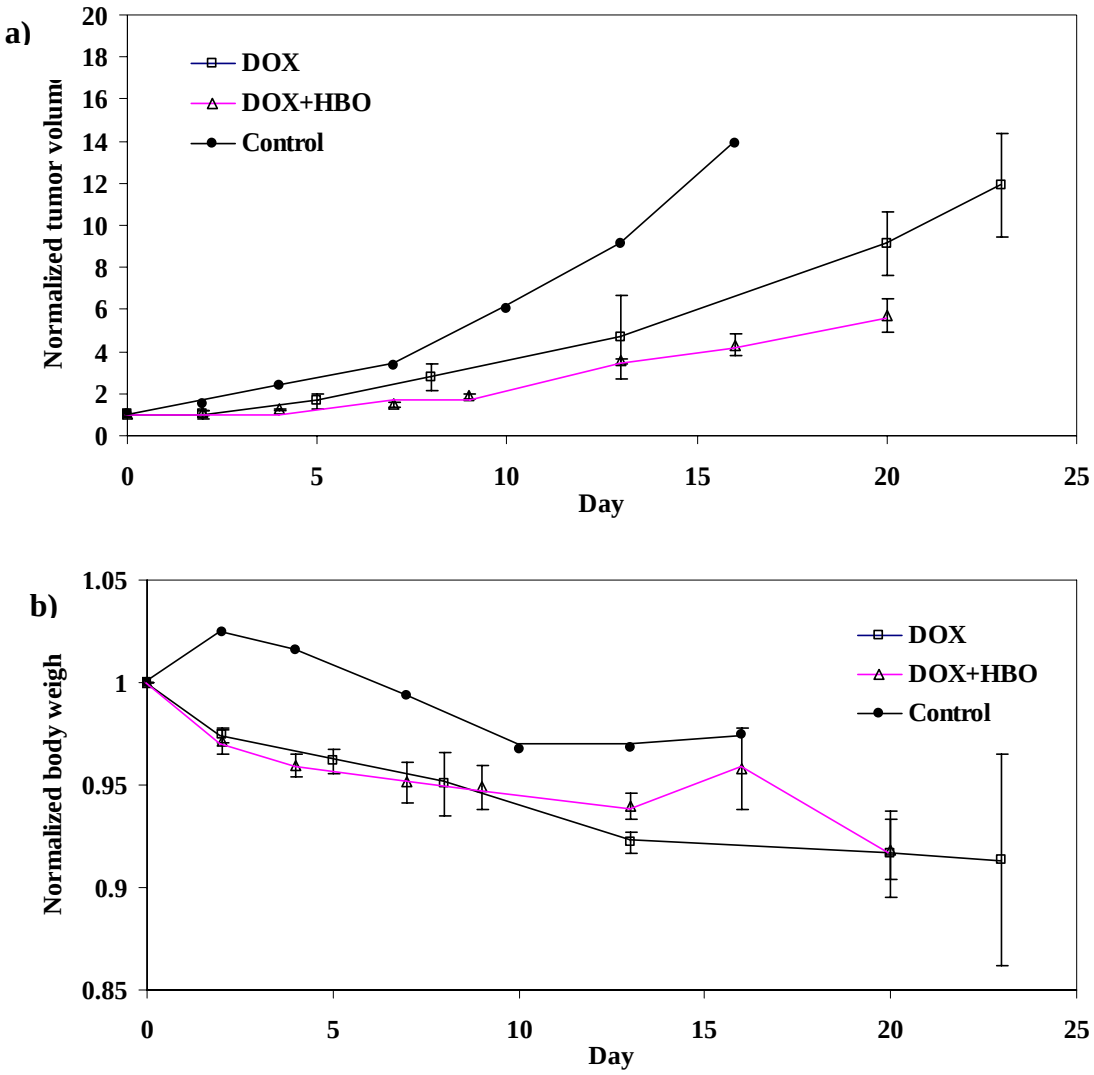

Figure 5.3 Normalized (a) tumor volume and b) body weight in rats with saline injection (●), DOX treatment (□) and HBO + DOX treatment (Δ).

5.3.3 Vascular hemodynamic changes of rats in DOX group

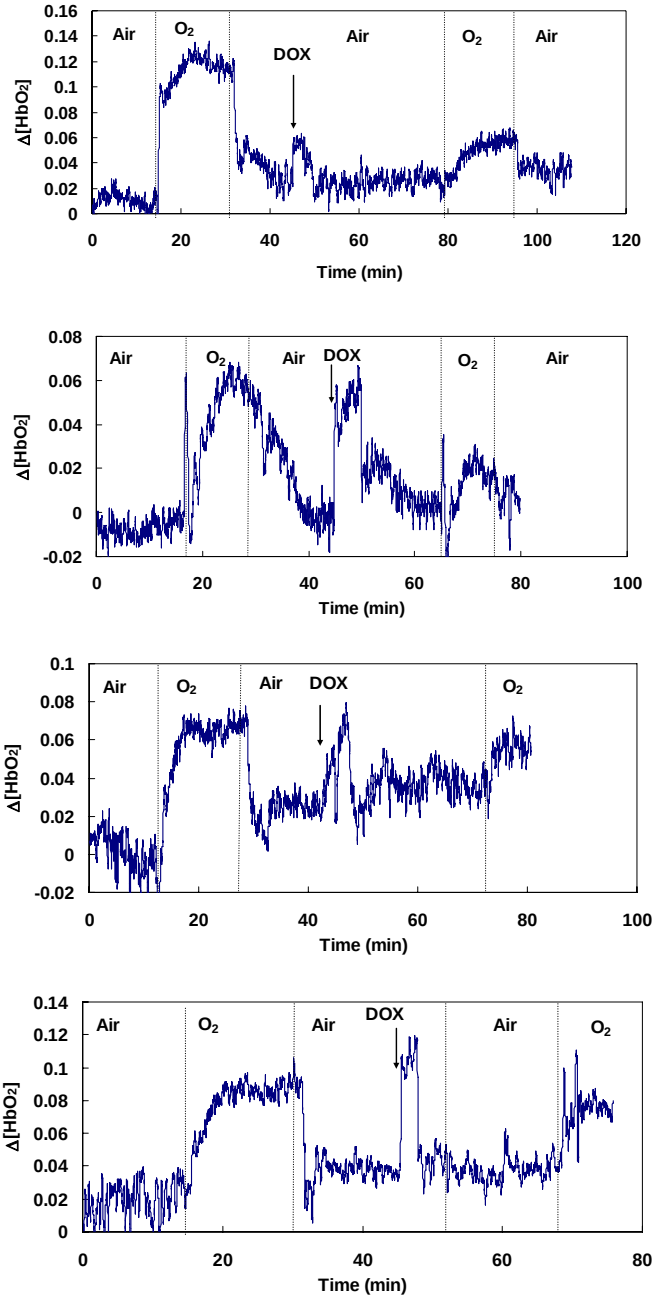

Figure 5.4 Time profile of $\Delta[HbO_2]$ of tumors (1~4) in DOX group when the rat was under gas intervention. The unit for $\Delta[HbO_2]$ is mM/DPF. $\Delta[HbO_2]$ of the 5th rat was discarded because of misplaced gas mask during the experiment due to the movement of the rat.

$\Delta[HbO_2]$ of rats in DOX group showed increases with values in a range of 0.07 ~ 0.12 (mM/DPF), when the gas switched from air to oxygen before DOX injection. When the gas was switched from air to oxygen after DOX administration, the maximal amplitude of $\Delta[HbO_2]$ increased with values in a range of 0.02 ~ 0.04 (mM/DPF), which is significantly less than the increase achieved with O_2 inhalation before DOX administration, as shown in figure 5.4. I also noticed the signal changes during DOX i.v. injection.

5.3.4 Vascular hemodynamic changes of rats in DOX +HBO group

It shows a stable baseline in $\Delta[HbO_2]$ when rats were inhaling air. $\Delta[HbO_2]$ increase immediately in the first few minutes and more gradually afterwards, as shown in figure 5.5. When the rats were exposed to hyperbaric oxygen, $\Delta[HbO_2]$ has a further increase until reaching a stabilized value. DOX i.v. injection immediately after HBO caused some fluctuation of signal, but stabilized when the injection is finished. $\Delta[HbO_2]$ has a stable baseline but with values greater than air inhalation before HBO when the rats were breathing air after HBO. Similar to DOX group, the maximal amplitude of $\Delta[HbO_2]$ achieved with O_2 inhalation prior to the DOX administration is significantly greater than that achieved with O_2 inhalation after DOX administration.

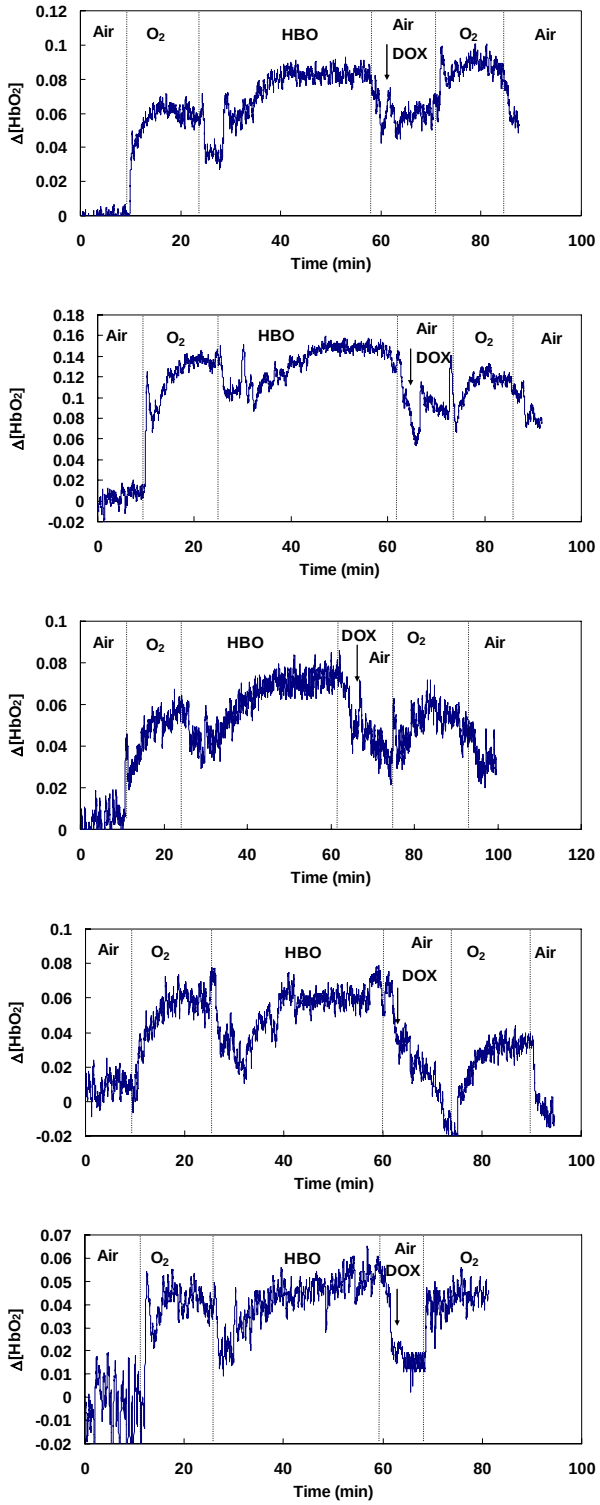

Figure 5.5 Typical time profile of $\Delta[HbO_2]$ of tumors in DOX + HBO group (n=5) when the rat was under gas intervention.

5.3.5 Vascular hemodynamic changes of rats in control group

$\Delta[HbO_2]$ have stable baseline values when rats were breathing air, as shown in figure 5.6. $\Delta[HbO_2]$ increased when the gas was switching to oxygen, and decreased when the gas was switched back to air, as expected. Different from $\Delta[HbO_2]$ in DOX treated group, the change of amplitude in $\Delta[HbO_2]$ when the gas switched from air to oxygen after saline injection is similar to the change due to gas intervention before injection in both rats.

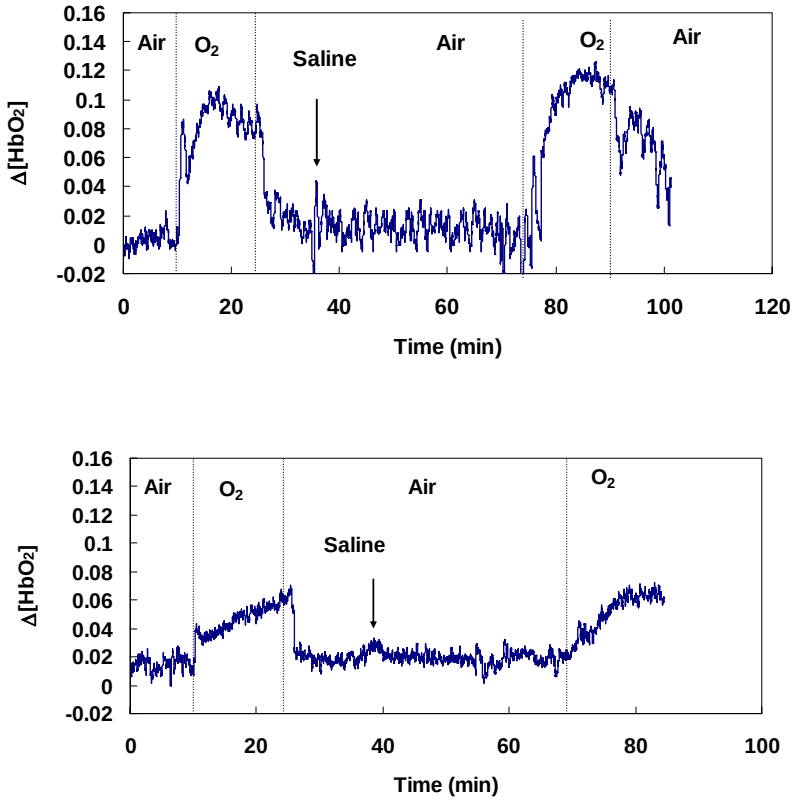

Figure 5.6 Time profile of $\Delta[HbO_2]$ of tumors in control group (n=2) when rats were subjected to gas intervention.

5.4 Discussion and Conclusion

In my study, I randomized breast tumors into three groups: group with DOX injection, group with DOX injection following HBO exposure at 2 atm, control group with saline injection. The result showed that tumors in HBO + DOX group grow significantly slower than those with DOX alone. HBO enhanced chemotherapeutic response of mammary carcinoma NF13762 to DOX *in vivo* reflected by slowing down the tumor growth after treatment.

Resistance to chemotherapy is common in hypoxic tumors. HBO may help overcome chemotherapy resistance by improving both tumor perfusion and cellular sensitivity. Improving tumor oxygenation and vascularization may increase drug delivery. This has been shown experimentally and in nude mice with human epithelial ovarian cancer treated with cisplatin [9, 129]. Reactive oxygen species (ROS), or free radicals are by-product of aerobic respiration and cellular metabolism and induced by oxidative stress during hypoxia (oxygen deficiency), reperfusion or hyperoxia (excess oxygen). ROS, at low levels, assist tumor growth but become toxic at high levels. This can be explained by the "threshold effect" whereby ROS reach a level beyond which the antioxidant capacity is inundated, resulting in irreversible damage and apoptosis [130-132]. One of the mechanisms of action of doxorubicin is production of ROS. By increasing ROS level, HBO push ROS levels past the threshold level, and thus enhanced the ROS-localized effects of doxorubicin [133, 134]. Another mechanism of HBO is to push cell to enter a proliferate stage, thus sensitizing them to radiotherapy and some chemotherapy by improving oxygenation. It has been showed that HBO

enhanced the chemotherapeutic effects of doxorubicin in an experimental model of pulmonary sarcoma [20]. HBO stimulated proliferation of an MCA-2 metastatic lung tumor cell line and induced cells to enter the replicating cycle compared to cells left at ambient pressure [20]. Other studies found that HBO increased the ratio of prostate cancer cells *in vitro* accumulating in G_2/M phases from the G_0 arrest phase [135]. Generally speaking, HBO therapy in combination with chemotherapy may be justified by the following: 1) improved oxygenation improves drug delivery to hypoxic regions in the tumor; 2) increasing intratumoral ROS levels beyond the threshold may induce tumor destruction; 3) improved oxygenation may also cause cell to enter a proliferate stage, thus sensitizing them to radiotherapy and some chemotherapy; 4) HBO may remove hypoxia stimulus that drives angiogenesis.

Even though the DOX dosage is reported to cause minimal cardiotoxicity, the result showed that changes in amplitudes of $\Delta[HbO_2]$ before DOX administration were much greater than the change after treatment in rats of DOX group and DOX + HBO group. It is likely that the amplitude difference results from the known cardiotoxicity reaction, the major side effect of DOX. It has been suggested that cardiac dysfunction induced by DOX resulted from the imbalances of the circulatory system such as decreases in blood pressure or the direct effects on vascular wall [136]. During the course of i.v. injection of DOX, the vasculature was exposed to high levels of DOX, and *in vitro* studies have suggested that DOX acutely induces vascular smooth muscle to release Ca^{2+} from its intracellular storage site and causes direct vasoconstrictor [137] and vasodilator effects [138]. Furthermore, the combination of doxorubicin and HBO

would also be expected to enhance the agent's cardiotoxicity because of the toxicity to cardiomyocytes of HBO. Therefore, the clinical addition of HBO to doxorubicin may not change the risk-benefit ratio of the agent. NIRS, in turn, may provide a novel approach to monitor the cardiotoxicity of treatment, which may leads to an optimized therapeutic plan to minimize the side effect of treatment. I also noticed the signal fluctuation in $\Delta[HbO_2]$ during DOX injection in DOX group. DOX solution is orange-red, so it is likely that DOX bolus injection would cause the absorption change of tumor tissue in NIR range. I measured and compared the spectra of tissue phantoms before and after adding DOX, to examine the disturbance of DOX injection on the signal of $\Delta[HbO_2]$. There were absorption differences when comparing both absorption spectra (Figure 5.1). However, the normalized spectra appeared to be overlaid (Figure 5.2). Therefore, it implied that DOX would affect total hemoglobin concentration, rather than oxygen saturation.

In summary, HBO enhanced the therapeutic action of doxorubicin in my tumor model, probably by multiple physiological mechanisms. The present study reveals that DOX may be used in conjunction with HBO to obtain the same effect as higher doxorubicin doses. Meanwhile, NIRS may work as an attractive approach to monitor the cardiotoxicity of treatment.

CHAPTER 6

NONINVASIVE MONITORING OF ESTROGEN EFFECTS AGAINST ISCHEMIC STROKE IN RATS BY NEAR INFRARED SPECTROSCOPY

6.1 Introduction

Stroke ranks as the third leading cause of death and the leading cause of disability in the United States [139]. There are two main types of stroke: ischemic stroke and hemorrhagic stroke, which account for about 83 percent and 17 percent of all cases, respectively. Ischemic stroke results from an obstruction of cerebral arteries, typically by blood clots. The blocking of the artery leads to acute reduction of perfusion pressure, which could induce dilation of arteries and veins on the surface of the brain [140]. Consequently, vasospasm occurs after cerebral ischemia [141]. Vasospasm is defined as inappropriate constriction or insufficient dilatation in the microcirculation and has been well described in the heart and brain. The recognition of vasospasm is essential both for the understanding and the treatment of heart attack and stroke.

In stroke, vasospasm has been extensively studied in subarachnoid hemorrhage (SAH), but to a less extent in ischemic stroke.[142, 143] Cerebral vasospasm has been proved to be the leading cause of death and disability after subarachnoid hemorrhage [144]. For ischemic stroke, some researchers also found arterioles near a vascular area frequently showed vasospastic appearance after 4-5 hours occlusion, which possibly caused prolonged hypo-perfusion even if reperfusion was achieved [143]. Therefore,

Anti-vasospasm drugs have become one of the major therapeutic targets for the treatment of both SAH and ischemic stroke. Accordingly, accurate evaluation of cerebral vascular hemodynamics in response to anti-vasospasm therapy should provide a better understanding of cerebral vasculature response to therapy, potentially allowing therapy to be tailored to individual characteristics.

Given the importance of cerebral hemodynamics, various techniques have been developed to observe vasospasm including xenon-enhanced computed tomography [145], corrosion cast technique [146], angiography [147] and Transcranial Doppler sonography [144, 148]. While each approach has unique strengths, some are highly invasive. In the last 15 years, Near Infrared Spectroscopy (NIRS) has been developed as a non-invasive optical method to measure cerebral hemodynamics, and it has been used to detect cerebral hypoxia and changes in cerebral blood volume [149-153]. Following the same principle, I hypothesized that NIRS can be utilized to detect cerebral vasospasm and monitor cerebral hemodynamic responses to anti-vasospasm therapy. This chapter reports my experimental investigation for my hypothesis based on animal studies.

Therapy targeting microvascular vasospasm is a promising approach to prevent myocardial infarctions [154]. Selective administration of a vasodilation drug, such as calcium antagonist, into vasospastic arteries in ischemic stroke would be effective in achieving a good clinical outcome [143]. It has been demonstrated that estrogens are potent neuro-protective agents and decrease focal and global ischemia-induced lesion size by as much as 50% and has been used to protect against reperfusion injury and

perhaps also to positively influence hemorrhagic risks by stabilizing energy metabolism in vascular endothelium [155-157]. Using the ovariectomized rats as a model, I investigated whether the acute estrogen depletion could induce microvascular dysfunction, such as vasospasm after ischemic stroke and that estrogen therapy could inhibit vasospasm in turn. An understanding of the events affected by estrogen during occlusion would allow us to define the therapeutic window for application of estrogens in stroke. In the present study, I explored, for the first time, the temporal effects of 17β-estradiol (E2) in focal cerebral ischemic event by NIRS. To characterize the rhythmic fluctuations of vasospasm during cerebral ischemia, I also performed the Fourier power spectral analysis of NIRS readings (hemoglobin concentration) in the control (without estrogen pretreatment) and the investigated (with estrogen pretreatment) stroke rat groups to validate my hypothesis, as reported in the following sections.

6.2 Materials and Methods

6.2.1 Animal preparation

Female Sprague-Dawley rats (250g; Charles River, Wilmington, MA) were acclimatized for 3 days before surgery. Two weeks before the focal ischemia was induced, all rats were bilaterally ovariectomized to eliminate endogenous estrogens. There were two groups of rats used in the experiments: ovariectomized rats alone (OVX; n=5) and ovariectomized rats with estrogen pretreatment (OVX+E2; n=4). One rat in OVX + E2 group has died during surgery. OVX group received focal ischemia surgery only, while OVX+E2 group was administrated a single dose of 17β-estradiol dissolved in corn oil (100 μg/kg) 2 hours before focal ischemia surgery. The rat hair

was trimmed for the ease of optical fiber contact before the surgery of middle cerebral artery occlusion (MCAO). All animal procedures were approved by the University of North Texas Health Science Center Animal Care and Use Committee.

6.2.2 Ischemic stroke model and experimental setup

Ischemic stroke was induced by MCAO as described elsewhere [158]. Briefly, rats were anesthetized with ketamine (60 mg/kg) and xylazine (10 mg/kg) by intraperitoneal injection. The left femoral artery was canalized and connected to a blood pressure monitor for mean arterial blood pressure monitoring. The left middle cerebral

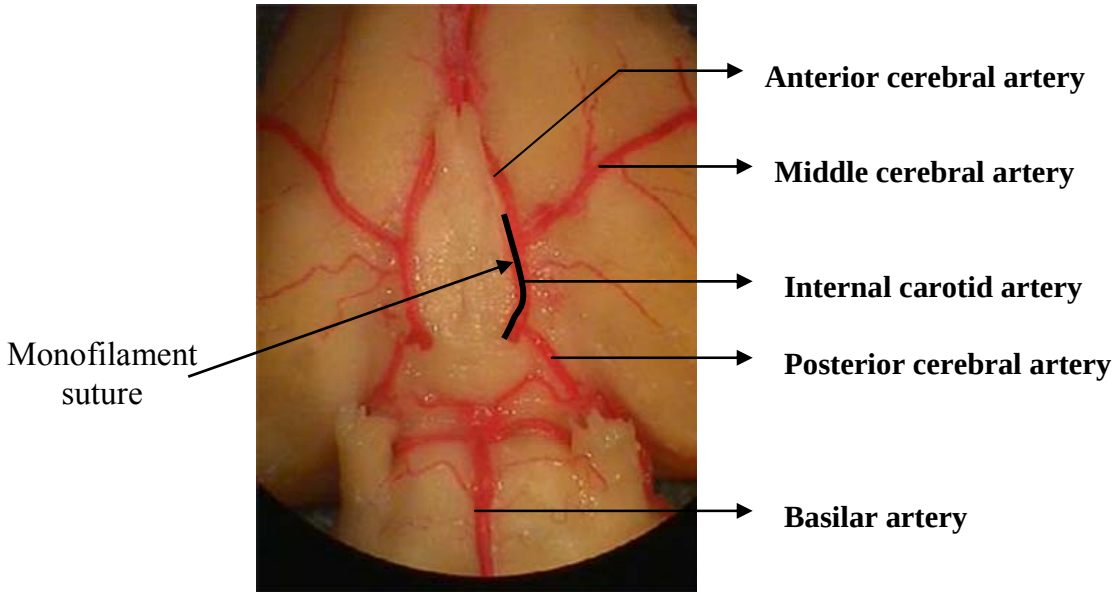

Figure 6.1 Demonstration of the location of a monofilament suture that was placed through one internal carotid artery to create middle cerebral artery occlusion.

artery (MCA) was occluded by a 3-0 monofilament suture introduced via the internal carotid artery, as shown in figure 6.1.

During surgery, the rat was placed in a small animal surgical platform and its body temperature was monitored, by a rectal probe, and maintained at between 36.5 and 37^{o}C with a heating lamp. Once the surgery of MCAO was complete, the rat was transferred immediately to another platform with a surgical frame to hold the animal head for the NIRS monitoring. The NIR light source was positioned firmly but with minimal pressure on the center of the animal head. There were two detectors, one was placed on the top of the ischemic hemisphere (the investigated side), and the other was on the non-ischemic hemisphere (the control side). NIRS system started to record hemodynamic data as soon as the NIRS probes were positioned on rat head. Therefore, there was a few minutes lapsed before NIRS system start recording data after occlusion. One hour after MCAO, the suture was withdrawn smoothly for reperfusion without perturbing the NIRS setup, and the NIRS system was continued to record the data.

6.2.3 Near infrared spectroscopy monitoring

A multi-channel, continuous wave NIRS system was used to monitor vascular oxygenation dynamics. Briefly, the light source of NIR system, emitting light at 750 nm, 805 nm and 830 nm sequentially, illuminated the rat head on the center of the head. The transmitted light was detected by two photo detectors. The NIR signals were amplified and digitized by an Analog-to-Digital Converter (ADC), followed by real-time display and data recording in a laptop computer.

According to the modified Beer-Lambert law, concentration changes in oxygenated and deoxygenated hemoglobin, $\Delta[HbO_2]$ and $\Delta[Hb]$, can be derived from the measured amplitudes transmitted at the two wavelengths (750nm and 830nm)[18]:

$$\Delta[HbO_2] = \frac{-1.532 \log(\frac{A_b}{A_t})^{750} + 1.753 \log(\frac{A_b}{A_t})^{830}}{DPF \cdot d} \quad (6.1)$$

$$\Delta[Hb] = \frac{1.758 \log(\frac{A_b}{A_t})^{750} - 0.92 \log(\frac{A_b}{A_t})^{830}}{DPF \cdot d} \quad (6.2)$$

where A_b and A_t are the NIR amplitudes during the occlusion and reperfusion periods, respectively, d is the direct source-detector separation, and *DPF* (differential path-length factor) is a tissue-dependent parameter and defined as the ratio between the optical path length and the physical separation between the source and detector. *DPF* is a variable, depending on tissue types and wavelengths, and typical values of *DPF* range from 3.59 ± 0.32 in the adult arm to 5.93 ± 0.42 in the adult brain [159]. However, a typical *DPF* value for a rat brain is unknown due to its limited size. In the study, since I are more interested in hemo-dynamic changes in the rat brain during ischemic stroke and reperfusion, *DPF* was included in the unit of [HbO_2] and [Hb], which still allow features of cerebral oxygen dynamics to be characterized. After Δ[HbO_2] and Δ[Hb] are calculated, Δ[HbT] is the summation of Δ[HbO_2] and Δ[Hb].

6.2.4 Fourier Analysis

The values of Δ[HbO_2], Δ[Hb], and Δ[HbT] during the entire experimental periods were calculated using equations (6.1) and (6.2). The fluctuation frequencies contained in the Δ[HbO_2] profiles were obtained by Fourier power spectral analysis using Matlab software (the mathworks, Inc, Natick, MA). The frequency analysis

covered the temporal period from 10 to 59 min after the MCAO, i.e., during the course of the ischemic stroke right before reperfusion. The sampling rate of multi-channel NIRS was 1 Hz, so it was much higher than the fluctuation frequencies in $\Delta[HbO_2]$. Thus, the frequency characteristics of the instrumentation had no impact on the Fourier analysis.

One way to view and compare the power spectral analysis is to examine the frequencies at which the power peaks are located. This technique was recently used to compare power spectra of blood flow in the optic nerve head [160]. The Fourier power spectra represent the magnitudes and frequencies of hemodynamic fluctuations during MCAO and reperfusion and inspect the total power over a given frequency range. Since $\Delta[HbO_2]$ signals are only relative changes, I normalized the power spectra by the value at 0 Hz. Because of the difference in peak powers between the two animal groups (OVX versus OVX+E2), the range chosen for power spectral analysis was 0.0025~0.01 Hz. The total power of $\Delta[HbO_2]$ frequency spectrum was quantified by integrating all the powers within a specific frequency range of 0.0025-0.01 Hz. The total cumulative powers were compared between two groups, and the Student t-test was used to determine a significant decrease in fluctuation power in OVX+E2 group, compared with OVX group.

6.3 Results

6.3.1 Dynamic response of hemoglobin concentration measured by NIRS

I observed rhythmic fluctuations in $\Delta[HbO_2]$ and $\Delta[HbT]$ when the rats were under occlusions, as shown in Figure 6.2a, a temporal profile of $\Delta[HbO_2]$ and $\Delta[HbT]$

of cerebral ischemic side in one representative rat of OVX group. However, there is no fluctuation observed in $\Delta[HbO_2]$ and $\Delta[HbT]$ in non-ischemic side of the same rat (Figure 6.2b). Figure 6.3 presents the temporal profiles of $\Delta[HbO_2]$ and $\Delta[HbT]$ in cerebral ischemic side of one representative rat in OVX+E2 group. No fluctuations were observed in both profiles of $\Delta[HbO_2]$ and $\Delta[HbT]$ in the ischemic side of rats in OVX + E2 group (Figure 6.3), neither in the corresponding control side.

$\Delta[HbO_2]$ of the ischemic side shows slight decrease when OVX rats were under occlusion. In contrast, I observed a slight increase in $\Delta[HbO_2]$ of the ischemic side when OVX + E2 rats were under occlusion. $\Delta[HbO_2]$ of the ischemic side in both groups of rats increased immediately once the reperfusion started. The value of $\Delta[HbO_2]$ was recorded at multiple time points (10, 30, 60, 70, 90 min), averaged over rats in OVX group (n=5) and OVX + E2 group (n=4) respectively, and normalized at the time (=60 min) when the reperfusion occurred for the ease of comparison, as shown in figure 6.4.

As I expected, $\Delta[HbT]$ in the ischemic side of both groups showed a gradual decrease in response to occlusion. Immediately after reperfusion, $\Delta[HbT]$ of both ischemic and non-ischemic side in OVX group decrease in the first few minute after reperfusion and generally recovered afterwards (Figure 6.2a and 6.2b). In comparison, I observed an immediate increase of $\Delta[HbT]$ of ischemic side in OVX + E2 group in the fist few minutes and then more gradual increase thereafter, as shown in figure 6.3.

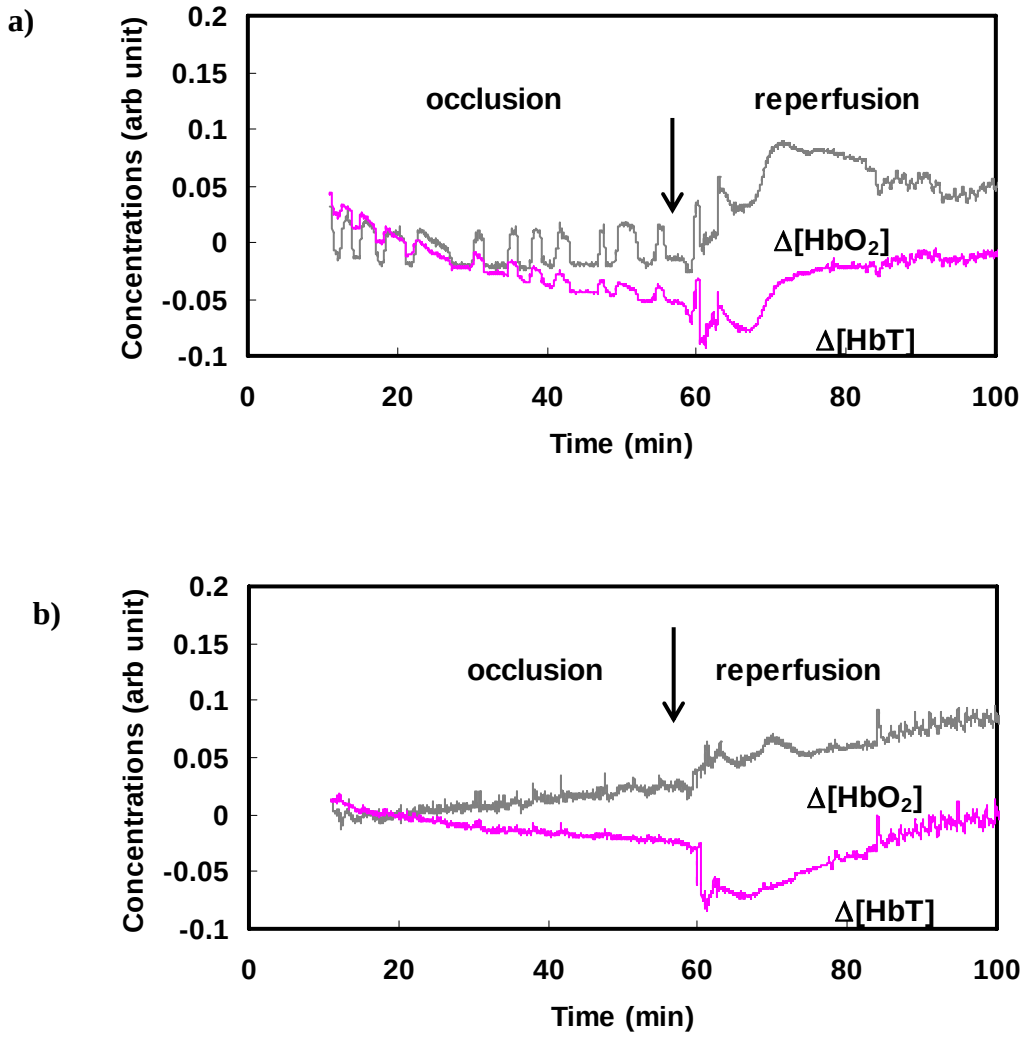

Figure 6.2 Temporal profiles of $\Delta[HbO_2]$ (black curve) and $\Delta[HbT]$ (pink curve) measured on (a) the ischemic side and (b) non-ischemic side of the rat during MCA occlusion and reperfusion from a representative rat in OVX group.

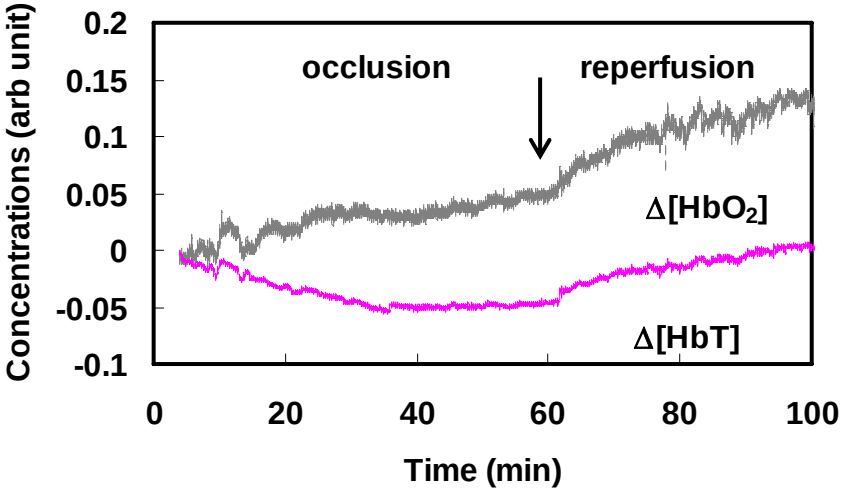

Figure 6.3 Temporal profiles of $\Delta[HbO_2]$ (black curve), and $\Delta[HbT]$ (pink curve) measured on the ischemic hemisphere during ischemia and reperfusion from a representative rat in OVX + E2 group.

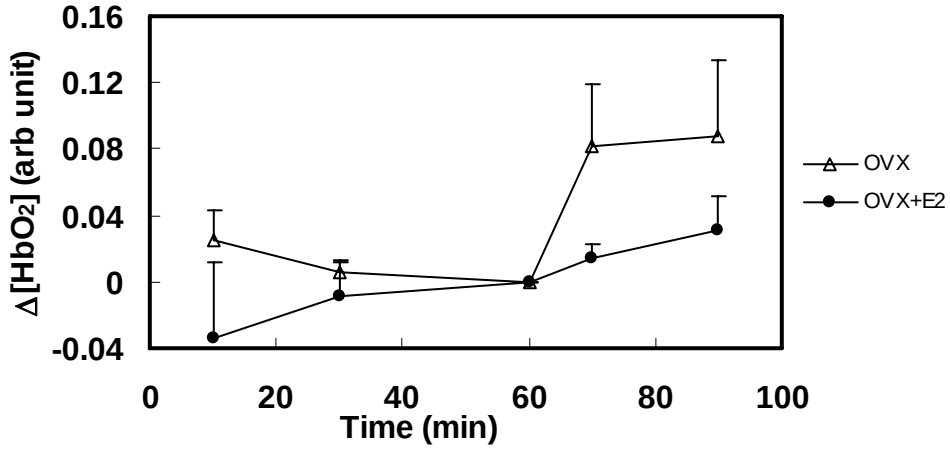

Figure 6.4 $\Delta[HbO_2]$ at multiple time points (10 min, 30min, 60min, 70min, 90min), averaged over OVX (n=5) and OVX+E2 (n=4) groups respectively, and normalized at 60 min for the ease of comparison between two groups. Every data point is presented as mean ± SD. MCA occlusion starts at time of 0 min, while the reperfusion is introduced at time of 60 min.

6.3.2 Fourier analysis of hemoglobin concentration fluctuations

To examine the fluctuation displayed in $\Delta[HbO_2]$ of the ischemic side of the stroke rat head, I computed $\Delta[HbO_2]$ power spectra, or periodograms, during the period of MCAO from both ischemic and control sides of OVX group rats. Figure 6.5 shows an example of $\Delta[HbO_2]$ periodogram from the representative rat of OVX group. It is observed from figure 6.5(a) that multiple power peaks occur in the frequency range between 0.0025 and 0.01 Hz from the data taken on the ischemic side, while no significant peaks in the corresponding frequency range taken from the control side (Figure 6.5b).

In order to examine the effects of estrogen pretreatment on the occluded cerebral vasculature of OVX rats, similar frequency analysis was also performed on $\Delta[HbO_2]$ and $\Delta[HbT]$ of both OVX and OVX + E2 groups. By calculating total cumulative powers between 0.0025 and 0.01 Hz based on the $\Delta[HbO_2]$ temporal profiles from all the rats, I found that the total mean power in OVX+E_2 group is significantly lower than that in OVX group ($p<0.05$), as shown in Figure 6.6. However, the total cumulative power of $\Delta[HbT]$ in OVX+E2 group is less, but not statistically less than that from OVX group ($p>0.05$).

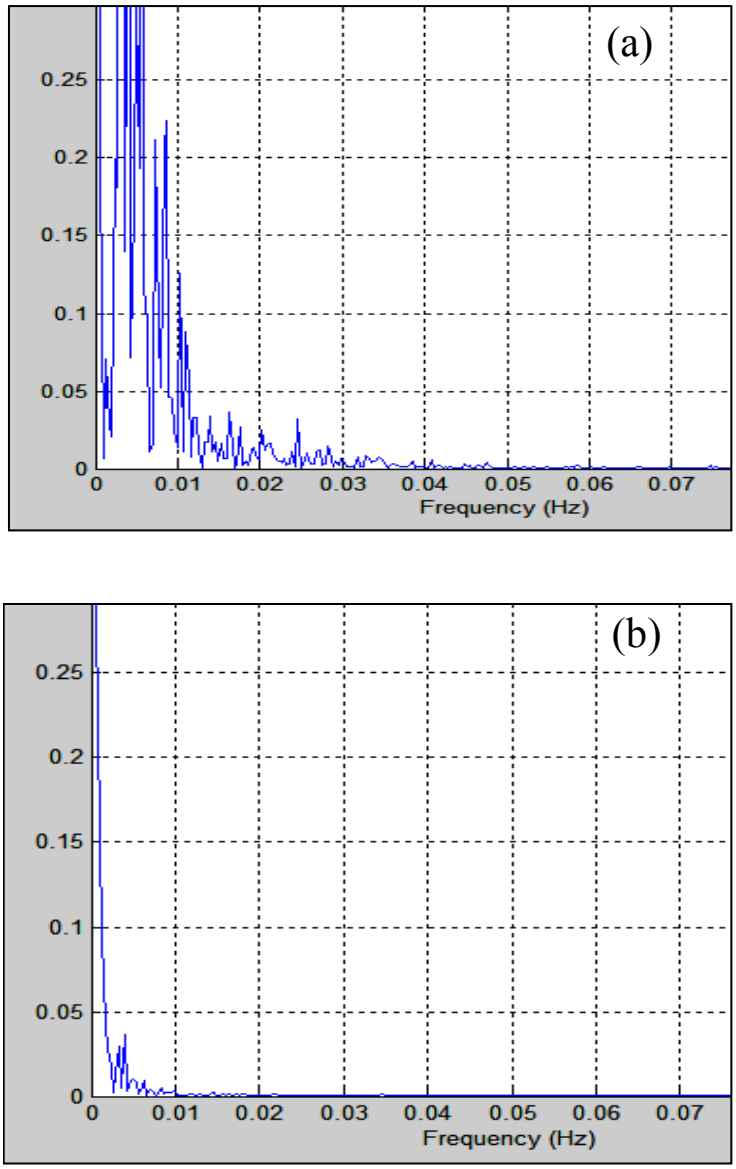

Figure 6.5. Corresponding periodograms calculated from the $\Delta[HbO_2]$ profiles (as given in figure 6.2) on the (a) ischemic side and (b) non-ischemic side. A significant total power increase in the frequency range between 0.0025 to 0.01 Hz was observed in the ischemic side compared to the non-ischemic side.

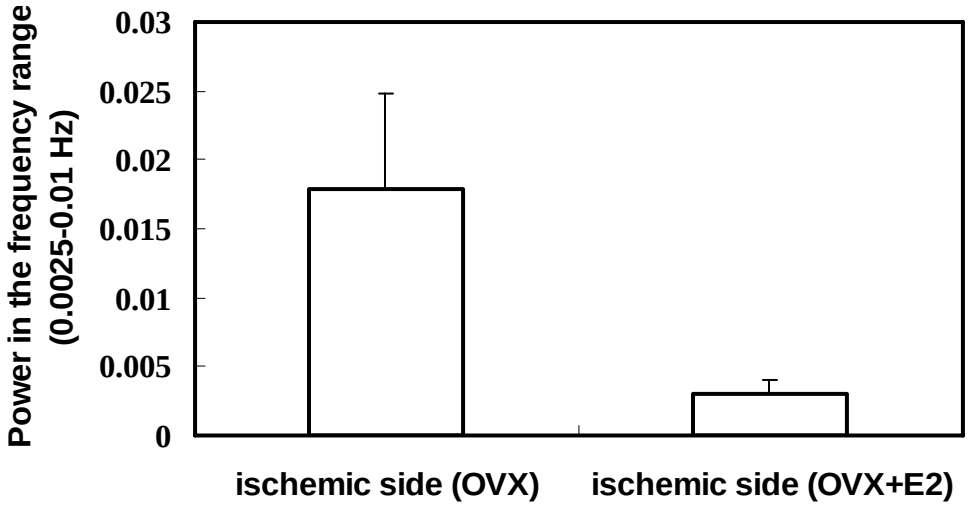

Figure 6.6 Power spectral analysis of $\Delta[HbO_2]$ profiles, taken during the ischemic stroke. It shows a significant decrease ($p<0.05$) in total power within the frequency range of 0.0025-0.01 Hz in OVX + E2 group (n=4), compared with the OVX group (n=5).

6.4 Discussion and conclusion

This study adopts NIRS in the reflection mode (optodes placed on the same side of the head close to each other). Despite unresolved spatial and quantitative concerns surrounding NIRS, relative changes in the concentrations of chromophores still could provide a useful clinical index [161]. Our own experiences show that NIRS provides a sensitive indicator to detect changes in the tissue vascular oxygenation state and hemodynamics of the brain in response to therapeutic intervention and therapy [124, 162]. In the present study, the main question addressed are whether changes in the concentration of hemoglobin can be used as an indicator as the cerebral vascular function during MCAO and thus to be used to monitor the therapeutic effect of vasodilation agent to treat cerebral vascular dysfunctions.

I monitored the temporal changes of cerebral vascular hemoglobin concentration ($\Delta[HbO_2]$ and $\Delta[Hb]$) in response to temporary middle cerebral artery occlusion in ovariectomized rats, when the rats had no pretreatment (Figure 6.2) or estrogen pretreatment (Figure 6.3). I observed the slow rhythmic variations with frequencies in $\Delta[HbO_2]$ and $\Delta[HbT]$ of OVX rats in response to occlusion. The Fourier analysis indicated that the rhythmic variation rest principally in the frequency range 0.0025 - 0.01 Hz. In comparison, there are no such variations in $\Delta[HbO_2]$ and $\Delta[HbT]$ of the corresponding control side without occlusion. One reason for the signal fluctuation might be aliasing of heart or respiratory motion. It has been postulated, however, that the sampling rate of 1 Hz should exclude cardiac (5 Hz) and respiratory motion aliasing (2 Hz) in activation studies [163]. Low frequency hemodynamic oscillation may reveal autoregulatory mechanisms of the brain vasculature [164-166]. However, the rhythmic fluctuation in the present study is more than 10 times slower than the signals caused by regular cerebral vasomotion, which contains a range of frequencies characteristically peaking around 0.1Hz and not a peculiarity of species and anesthetic state [163]. Similar fluctuations slower than regular vasomotion were also observed in MR signals of children who were undergoing routine clinical MRI under thiopental anesthesia [167]. It was postulated that such fluctuations occurred during the absence of autoregulation [167, 168]. Therefore, the rhythmic fluctuations are likely to indicate cerebral vasospasm, a microvascular dysfunction induced by vascular ischemia during MCAO.

Cerebral autoregualtion is thought to result from intrinsic myogenic and metabolic factors but is also known to be modified by extrinsic factors such as hormone conditions [169]. Estrogen, as a potent neuro-protective compound in a variety of animal and cell culture models, play important roles in the autoregulatory mechanisms of the cerebral vasculature [158, 170]. Loss of estrogen in ovariectomized rats can affect the normal cerebral autoregulation, thus it is likely to have abnormal vascular responses, such as cerebral vasospasm, to happen when cerebral vascular pressure changes abruptly due to occlusion, as shown in figure 2a. Selective administration of a vasodilation drug into vasoplastic arteries in ischemic stroke would be an effective way to achieve a good clinical outcome. In the current animal model with estrogen pretreatment, there is no vasospasm occurred during occlusion in OVX + E2 rats, as shown in Figure 6.3. Furthermore, the temporal profiles of $\Delta[HbO_2]$ and $\Delta[HbT]$ during occlusion were analyzed by Fourier spectrum to characterize the estrogen effects on ischemic cerebral vasculatures. The corresponding spectra were compared between the OVX rats and OVX + E2 rats. The frequency analysis of $\Delta[HbO_2]$ indicated a significant decrease in fluctuation within the frequency range between 0.0025 to 0.01 Hz in OVX + E2 rats in comparison with the OVX rats ((Figure 6.5). Therefore, I could postulate that 17β-estradiol partially restore the vessel function to similar levels as non-ischemic vessels. Some recent studies also demonstrated the similar therapeutic effects of 17β-estradiol on the vessel function [171]. Certainly, a better understanding of the mechanisms underlying the beneficial effects of estrogen on the vasculature is required to optimize possible therapeutic application. By using the ischemic stroke rat model in

conjunction with estrogen pretreatment, this study has provided strong experimental support for my hypothesis that NIRS can be utilized to detect cerebral vasospasm and to monitor cerebral hemodynamic responses to anti-vasospasm therapy.

Estrogen has been also shown to be a vasorelaxant [172]. During Occlusion, there is a gradual decrease in Δ[HbT] in both ischemic side and non-ischemica side of two groups, which indicates the decrease of the total blood volume due to the occlusion. Meanwhile, $\Delta[HbO_2]$ shows a slight decrease in the ischemic side of OVX group, which implies the depletion of oxygen molecule binding with hemoglobin due to the occlusion. In contrast, $\Delta[HbO_2]$ have a slight increase in the ischemic side of OVX + E2 group in response to occlusion. Both $\Delta[HbO_2]$ and Δ[HbT] temporal profiles in ischemic side of OVX + E2 group have similar trends as those in non-ischemic side of OVX group in response to occlusion and reperfusion, which may indicate Estrogen reduces the risk of cerebral ischemia/reperfusion injury by its vasoactive effects. It has been demonstrated that estrogen enhance cerebral blood flow during global ischemia and early reperfusion in an ischemia/reperfusion model [172, 173].

In summary, this study demonstrates that NIRS detects the cerebral hemodynamic changes in response to middle cerebral artery occlusion and after reperfusion in ovariectomized rats. A significant component of signal fluctuation in a low-frequency range was identified in $\Delta[HbO_2]$ temporal profiles from the ovariectomized rats without estrogen pretreatment. Comparatively, those fluctuations disappeared in those rats with the pretreatment. While the underlying mechanism of estrogen therapeutic effects on microvascular dysfunction requires further investigation,

the present study clearly demonstrates a new application of NIRS, i.e., to detect cerebral vasospasm and to monitor cerebral responses to anti-vasospasm therapy. The methodology may become a useful monitoring tool in animal studies for pharmaceutical development to treat dysfunctional microvasculature and vasospasm induced by cerebral ischemia.

Acknowledgements

This study was supported in part by the research seed funding from the University of Texas at Arlington and the University of North Texas Health Science Center at Fort Worth.

CHAPTER 7

SUMMARY AND FUTURE WORK

7.1 Summary

The objectives of the study are to 1) validate NIRS measurement by other approaches including MRI and FOXY^{TM} fluorescence oxygen sensor; 2) examine the preservation of tumor oxygenation after the administration of hyperbaric oxygen; 3) investigate whether HBO, when combined with DOX, can produce better therapeutic efficiency than DOX alone. 4) demonstrate NIRS is an attractive tool to monitor tumor vasculature response to therapeutic intervention or cerebral vascular oxygen dynamics during and after stroke.

To accomplish the goals, 1) ^{19}F MRI was applied to monitor tumor tissue oxygen tension (pO_2) images, while NIRS was used to measure global tumor vascular oxygenation dynamics simultaneously when the rats were exposed to hyperoxic gas intervention. Multiple correlations were examined between the rate and magnitudes of vascular and tissue oxygen response. 2) two techniques, FOXY fluorescence oxygen sensor and NIRS, were applied simultaneously to monitor tumor tissue and vascular oxygenation during and post hyperbaric oxygen administration. 3) Tumor size and body weight were monitored and compared between rats treated with combined therapy and chemotherapy alone. 4) multi-channel NIRS was used to monitor the cerebral vascular

oxygenation during and after MCAO, and characterize the therapeutic effects of estrogen on dysfunctional vasculature induced by MCAO.

The present study demonstrated that 1) NIRS and MRI and FOXY^{TM} oxygen sensor are complimentary approaches to monitor tumor oxygenation. 2) Tumor tissue oxygenation achieved by hyperbaric oxygenation persists over 10-20 minutes even after terminating hyperbaric oxygenation intervention. 3) Several correlations were existed for both modalities under sequences of hyperoxic gas intervention with hyperbaric oxygen exposure. Correlation of tumor vascular oxygenation and tumor tissue pO_2 determined by those techniques simultaneously could give us a better understanding on the patho-physiology of tumor and response to therapeutic interventions. 4) HBO enhanced the therapeutic action of doxorubicin in my tumor model, probably by multiple physiological mechanisms. DOX could be used in conjunction with HBO to achieve the same effect as higher doxorubicin doses. NIRS may work as an attractive approach to monitor the cardiotoxicity of treatment. 5) NIRS can detect cerebral vasospasm and monitor cerebral responses to anti-vasospasm therapy. The methodology presented in the dissertation may become a useful monitoring tool in animal studies for pharmaceutical development to treat dysfunctional microvasculature and vasospasm induced by cerebral ischemia.

7.2 Future Work

As mentioned in chapter 3, ΔTBF and $\Delta TMRO_2$ were calculated from NIRS readings based on the model. The current results revealed all three possibilities, i.e., increase, no change or decrease of blood flow, during carbogen inhalation. Such

variations may be due to tumor- or site-specific differences in the vasculature. Moreover, the estimated $\Delta TMRO_2$ reveals the similar trend as the ΔTBF during hyperoxic gas intervention. All of these results, nevertheless, need to be further verified by simultaneous PET/NIRS or Laser Doppler Imager/NIRS measurements in tumors.

As described in chapter 2 and 4, I monitored the tumor vascular and tissue oxygen dynamics in response to therapeutic interventions (normobaric oxygen or hyperbaric oxygen) by simultaneous NIRS/MRI or NIRS/FOXY measurement. Given the tumor heterogeneity, NIR imaging system could be introduced to the future study since it could provide images of changes in vascular oxygenation and blood volume in response to therapeutic interventions.

The present study showed that combined therapy of DOX with HBO produced better therapeutic effect than DOX alone, by comparing the tumor growth rate of tumors in DOX + HBO group with those in DOX groups. Apart from the overall tumor volume, other parameters, such as tumor distribution and occurrence of distal metastases, could be monitored in the future study. In addition, the DOX dosage in the present study needs to be reconsidered since it only cause the tumor regression tumor rather than the tumor remission. Despite DOX is one of the most widely used broad-spectrum anticancer agents, the cardio-toxicity DOX limits its application. Back to 80s, variety of drug delivery methods has been applied to doxorubicin, in order to increase therapeutic efficacy and decrease toxicity of the agent. Magnetically responsive albumin microspheres containing doxorubicin and magnetite (Fe_3O_4) were selectively targeted to Yoshida sarcoma tumors in rats by utilizing an extracorporeal magnet [174]. Their

results indicated that all the rats treated with microspheres containing DOX exhibited total remission and no death or metastases occurred, while the control group data has significant increase of tumor size and widespread metastases. Moreover, liposome-encapsulated doxorubicin has been reported to provides ~30% increase in life span in an intracranial rat brain tumor model compared with free DOX [175]. Therefore, doxorubicin encapsulated in magnetic microsphere or remote-loaded, sterically stabilized liposomes, could be administrated to rats immediately following HBO intervention in the future study. In addition, the distribution of DOX inside the tumor body can be traced by fluorescence imager because of the autofluorescence feature of DOX.

In chapter 6, NIRS was utilized to monitor the vasospasm induced by MACO in ovariectomized rats. In the future study, simultaneous measurement by NIR imaging system and flowmeter could be introduced to provide more information for localized cerebral vascular oxygenation and blood flow rate, so as to assist us to find a better therapeutic treatment.

APPENDIX A

LIST OF PUBLICATIONS

Publications in peer-reviewed journals:

1. **Mengna Xia**, Vikram Kodibagkar, Hanli Liu and Ralph Mason, "Tumor oxygen dynamic measured simultaneously by near infrared spectroscopy and ^{19}F magnetic resonance imaging in rats", Physics in Medicine and Biology,51: 45-60(2006) .

Up to April 20, 2007, the paper has been cited by:

CH-overtone regions as diagnostic markers for near-infrared spectroscopic diagnosis of primary cancers in human pancreas and colorectal tissue

Michael Keese, Ralf Mueller, H. Michael Heise, Venkata Radhakrishna Kondepati, Thomas Oszinda, Klaus Luig, Olaf Schroeder and Juergen Backhaus 2007 *Analytical and Bioanalytical Chemistry*

MR assessment of changes of tumor in response to hyperbaric oxygen treatment

Murali C. Krishna, Peter Choyke, Marcelino Bernardo, Ken-ichiro Matsumoto, Sankaran Subramanian, James B. Mitchell and Martin J. Lizak 2006 *Magnetic Resonance in Medicine*

2. Jae Kim**, Mengna Xia,** Hanli Liu, **"**Extinction coefficients of hemoglobin for near-infrared spectroscopy of tissue", IEEE Engineering in Medicine and Biology magazine, 24: 118-121 (2005)

3. Yueqing Gu, Wei R. Chen, **Mengna Xia**, Sang W. Jeong, and Hanli Liu, "Effect Of photothermal therapy On breast tumor vascular contents: non-invasive monitoring by near infrared spectroscopy", Photochemistry and Photobiology, 81: 1002-1009 (2005)

roceeding papers and presentations:

1. **Mengna Xia,** Benjamin Levine, Ralph Mason, Hanli Liu, "Simultaneous monitoring of tumor vascular oxygenation and tissue oxygen tension under hyperbaric oxygen exposure", in Biomedical Topical Meetings on CD-ROM (The Optical Society of America, Washington, DC, 2006).
2. **Mengna Xia**, Vikram Kodibagkar, Ralph Mason, Benjamin Levine, Hanli Liu, "Tumor vascular and tissue oxygenation dynamics under normobaric and hyperbaric oxygen interventions", presented at the fourth Era of Hope meeting for the Department of Defense (DOD) Breast Cancer Research Program (BCRP) held on June 8-11, 2005 in Philadelphia, Pennsylvania
3. Xiufeng Li, **Mengna Xia**, Edmond Richer, Matthew Lewis, Billy Smith, Ammar Adam, Ralph Mason, Hanli Liu, Peter P. Antich, "Optical Imaging Phantom Study for Quantitative Imaging Correction and Physiological Parameter Detection in vivo, Molecular Medicine Symposium", presented in the University of Texas System: Translating Discoveries into Health, Houston, TX, 2005
4. **Mengna Xia**, Ralph Mason, Hanli Liu, "A model of hemodynamic responses of rat tumors to hyperoxic gas challenge", Proc. SPIE- Optical Tomography and Spectroscopy of Tissue VI, 5693: 301-307 (2005)

5. **Mengna Xia**, Vikram Kodibagkar, A. Constantinescu, Y. Gu, H. Liu, R. P. Mason, "Simultaneous ^{19}F MR EPI imaging and near-infrared spectroscopy to establish correlations in tumor oxygen dynamics", 12^{th} annual meeting of the international society of magnetic resonance in Medicine, Kyoto, 2004.

6. Yueqing Gu, Vikram Kodibagkar, **Mengna Xia**, Anca Constantinescu, Ralph P. Mason, Hanli Liu, "Breast tumor vascular oxygenation and blood volume assessed by near-infrared spectroscopy and magnetic resonance", Proc. SPIE- Optics in Health Care and Biomedical Optics: Diagnostics and Treatment II, 5630: 918-925 (2004)

7. **Mengna Xia**, Vikram Kodibagkar, Yueqing Gu, Anca Constantinescu, Ralph Mason, Hanli Liu, "Tumor oxygen dynamics measured simultaneously by near infrared spectroscopy and ^{19}F MR EPI imaging", in Biomedical Topical Meetings on CD-ROM (The Optical Society of America, Washington, DC, 2004), ThF33

8. Yueqing Gu, Vikram Kodibagkar, **Mengna Xia**, Anca Constantinescu, Ralph Mason, Hanli Liu, "Correlation of NIR spectroscopy with BOLD MR imaging of assessing breast tumor vascular oxygen status", in Biomedical Topical Meetings on CD-ROM (The Optical Society of America, Washington, DC, 2004), FB6

9. Yueqing Gu, Vikram Kodibagkar, **Mengna Xia**, Zhiyu Qian, Jae. G. Kim, Anca Constantinescu, Ralph P. Mason, Hanli Liu, "Simultaneous determination of breast tumor vascular oxygenation and blood volume measured with near infrared spectroscopy and ^{19}F MRS and ^{1}H MRI," presented in SPIE, Photonics West, San Jose, CA, Jan. 26-29, 2003.

10. Yueqing Gu, Vincent Bourke, Jae G. Kim, **Mengna Xia,** Anca Consstantinescu, Ralph P. Mason, Hanli Liu, " Breast tumor oxygenation in response to carbogen intervention assessed

simultaneously by three oxygen-sensitive parameters", Proc. SPIE- Optical Tomography and Spectroscopy of Tissue V, 4955: 416-423 (2003)

11. Xiaorong Xu, Wen Zhu, Vikram Padival, **Mengna Xia**, Xuefeng Cheng,, "Validation Of NIRS In measuring tissue hemoglobin concentration and oxygen saturation on ex vivo and isolated limb models", Proc. SPIE- Optical Tomography and Spectroscopy of Tissue V, 4955: 369-378 (2003)

REFERENCES

1. Vaupel, P., K. Schlenger, C. Knoop, and M. Hockel, *Oxygenation of human tumors: evaluation of tissue oxygen distribution in breast cancers by computerized O2 tension measurement.* Cancer Res, 1991. **51**: p. 3316-22.
2. Runkel, S., A. Wischnik, J. Teubner, E. Kaven, J. Gaa, and F. Melchert, *Oxygenation of mammary tumors as evaluated by ultrosound-guided computerized-pO2-histography.* Adv Exp Med Biol, 1994. **345**: p. 451-58.
3. Movsas, B., J. Chapman, and E. Horwotz, *Hypoxic regions exist in human prostate carcinoma.* Urology, 1999. **53**: p. 11-18.
4. Hockel, M., K. Schlenger, B. Aral, M. Mitze, U. Schaffer, and P. Vaupel, *Association between tumor hypoxia and malignant progression in advanced cancer of the uterine cervix.* Cancer Res, 1996. **56**: p. 4509-15.
5. Nordsmark, M., M. Overgaard, and J. Overgaard, *Pretreatment oxygenation predicts radiation response in advanced squamous cell carcinoma of the head and neck.* Radiother Oncol, 1996. **41**: p. 31-9.
6. Brizel, D., R. Dodge, R. Clough, and M. Dewhirst, *Oxygenation of head and neck cancer: changes during radiotherapy and impact on treatment outcome.* Radiother Oncol, 1999. **53**: p. 113-7.
7. Gray, L., A. Conger, M. Ebert, S. Hornsey, and O. Scott, *Concentration of oxygen dissolved in tissues at the time of irradiation as a factor in radiotherapy.* Br J Radiol, 1953. **26**: p. 638-48.
8. Durand, R., *The influence of microenvironmental factors during cancer therapy.* In Vivo, 1994. **8**: p. 691-702.
9. Baish, J., Y. Gazit, D. Berk, M. Nozue, L. Baxter, and R. Jain, *Role of tumor vascular architecture in nutrient and drug delivery: an invasion percolation-based network model.* Microvasc Res, 1996. **51**: p. 327-46.
10. Mason, R.P., S. Ran, and P.E. Thorpe, *Quantitative assessment of tumor oxygen dynamics: molecular imaging for prognostic radiology.* J. Cell Biochem., 2002. **39**: p. 45-53.
11. Zhao, D., L. Jiang, and R.P. Mason, *Measuring changes in tumor oxygenation.* Methods Enzymol., 2004. **386**: p. 378-418.
12. Mason, R.P., A. Constantinescu, S. Hunjan, D. Le, E.W. Hahn, P.P. Antich, C. Blum, and P. Peschke, *Regional tumor oxygenation and measurement of dynamic changes.* Radiat. Res., 1999. **152**(3): p. 239-49.
13. Hunjan, S., R.P. Mason, A. Constantinescu, P. Peschke, E.W. Hahn, and P.P. Antich, *Regional tumor oximetry: 19F NMR spectroscopy of hexafluorobenzene.* Int. J. Radiat. Oncol. Biol. Phys., 1998. **41**(1): p. 161-71.

14. Hunjan, S., D. Zhao, A. Constantinescu, E.W. Hahn, P.P. Antich, and R.P. Mason, *Tumor oximetry: demonstration of an enhanced dynamic mapping procedure using fluorine-19 echo planar magnetic resonance imaging in the Dunning prostate R3327-AT1 rat tumor.* Int. J. Radiat. Oncol. Biol. Phys., 2001. **49**(4): p. 1097-1108.
15. Mason, R.P., S. Hunjan, A. Constantinescu, Y. Song, D. Zhao, E.W. Hahn, P.P. Antich, and P. Peschke, *Tumor oximetry: comparison of 19F MR EPI and electrodes.* Adv. Exp. Med. Biol., 2003. **530**: p. 19-27.
16. Liu, H., Y. Song, K.L. Worden, X. Jiang, A. Constantinescu, and R.P. Mason, *Noninvasive Investigation of Blood Oxygenation Dynamics of Tumors by Near-Infrared Spectroscopy. Appl. Opt.*, 2000. **39**(28): p. 5231-5243.
17. Steinberg, F., H.J. Rohrborn, T. Otto, K.M. Scheufler, and C. Streffer, *NIR reflection measurements of hemoglobin and cytochrome aa3 in healthy tissue and tumors. Correlations to oxygen consumption: preclinical and clinical data.* Adv. Exp. Med. Biol., 1997. **428**: p. 69-77.
18. Cope, M., *the application of near infrared spectroscopy to non invasive monitoring of cerebral oxygenation in the newborn infant*. 1991, Ph.D dissertation in University of London.
19. Mueller-Klieser, W., P. Vaupel, and R. Manz, *Tumor oxygenation under normobaric and hyperbaric conditions.* Br J Radiol, 1983. **56**: p. 559-64.
20. Petre, P., F. Baciewicz, S. Figan, and J. Spear, *Hyperbaric oxygen as a chemotherapy adjuvant in the treatment of metastatic lung tumors in a rat model.* J Thorac Cardiovasc Surg, 2003. **125**: p. 85-95.
21. Kalns, J., L. Krock, and E. Piepmeier, *The effect of hyperbaric oxygen on growth and chemosensitivity of metastatic prostate cancer.* Anticancer Res, 1998. **18**.
22. Takiguchi, N., N. Saito, M. Nunomura, K. Kouda, K. Oda, N. Furuyama, and N. Nakajima, *Use of 5-FU plus hyperbaric oxygen for treating malignant tumors:evaluation of antitumor effect and measurement of 5-FU in individual organs.* Cancer Chemother Pharmacol, 2001. **47**: p. 11-14.
23. Peterson, J., V. Fitzgerald, and D. Buckhold, *Fiber-optic probe for in vivo measurement of oxygen partial pressure.* Anal. Chem., 1984. **56**: p. 62-67.
24. Gu, Y., V.A. Bourke, J.G. Kim, A. Constantinescu, R.P. Mason, and H. Liu, *Dynamic response of breast tumor oxygenation to hyperoxic respiratory challenge monitored with three oxygen-sensitive parameters.* Appl. Opt., 2003. **42**(16): p. 2960-2967.
25. Hall, E.J., *The oxygen effect and reoxygenation*, in *Radiobiology for the Radiologist*, E.J. Hall, Editor. 1994, J. B. Lippincott: Philadelphia. p. 133-152.
26. Chapman, J.D., C.C. Stobbe, M.R. Arnfield, R. Santus, J. Lee, and M.S. McPhee, *Oxygen dependency of tumor cell killing in vitro by light-activated Photofrin II.* Radiat. Res., 1991. **126**(1): p. 73-79.
27. Brown, J.M., *The hypoxic cell: a target for selective cancer therapy--eighteenth Bruce F. Cain Memorial Award lecture.* Cancer Res., 1999. **59**(23): p. 5863-5870.

28. Fyles, A.W., M. Milosevic, R. Wong, M.C. Kavanagh, M. Pintilie, A. Sun, W. Chapman, W. Levin, L. Manchul, T.J. Keane, and R.P. Hill, *Oxygenation predicts radiation response and survival in patients with cervix cancer.* Radiother. Oncol., 1998. **48**(2): p. 149-156.
29. Welch, M.J., H. Halpern, and K.A. Kurdziel, *Example of imaging solutions to multi-disease biological challenge--imaging of hypoxia.* Acad. Radiol., 2003. **10**: p. 887-890.
30. Hockel, M., K. Schlenger, B. Aral, M. Mitze, U. Schaffer, and P. Vaupel, *Association between tumor hypoxia and malignant progression in advanced cancer of the uterine cervix.* Cancer Res., 1996. **56**(19): p. 4509-4515.
31. Overgaard, J. and M.R. Horsman, *Modification of hypoxia-induced radioresistance in tumors by the use of oxygen and sensitizers.* Semin. Radiat. Oncol., 1996. **6**: p. 10-21.
32. Sevick, E.M., B. Chance, J. Leigh, S. Nioka, and M. Maris, *Quantitation of time- and frequency-resolved optical spectra for the determination of tissue oxygenation.* Anal. Biochem., 1991. **195**(2): p. 330-351.
33. Delpy, D.T. and M. Cope, *Quantification in tissue near-infrared spectroscopy.* Phil. Trans. R. Soc. Lond. B., 1997. **352**: p. 649-659.
34. Yodh, A.G. and D.A. Boas, *Functional imaging with diffusing light*, in *Biomedical photonics handbook*, V. Tuan, Editor. 2003, CRC: Florida.
35. Homma, S., T. Fukunaga, and A. Kagaya, *Influence of adipose tissue thickness on near-infrared spectroscopic signals in the measurement of human muscles.* J. Biomed. Opt., 1996. **1**: p. 418-424.
36. Hull, E.L., D.L. Conover, and T.H. Foster, *Carbogen-induced changes in rat mammary tumour oxygenation reported by near infrared spectroscopy.* Br. J. Cancer, 1999. **79**(11-12): p. 1709-1716.
37. Pogue, B., H. Zhu, C. Nwaigwe, T. McBride, U. Osterberg, K. Paulsen, and J. Dunn, *Hemoglobin imaging with hybrid magnetic resonance and near-infrared diffuse tomography.* Adv Exp Med Biol, 2003. **530**: p. 215-24.
38. Chance, B., *Near infrared images using continuous, phase modulated and pulsed light with quantitation of blood and oxygenation.* Ann. New Acad. Sci., 1997. **838**: p. 29-45.
39. Shah, N., A.E. Cerussi, D. Jakubowski, D. Hsiang, J. Butler, and B.J. Tromberg, *Spatial variations in optical and physiological properties of healthy breast tissue.* J. Biomed. Opt., 2004. **9**(3): p. 534-40.
40. Dehghani, H., M.M. Doyley, B.W. Pogue, S. Jiang, J. Geng, and K.D. Paulsen, *Breast deformation modeling for image reconstruction in near infrared optical tomography.* Phys. Med. Biol., 2004. **49**(7): p. 1131-45.
41. Conover, D.L., B.M. Fenton, T.H. Foster, and E.L. Hull, *An evaluation of near infrared spectroscopy and cryospectrophotometry estimates of haemoglobin oxygen saturation in a rodent mammary tumour model.* Phys. Med. Biol., 2000. **45**: p. 2685-2700.
42. Kim, J.G., D. Zhao, Y. Song, A. Constantinescu, R.P. Mason, and H. Liu, *Interplay of tumor vascular oxygenation and tumor pO2 observed using near-*

infrared spectroscopy, an oxygen needle electrode, and 19F MR pO2 mapping. J. Biomed. Opt., 2003b. **8**(1): p. 53-62.
43. Hahn, E.W., P. Peschke, R.P. Mason, E.E. Babcock, and P.P. Antich, *Isolated tumor growth in a surgically formed skin pedicle in the rat: a new tumor model for NMR studies.* Magn. Reson. Imaging, 1993. **11**(7): p. 1007-1017.
44. Yang, Y., H. Liu, X. Li, and B. Chance, *Low-cost frequency-domain photon migration instrument for tissue spectroscopy, oximetry, and imaging.* Opt. Eng., 1997. **36**: p. 1562-1569.
45. Kety, S.S., *The theory and applications of the exchange of inert gas at the lungs and tissues.* Pharmacol. Rev., 1951. **3**(1): p. 1-41.
46. Song, Y., A. Contantinescu, and R.P. Mason, *Dynamic breast tumor oximetry: the development of prognostic radiology.* Technol. in Cancer Res. & Treatm., 2002. **1**(6): p. 471-478.
47. Mazurchuk, R., R. Zhou, R.M. Straubinger, R.I. Chau, and Z. Grossman, *Functional magnetic resonance (fMRI) imaging of a rat brain tumor model: implications for evaluation of tumor microvasculature and therapeutic response.* Magn Reson Imaging, 1999. **17**: p. 537-548.
48. Kim, J.G. and H. Liu, *Investigation of bi-phasic tumor oxygen dynamics induced by hyperoxic gas intervention: a numerical study.* Opt. Express, 2005. **13**: p. 4465-75.
49. Kim, J.G. and H. Liu. *Investigation of breast tumor hemodynamics using tumor vascular phantoms and FEM simulations*. in *Biomedical Optics Topical Meetings on CD-ROM*. 2004. Washington DC: the Optical Society of America.
50. Toronov, V., A. Webb, J.H. Choi, M. Wolf, A. Michalos, E. Gratton, and D. Hueber, *Investigation of human brain hemodynamics by simultaneous near-infrared spectroscopy and functional magnetic resonance imaging.* Med. Phys., 2001. **28**: p. 521-7.
51. Chen, Y., D.R. Tailor, Intes X, and B. Chance, *Correlation between near-infrared spectroscopy and magnetic resonance imaging of rat brain oxygenation modulation.* Phys. Med. Biol., 2003. **48**(4): p. 417-427.
52. Ntziachristos, V., A.G. Yodh, M. Schnall, and B. Chance, *Concurrent MRI and diffuse optical tomography of breast after indocyanine green enhancement.* Proc. Natl. Acad. Sci. USA, 2000. **97**: p. 2767-2772.
53. Ntziachristos, V., A.G. Yodh, M. Schnall, and B. Chance, *MRI-guided diffuse optical spectroscopy of malignant and benign breast lesions.* Neoplasia, 2002. **4**: p. 347-354.
54. Gulsen, G., H. Yu, J. Wang, O. Nalcioglu, S. Merritt, F. Bevilacqua, A.J. Durkin, D.J. Cuccia, R. Lanning, and B.J. Tromberg, *Congruent MRI and near-infrared spectroscopy for functional and structural imaging of tumors.* Technol. Cancer Res. Treat., 2002. **1**: p. 497-505.
55. Gu, Y., V. Kodibagkar, M. Xia, A. Constantinescu, R. Mason, and H. Liu. *Correlation of NIR spectroscopy with BOLD MR imaging of assessing breast tumor vascular oxygen status*. in *OSA Biomedical Optics Topical Meetings*. 2004. Miami, FL: The Optical Society of America.

56. Arridge, S.R. and M. Schweiger, *Photon measurement density functions: II. Finite element method calculations.* Appl. Opt., 1995. **34**: p. 8026-8037.
57. Arridge, S.R., *Photon measurement density functions: I. Analytical forms.* Appl. Opt., 1995. **34**: p. 7395-7409.
58. Gu, Y., R.P. Mason, and H. Liu, *Estimated fraction of tumor vascular blood contents sampled by near infrared spectroscopy and 19F magnetic resonance spectroscopy.* Opt. Express, 2004b. **13**: p. 1724 - 1733.
59. Zhao, D., A. Constantinescu, E.W. Hahn, and R.P. Mason, *Tumor oxygen dynamics with respect to growth and respiratory challenge: investigation of the Dunning prostate R3327-HI tumor.* Radiat. Res., 2001. **156**(5 Pt 1): p. 510-20.
60. Zhao, D., A. Constantinescu, E.W. Hahn, and R.P. Mason, *Differential oxygen dynamics in two diverse dunning prostate R3327 rat tumor sublines (MAT-Lu and HI) with respect to growth and respiratory challenge.* Int. J. Radiat. Oncol. Biol. Phys., 2002. **53**(3): p. 744-756.
61. Vaupel, P., D.K. Kelleher, and T. Engel, *Do changes in tumor blood flow necessarily lead to changes in tissue oxygenation and in bioenergetic status?* Adv. Exp. Med. Biol., 1994. **361**: p. 607-11.
62. Braun, R.D., J.L. Lanzen, and M.W. Dewhirst, *Fourier analysis of fluctuations of oxygen tension and blood flow in R3230Ac tumors and muscle in rats.* Am. J. Physiol., 1999. **277**(2 Pt 2): p. H551-68.
63. Kimura, H., R.D. Braun, E.T. Ong, R. Hsu, T.W. Secomb, D. Papahadjopoulos, K. Hong, and M.W. Dewhirst, *Fluctuations in red cell flux in tumor microvessels can lead to transient hypoxia and reoxygenation in tumor parenchyma.* Cancer Res., 1996. **56**(23): p. 5522-8.
64. Baudelet, C. and B. Gallez, *How does blood oxygen level-dependent (BOLD) contrast correlate with oxygen partial pressure (pO2) inside tumors?* Magn Reson Med., 2002. **48**: p. 980-6.
65. Kim, J.G., Y. Gu, A. Constantinescu, R.P. Mason, and H. Liu. *Non-uniform tumor vascular oxygen dynamics monitored by three-channel near-infrared spectroscopy*. in *Proc. SPIE-Int. Soc. Opt. Eng.* 2003a. Bellingham: SPIE.
66. Brooksby, B.A., H. Dehghani, B.W. Pogue, and K.D. Paulsen, *Near infrared (NIR) tomography breast image reconstruction with a priori structural information from MRI: algorithm development for reconstructing heterogeneities.* IEEE J. Select Topics Quantum Electron., 2003. **9**: p. 199-209.
67. Thomlinson, R., *An experimental method for comparing treatments of intact malignant tumours in animals and its application to the use of oxygen in radiotherapy.* Br J Cancer, 1960. **14**: p. 555-576.
68. Kinoshita, Y., K. Kohshi, N. Kunugita, T. Yosaki, and A. Yokota, *Preservation of tumour oxygen after hyperbaric oxygenation monitored by magnetic resonance imaging.* Br J Cancer, 2000. **82**: p. 88-92.
69. Brizel, D., W. Hage, R. Dodge, M. Munley, C. Piantadosi, and M. Dewhirst, *Hyperbaric oxygen improves tumor radiation response significantly more than carbogen/Nicotinamide.* Radiat Res, 1997. **147**: p. 715-720.

70. Powell, M., D. Collingridge, M. Saunders, P. Hoskin, S. Hill, and D. Chaplin, *Improvement in human tumour oxygenation with carbogen of varying CO2 concentrations.* Radiother Oncol, 1999. **50**: p. 167-171.
71. Grau, C., M. Horsman, and J. Overgaard, *Improving the radiation response in a C3H mouse mammary carcinoma by normobaric oxygen or carbogen breathing.* Int J Radiat Oncol Biol Phys, 1992. **22**: p. 415-419.
72. Olive, P. and W. Inch, *Effect of inhaling oxygen/carbon dioxide mixtures on oxygenation and cure by X-rays of the C3HBA mouse mammary carcinoma.* Radiology, 1973. **106**: p. 673-678.
73. Zhao, D., L. Jiang, and R. Mason, *Measuring changes in tumor oxygenation.* Methods Enzymol, 2004. **386**: p. 378-418.
74. Shtern, F. and D. Windfield, *Report of the joint working group on quantitative in vivo functional imaging in oncology.* Acad Radiol, 1999. **6**: p. S259-300.
75. Stone, H.B., J.M. Brown, T.L. Phillips, and R.M. Sutherland, *Oxygen in human tumors: correlations between methods of measurement and response to therapy. Summary of a workshop held November 19-20, 1992, at the National Cancer Institute, Bethesda, Maryland.* Radiat Res, 1993. **136**(3): p. 422-34.
76. Liu, H., Y. Gu, J.G. Kim, and R. Mason, *Near-infrared Spectroscopy and Imaging of Tumor Vasculature Oxygenation.* Methods Enzymol, 2004. **386**: p. 349-378.
77. Hull, E.L., D.L. Conover, and T.H. Foster, *Carbogen-induced changes in rat mammary tumour oxygenation reported by near infrared spectroscopy.* Br J Cancer, 1999. **79**(11-12): p. 1709-16.
78. Wang, H., M. Putt, M. Emanuele, D. Shin, E. Glatstein, and A.G. Yodh, *Treatment-induced changes in tumor oxygenation predict photodynamic therapy outcome.* Cancer Res, 2004. **64**: p. 7553-7561.
79. Song, C., J. Rhee, and D. Haumschild, *Continuous and non-invasive quantification of heat-induced changes in blood flow in the skin and RIF-1 tumor of mice by laser Doppler flowmetry.* Int J Hyperthermia, 1987. **3**: p. 71-7.
80. Lanzen, J.L., R.D. Braun, A.L. Ong, and M.W. Dewhirst, *Variability in blood flow and pO2 in tumors in response to carbogen breathing.* Int.J Radiat Oncol Biol Phys., 1998. **42**(4): p. 855-859.
81. Powell, M.E.B., S.A. Hill, M.I. Saunders, P.J. Hoskin, and D.J. Chaplin, *Effect of carbogen breathing on tumour microregional blood flow in humans.* Radiother and Oncol, 1996. **41**(3): p. 225-231.
82. Pigott, K.H., S.A. Hill, D.J. Chaplin, and M.I. Saunders, *Microregional fluctuations in perfusion within human tumours detected using laser Doppler flowmetry.* Radiother and Oncol, 1996. **40**(1): p. 45-50.
83. Stevens, H., H.M.L. Jansen, J. De Reuck, M. Lemmerling, K. Strijckmans, P. Goethals, I. Lemahieu, B.M. de Jong, A.T.M. Willemsen, and J. Korf, *55Cobalt (Co) as a PET-tracer in stroke, compared with blood flow, oxygen metabolism, blood volume and gadolinium-MRI.* J Neurol Sci, 1999. **171**(1): p. 11-18.

84. Mineura, K., T. Sasajima, M. Kowada, T. Ogawa, J. Hatazawa, and K. Uemura, *Long-term positron emission tomography evaluation of slowly progressive gliomas.* Eur J Cancer, 1996. **32**(7): p. 1257-1260.
85. Boas, D., G. Strangman, J. Culver, R. Hoge, G. Jasdzewski, R. Poldrack, B. Rosen, and J. Mandeville, *Can the cerebral metabolic rate of oxygen be estimated with near-infrared spectroscopy?* Phys Med Biol, 2003. **48**: p. 2405-2418.
86. Hahn, E.W., P. Peschke, R.P. Mason, E.E. Babcock, and P.P. Antich, *Isolated tumor growth in a surgically formed skin pedicle in the rat: a new tumor model for NMR studies.* Magn Reson Imaging, 1993. **11**(7): p. 1007-17.
87. Cope, M., *the application of near infrared spectroscopy to non invasive monitoring of cerebral oxygenation in the newborn infant*. 1991, the university of London.
88. Jones, M., J. Berwick, D. Johnston, and J. Mayhew, *Concurrent Optical Imaging Spectroscopy and Laser-Doppler Flowmetry: The Relationship between Blood Flow, Oxygenation, and Volume in Rodent Barrel Cortex.* NeuroImage, 2001. **13**(6): p. 1002-1015.
89. Mandeville, J., J. Marota, C. Ayata, G. Zaharchuk, M. Moskowitz, B. Rosen, and R. Weisskoff, *Evidence of a cerebrovascular postarteriole windkessel with delayed compliance.* J Cereb Blood Flow Metab, 1999. **19**: p. 679-689.
90. Song, Y., J. Kim, R. Mason, and H. Liu, *Investigation of rat breast tumour oxygen consumption by near-infrared spectroscopy.* J. Phys. D: Appl. Phys., 2005. **38**: p. 2682–2690.
91. Honess, D. and N. Bleehen, *Perfusion changes in the RIF-1 tumor and normal tissues after carbogen and nicotinamide, individually and combined.* Br J Cancer, 1995. **71**: p. 1175-1180.
92. Robinson, S., F. Howe, and J. Griffiths, *Non-invasive monitoring of carbogen-induced changes in tumor blood flow and oxygenation by functional magnetic resonance imaging.* Int J Radiat Oncol Biol Phys, 1995. **33**: p. 855-859.
93. Hill, S., D. Collingridge, B. Vojnovic, and D. Chaplin, *Tumor radiosensitization by high oxygen content gases: influence of the carbon dioxide content of the inspired gas on pO2,microcirculatory function and radiosensitivity.* Int J Radiat Oncol Biol Phys, 1998. **40**: p. 943-959.
94. Dunn, T., R. Braun, W. Rhenus, G. Rosner, T. Secomb, G. Tozer, D. Chaplin, and M. Dewhirst, *The effects of hyperoxic and hypercarbic gases on tumor blood flow.* Br J Cancer, 1999. **80**: p. 117-126.
95. Zhao, D., A. Constantinescu, C. Chang, E.W. Hahn, and R.P. Mason, *Correlation of tumor oxygen dynamics with radiation response of the Dunning Prostate R3327-HI tumor.* Radiat Res, 2003. **159**(5): p. 621-31.
96. Brady, L., H. Plenk, J. Hanley, J. Glassburn, S. Kramer, and R. Parker, *Hyperbaric oxygen therapy for carcinoma of the cervix stages IIB, IIIB, and IVA: results of a randomized study by the radiation therapy oncology group.* Int J Radiat Onclo Biol Phys, 1981. **7**: p. 991-8.

97. Berry, G., B. Dixon, and A. Ward, *The leeds results for radiotherapy in HBO for carcinoma of the head and neck.* Clin Radiol, 1979. **30**: p. 591-2.
98. Hunugita, N., K. Kkihshi, Y. Kinoshita, T. Katoh, H. Abe, T. Tosaki, T. Kawamoto, and T. Norimura, *Radiotherapy after hyperbaric oxygenation improves radioresponse in experimental tumor models.* Cancer Letter, 2001. **164**: p. 149-54.
99. Becker, A., T. Kuhnt, H. Liedtke, A. Krivokuca, M. Bloching, and J. Dunst, *Oxygenation measurements in head and neck cancer during hyperbaric oxygenation.* Strahlenther Onkol, 2002. **2**: p. 105-8.
100. Kinoshita, Y., K. Kohshi, N. Kunugita, T. Tosaki, and A. Yokota, *Preservation of tumour oxygen after hyperbaric oxygenation monitored by magnetic resonance imaging.* British J of cancer, 2000. **82**: p. 88-92.
101. Bate, T., *The treatment of stage 3 carcinoma of the cervix by external radiotherapy and high-pressure oxygen.* Br J Radiol, 1969. **42**: p. 266-9.
102. Kienle, A. and M. Patterson, *Improved solutions of the steady-state and the time-resolved diffusion equations for reflectance from a semi-infinite turbid medium.* J Opt Soc Am A, 1997. **14**: p. 246-54.
103. Farrell, T., M. Patterson, and B. Wilson, *A diffusion theory model of spatially resolved, steady-state diffuse reflectance for the noninvasive determination of tissue optical properties in vivo.* Med Phys, 1992. **19**: p. 879-88.
104. Nichols, M., E. Hull, and T. Foster, *Design and testing of a white-light, steady-state diffuse reflectance spectrometer for determination of optical properties of highly scattering systems.* Appl Opt, 1997. **36**: p. 93-104.
105. Hull, E., M. Nichols, and T. Foster, *Quantitative broadband near-infared spectroscopy of tissue-simulating phantoms containing erythrocytes.* Phys Med Biol, 1998. **43**: p. 3381-3404.
106. Doornbos, R., R. Lang, M. Aalders, F. Cross, and H. Sterenborg, *The determination of in vivo human tissue optical properties and absolute chromophore concentrations using spatially resolved steady-state diffuse spectrosocpy.* Phys Med Biol, 1999. **44**: p. 967-81.
107. Höckel, M., K. Schlenger, C. Knoop, and P. Vaupel, *Oxygenation of carcinomas of the uterine cervix: evaluation by computerized O2 tension measurements.* Cancer Res, 1991. **51**: p. 6098-6102.
108. Griffiths, J., *The OxyLite: a fibre-optic oxygen sensor.* Br J Radiol, 1999. **72**: p. 627-30.
109. Bussink, J., J. Kaanders, A. Strik, B. Vojnovic, and A.v.d. Kogel, *Optical sensor-based oxygen tension measurements correspond with hypoxia marker binding in three human tumor xenograft lines.* Radiat Res, 2000. **154**: p. 547-55.
110. Bourke, V.A., *Dynamic interrogation of the tumor microenviorenvironment in response to radiation therapy, respiratory challenge, and pharmocologic intervention*, in *Department of Radiology*. 2005, Ph.D Dissertation in Univ of Texas Southwestern Medical Center: Dallas, TX.

111. Xia, M., V. Kodibagkar, H. Liu, and R.P. Mason, *Tumour oxygen dynamics measured simultaneously by near-infrared spectroscopy and ^{19}F magnetic resonance imaging in rats.* Phys. Med. Biol., 2006. **51**: p. 45-60.
112. Brizel, D., S. Lin, J. Johnson, J. Brooks, M. Dewhirst, and C. Piantadosi, *The mechanisms by which hyperbaric oxygen and carbogen improve tumour oxygenation.* British J of cancer, 1995. **72**: p. 1120-1124.
113. Becher, A., T. Kuhnt, H. Liedtke, A. Krivokuca, M. Bloching, and J. Dunst, *Oxygenation measurements in head and neck cancers during hyperbaric oxygenation.* Strahlenther Onkol, 2001. **178**: p. 105-8.
114. Weiss, R., G. Sarosy, K. Clagett-carr, M. Russo, and B. Leyland-jones, *Anthracyline analogs: the past, present, and future.* Cancer Chemother Pharmacol, 1986. **18**: p. 185-97.
115. Hall, E., *Radiobiology for the Radiologist*. 4th ed. 1994, Philadelphia, PA: Lippincott.
116. Thews, O., D. Kelleher, and P. Vaupel, *Erythropoietin restores the anemia-induced reduction in cyclophosphamide cytotoxicity in rat tumors.* Cancer Res, 2001. **61**: p. 1358-61.
117. Bush, R., R. Jenkin, W. Allt, F. Beale, A. Dembo, and J. Pringle, *Definitive evidence for hypoxic cells influencing cure in cancer therapy.* Br J Cancer, 1978. **37**: p. 302-06.
118. Brizel, D., W. Hage, R. Dodge, M. Munley, C. Piantadosi, and M. Dewhirst, *Hyperbaric Oxygen Improves Tumor Radiation Response Significantly More Than carbogen/Nicotinarnid.* Radiation Res., 1997. **147**: p. 715-20.
119. Rockwell, S., M. Kelley, C. Irvin, C. Hughcs, E. Porter, H. Yabuki, and J. Fischer, *Modulation of tunlor oxygenation and radiosensitivity by a perfluorooctylbromide emulsion.* Radiother Oncol, 1991. **22**: p. 92-8.
120. Lustig, R., N. Lowe, C. Rose, J. Haas, S. Krasnow, M. Spaulding, and I. Prosnitz, *Phase 1/11 study kluosol and 100% oxygen as an adjuvant to radiation i11 the treatment of locally advanced non-small cell carcinoma of the head and neck.* Int. .I. Radiat. Oncal. Biol. Phys., 1989. **16**: p. 1587-93.
121. Xia, M., V. Kodibagkar, R. Mason, B. Levine, and H. Liu. *Tumor vascular and tissue oxygenation dynamics under normobaric and hyperbaric oxygen interventions*. in *fourth Era of Hope meeting for the Department of Defense (DOD) Breast Cancer Research Program (BCRP)*. 2005. Philadelphia, PA.
122. Stuhr, L., *Hyperbaric oxygen alone or combined with 5-FU attenuates growth of DMBA-induced rat mammary tumors.* Cancer Lett, 2004. **210**: p. 35-40.
123. Jobsis, F., *Noninvasive, infrared monitoring of cerebral and myocardial oxygen sufficiency and circulatory parameters.* Science, 1977. **198**: p. 1264-7.
124. Xia, M., V. Kodibagkar, H. Liu, and R.P. Mason, *Tumour oxygen dynamics measured simultaneously by near-infrared spectroscopy and 19F magnetic resonance imaging in rats.* Physics in medicine and biology, 2006. **51**: p. 45-60.
125. Kim, J., D. Zhao, R. Mason, and H. Liu. *Acute effects of combreatastatin A4 phosphate on breast tumor hemodynamics monitored by Near Infrared*

Spectroscopy. in *in Biomedical Optics 2006 Technical Digest (Optical Society of America, Washington, DC, 2006)*. 2006.
126. Kim, J., D.J. Cuccia, J. Lee, A.E. Cerussi, A.J. Durkin, and B.J. Tromberg. *Monitoring of chemotherapy effects on rat breast tumors: a correlation between optical signals and histology*. in *SPIE*. 2007. San Jose, CA.
127. Cohen, M., A. Johnston-Early, M. Hood, M. McKenzie, M. Citron, N. Jaffe, and S. Krasnow, *Drug precipitation within i.v. tubing: a potential hazard of chemotherapy administration.* Cancer Treat Rep. 1985 Nov;69(11):1325-6, 1985. **69**: p. 1325-6.
128. Esenaliev, R., Y. Petrov, O. Hartrumpf, D. Deyo, and D. Prough, *Continuous, noninvasive monitoring of total hemoglobin concentration using an optoacoustic technique.* Appl Opt, 2004. **43**: p. 3401-07.
129. Alagoz, T., R. Buller, B. Anderson, K. Terrell, R. Squatrito, T. Niemann, D. Tatman, and P. Jebson, *Evaluation of hyperbaric oxygen as a chemosensitizer in the treatment of epithelial ovarian cancer in xenografts in mice.* Cancer, 1995. **75**: p. 2313-22.
130. Kong, Q., J. Beel, and K. Lillehei, *A threshold concept for cancer therapy.* Med Hpyotheses, 2000. **55**: p. 29-35.
131. Harrisona, L., M. Chadhaa, R. Hillb, K. Hua, and D. Shashaa, *Impact of tumor hypoxia and anemia on radiation therapy outcomes.* Oncologist, 2002. **7**: p. 492-508.
132. Laurent, A., C. Nicco, C. Chéreau, C. Goulvestre, J. Alexandre, A. Alves, E. Lévy, Goldwasser, F. Panis, O. Soubrane, B. Weill, and F. Batteux, *Controlling tumor growth by modulation endogenous production of reactive oxygen species.* Cancer Res, 2005. **65**: p. 948-56.
133. Kizaka-Kondoh, S., M. Inoue, H. Harada, and M. Hiraoka, *Tumor hypoxia: a target for selective cancer therapy.* Cancer Sci, 2003. **94**: p. 1021-28.
134. McMillan, T., K. Calhoun, J. Mader, C. Stiernberg, and S. Rajaraman, *The effect of hyperbaric oxygen on oral mucosal carcinoma.* Laryngoscope, 1989. **99**: p. 241-44.
135. Kalns, J. and E. Piepmeier, *Exposure to hyperbaric oxygen induces cell cycle perturbation in prostate cancer cells.* In Vitro Cell Dev Biol Anim, 1999. **35**: p. 98-101.
136. Murata, T., H. Yamawaki, M. Hori, K. Sato, H. Ozaki, and H. Karaki, *Chronic vascular toxicity of doxorubicin in an organ-cultured artery.* British J of Pharm, 2001. **132**: p. 1365-73.
137. Kanmura, Y., L. Raeymaekers, and R. Casteels, *Effects of doxorubicin and ruthenium red on intracellular Ca^{2+} stores in skiined rabbit mesenteric smooth-muscle fibres.* Cell Calcium, 1989. **10**: p. 433-39.
138. Ferrans, V., J. Clark, J. Zhang, Z. Yu, and E. Herman, *Pathogenesis and prevention of doxorubicin cardiomyopathy.* Tsitologiia, 1997. **39**: p. 928-37.
139. Barnett, H.J., *Stroke in women.* Can Cardiol, 1990. **6**: p. 11B-17B.
140. Derdeyn, C.P., T.O. Videen, K.D. Yundt, S.M. Fritsch, D.A. Carpenter, R.L. Grubb, and W.J. Powers, *Variability of cerebral blood volume and oxygen*

extraction: stages of cerebral haemodynamic impairment revisited. Brain, 2002. **125**: p. 597-607.
141. Sette, G., J.C. Baron, B. Mazoyer, M. Levasseur, S. Pappata, and C. Crouzel, *Local brain haemodynamics and oxygen metabolism in cerebrovascular disease: Positron emission tomography.* Brain, 1989. **112**: p. 931-51.
142. Dorsch, N., *Therapeutic approaches to vasospasm in subarachnoid hemorrhage.* Curr Opin Crit Care, 2002. **8**: p. 128-133.
143. Ohtake, M., S. Morino, T. Kaidoh, and T. Inoue, *Three-dimensional structural changes in cerebral microvessels after transient focal cerebral ischemia in rats: scanning electron microscopic study of corrosion casts.* Neurophthology, 2004. **24**: p. 219-227.
144. Schuknecht, B., J. Fandino, C. Yuksel, Y. Yonekawa, and A. Valavanis, *Endovascular treatment of cerebral vasospasm: assessment of treatment effect by cerebral angiography and transcranial colour doppler sonography.* Neuroradiology, 1999. **41**: p. 453-62.
145. Firlik, K., A. Firlik, and H. Yonas, *Xenon-enhanced computed tomography in the management of cerebral vasospasm following aneurysmal subarachnoid hemorrhage.* Keio J Med, 2000. **49**: p. A148-50.
146. Shigeki, O., D. Isao, N. Masaaki, O. Keisuke, O. Kotaro, S. Tomomi, A. Shoji, N. Yoshifumi, Y. Nobuyoshi, and O. Takashi, *Three-Dimensional Analysis of Vasospastic Major Cerebral Arteries in Rats With the Corrosion Cast Technique.* stroke, 1997. **28**: p. 1631-1638.
147. Grosset, D., J. Straiton, I. McDonald, and R. Bullock, *Angiographic and Doppler diagnosis of cerebral artery vasospasm following subarachnoid haemorrhage.* Br J Neurosurg, 1993. **7**: p. 291-8.
148. Lagalla, G., M. Ceravolo, L. Provinciali, M. Recchioni, A. Ducati, U. Pasquini, C. Piana, and U. Salvolini, *Transcranial Doppler sonographic monitoring during cerebral aneurysm embolization: a preliminary report.* Am J Neuroradiol. Sep;19(8):1549-53, 1998. **19**: p. 1549-53.
149. Wyatt, J., M. Cope, and D. Delpy, *Quantification of cerebral oxygenation and hemodynamics in sick new-born infants by near infrared spectrophotometry.* Lancet, 1986. **2**: p. 1063-1066.
150. Hazeki, O. and M. Tamura, *Quantitative analysis of hemoglobin oxygenation state of rat brain in situ by near-infrared spectrophotometry.* J Appl Physiol, 1988. **64**: p. 796-802.
151. Delpy, D., M. Cope, and E. Cady, *Cerebral monitoring in newborn infants by magnetic resonance and near infrared spectroscopy.* Scand J Clin Lab Invest, 1987. **47**: p. 9-17.
152. Brazy, J., *Cerebral oxygen monitoring with near infrared spectroscopy: clinical application to neonates.* J Clin Monit, 1991. **7**: p. 325-334.
153. Nelson, L.A., J.C. McCann, A.W. Loepke, J. Wu, B.B. Dor, and C.D. Kurth, *Development and validation of a multiwavelength spatial domain near-infrared oximeter to detect cerebral hypoxia-ischemia.* J Biomed Opt., 2006. **11**.

154. Kaul, S. and H. Ito, *Microvasculature in acute myocardial ischemia: part II: evolving concepts in pathophysiology, diagnosis and treatment.* Circulation, 2004. **109**: p. 310-315.
155. Dubal, D., M. Kashon, L. Pettigrew, and J. Ren, *Estradiol protects against ischemic injury.* J Cereb Blood Flow Metab, 1998. **18**: p. 1253-1258.
156. MacCullough, L. and P. Hurn, *Estrogen and ischemic neuroprotection: an integrated view.* Trends Endocrinol Metab, 2003. **14**: p. 228-235.
157. Hurn, P. and I. Macrae, *Estrogen as a neuroprotectant in stroke.* J Cereb Blood Flow Metab, 2000. **20**: p. 631-652.
158. Green, P., S. Yang, K. Nilsson, A. Kumar, D. Covery, and J. Simpkins, *The nonfeminizing enantiomer of 17beta-estradiol exerts protective effects in neuronal cultures and a rat model of cerebral ischemia.* Endocrinology, 2001. **142**: p. 400-406.
159. Zee, v.d., M. Cope, S. Arridge, M. Essenpreis, L. Potter, A. Edward, J. Wyatt, D. McCormick, S. Roth, E. Reynolds, and D.T. Delpy, *Experimentally measured optical pathlengths for the adult head, calf and forearm and the head of the newborn infant as a functional of inter optode spacing.* Adv Exp Med Biol, 1992. **316**: p. 143-153.
160. Buerk, D. and C. Riva, *Vasomotion and spontaneous low-frequency oscillations in blood flow and nitric oxide in cat optic nerve head.* Microvasc Res, 1998. **55**: p. 103-112.
161. Smielewski, P., P. Kirkpatrick, P. Minhas, J.D. Pickard, and M. Czosnyka, *Can cerebral vascular reactivity be measured with near-infared spectroscopy?* Stroke, 1995. **26**: p. 2285.
162. Kim, J.G., Y. Gu, A. Constantinescu, R.P. Mason, and H. Liu, *Non-uniform tumor vascular oxygen dynamics monitored by three-channel near-infrared spectroscopy*, in *Optical Tomography and Spectroscopy of Tissue V*. 2003a. p. 4955-57.
163. Mayhew, J.E.W., S. Askew, Y. Zheng, J. Porrill, G.W.M. Westby, P. Redgrave, D.M. Rector, and R.M. Harper, *Cerebral vasomotion: A 0.1-Hz oscillation in reflected light imaging of neural activity.* Neuroimaging, 1996. **4**: p. 183-93.
164. Morita-Tsuzuki, Y., E. Bouskela, and J.E. Hardebo, *Vasomotion in the rat cerebral microcirculation recorded by laser-doppler flowmetry.* Acta. Physiol. Scand., 1992. **146**: p. 431-9.
165. Diehl, R.R., D. Linden, D. Lucke, and P. Berlit, *Phase relationship between cerebral blood flow velocity blood pressure: a clinical test of autoregulation.* stroke, 1995. **26**: p. 1801-04.
166. Hu, H.H., T.B. Kuo, W.J. Wong, Y.O. Luk, C.M. Chern, L.C. Hsu, and W.Y. Sheng, *Transfer function analysis of cerebral hemodynamics in patients with carotid stenosis.* J. Cereb. Blood Metab., 1999. **19**: p. 460-5.
167. Kiviniemi, V., J. Jauhiainen, O. Tervonen, E. Paakko, J. Oikarinen, V. Vainionpaa, H. Rantala, and B. Biswal, *Slow vasomotor fluctuation in fMRI of anesthetized child brain.* Magn. Reson. Med., 2000. **44**: p. 373-8.

168. Dora, E. and A. Kovach, *Metabolic and vascular volume oscillations in the cat brain cortex.* Acta. Physiol. Acad. Sci. Hung., 1981. **57**: p. 261-275.
169. Edvinsson, L., E.T. Mackenzie, and J. McCulloch, *Cerebral blood flow and metabolism*. 1993, New York: Raven Press. 637–46.
170. Emese, S., V. Szabolcs, M. Tamas, B. Ferenc, S. Bela, S. Peter, and K. Katalin, *Effects of estrogen and progestin on hypothalamic blood flow autoregulation.* J. Soc. Gynecol. Investig., 2005. **12**: p. 604-9.
171. Goodrow, G.J., L. Vitullo, and M.J. Cipolla, *Effect of estrogen therapy on cerebral arteries during stroke in female rats.* Menopause, 2005. **12**: p. 99-109.
172. Liu, R., S. Yang, E. Perez, K.D. Yi, S.S. Wu, K. Eberst, L. Prokai, K. Prokai-Tatrai, Z.Y. Cai, D.F. Covey, A.L. Day, and J.W. Simpkins, *Neuroprotective Effects of a Novel Non-Receptor-Binding Estrogen Analogue in Vitro and In Vivo Analysis.* stroke, 2002. **33**: p. 2485-91.
173. Hurn, P.D., M.T. Littleton-Kearney, J.R. Kirsch, A.M. Dharmarajan, and R.J. Traystman, *Postischemic cerebral blood flow recovery in the female: effect of 17 beta-estradiol.* J cereb blood flow metab, 1995. **15**: p. 666-72.
174. Widder, K., R. Morris, G. Poore, D. Howard, and A. Senyei, *Tumor remission in Yoshida sarcoma-bearing rats by selective targeting of magnetic albumin microspheres containing doxorubicin.* Proc. Natl. Acad. Sci. USA, 1981. **78**: p. 579-81.
175. Zhou, R., R. Mazurchuk, and R.M. Straubinger, *Antivasculature effects of doxorubicin-containing liposomes in an intracrainial rat brain tumor model.* Cancer Res, 2002. **62**: p. 2561-66.

BIOGRAPHICAL INFORMATION

Mengna Xia was born in Nanchang, Jiangxi province, China. She received her BS and MS degree in Biomedical Engineering department at Huazhong University of Science and Technology, Wuhan, China, in 1996 and 1999 respectively. She received her Ph.D from Joint Graduate Program of Biomedical Engineering between University of Texas Southwestern Medical Center and University of Texas at Arlington on August 2007. Her research area was to apply optical approaches, such as near infrared spectroscopy and fluorescence oxygen sensor, and Magnetic Resonance Imaging to breast cancer research. She was awarded a three year pre-doctoral fellowship from Department of Defense Breast Cancer Research Program in March, 2004. She has been awarded Best Biomedical Engineering Student award and Hermann's Fellowship by Joint Graduate Program of Biomedical Engineering between University of Texas Southwestern Medical Center and University of Texas at Arlington. She had published more than 10 papers in peer-review journal and international conferences in her areas. She got married in 2003 and has a lovely baby now.